Self-organization, reactivity, and stability of nanostructured copper surfaces

Zuzana Budinská

THÈSE DE DOCTORAT DE
L'UNIVERSITÉ PIERRE ET MARIE CURIE

Spécialité

Chimie Physique et Chimie Analytique

Présentée par

Zuzana Budinská

Pour obtenir le grade de

DOCTEUR de L'UNIVERSITÉ PIERRE ET MARIE CURIE

Self-organization, reactivity, and stability of nanostructured copper surfaces

Auto-organisation, réactivité et stabilité de surfaces nanostructurées de cuivre

---

soutenue le 20 Novembre 2015 devant le jury composé de :

M. Vincent Fournée	Directeur de Recherche	Rapporteur
M. Vincent Repain	Professeur	Rapporteur
M. Geoff Thornton	Professeur	Examinateur
M. Jacques Jupille	Directeur de Recherche Émérite	Examinateur
M. Philippe Marcus	Directeur de Recherche	Directeur de thèse
M. Frédéric Wiame	Maître de Conférences	Encadrant
M. Vincent Maurice	Directeur de Recherche	Membre invité

Acknowledgements

The present thesis work was done in the group "Physico-Chimie des Surfaces" of Institut de Recherche de Chimie Paris with a fellowship provided by UPMC.

I would like to thank ...

...my thesis director Philippe Marcus for giving me the opportunity to do my thesis in the PCS laboratory and for his supervision and correction of my thesis manuscript.

...my thesis advisor Frédéric Wiame for his guidance throughout the past three years, for introducing me to STM, for his advice during writing of my thesis and correction of my manuscripts, as well as for always answering all of my questions.

...Vincent Maurice for help with corrections of my manuscripts.

...the rapporteurs Vincent Fournée et Vincent Repain for devoting their time to the review of my scientific work.

...the jury members Geoff Thornton and Jacques Jupille for accepting to assist in my thesis defense.

...UPMC and CNRS for financial support.

...Lorena Klein for help with polishing of my samples.

...all my fellow PhD students and post-docs, Matthieu, Blanca, Shadi, Emna, Hao, Bingbing, Clément, Toni, Jun, Slava, Oumaima, Svetlana, Rémi, Marion, Hu, Elise, Pauline, Luis and Mohamed (in order of appearance), and also all "permanents" of the lab, for creating a friendly work environment.

...my parents Ivana and Luboš for being my role models.

...JB for his love.

Table of contents

Introduction

When thinking about the progress in the field of electronics over the last decades, we could imagine that there are no limits. Computers have been shrinking in front of our eyes ever since they have been invented. This behavior is captured by the so-called "Moore's law", which says that the number of transistors in a dense integrated circuit doubles approximately every two years [1]. Today, the miniaturization of electronics has come so far that there is a need for nanoscale structural assemblies to perform the functions of a computer, data storage device, laser or satellite. We are now entering a so-called "More than Moore's" phase [2], in which it comes to not only further miniaturization, but also functional diversification. With decreasing size of devices to the nanometer scale, their properties begin to differ due to quantum size effects arising from the reduced dimensions and surface effects arising from the increased surface-to-volume ratio. The nanodevices show new electronic, optical or magnetic properties. Therefore new functionalities are incorporated into devices that do not necessarily scale according to "Moore's law", but provide additional value. The "More than Moore's" approach adds typically non-digital functionalities (e.g. radio frequency devices, power control, actuators, sensors, microelectromechanical systems (MEMS)).

To fabricate a structure in nanodimensions, two approaches can be differentiated: so-called top-down or bottom-up approach. The top-down approach means directly shaping a solid by means of e.g. lithography or etching. The bottom-up approach is when one builds up the final structures from parts, such as molecules or even atoms. Atom manipulation can be used, however it is rather slow for industrial purposes and therefore the bottom-up approach takes advantage of self-assembly and/or self-ordering processes to create the desired structure.

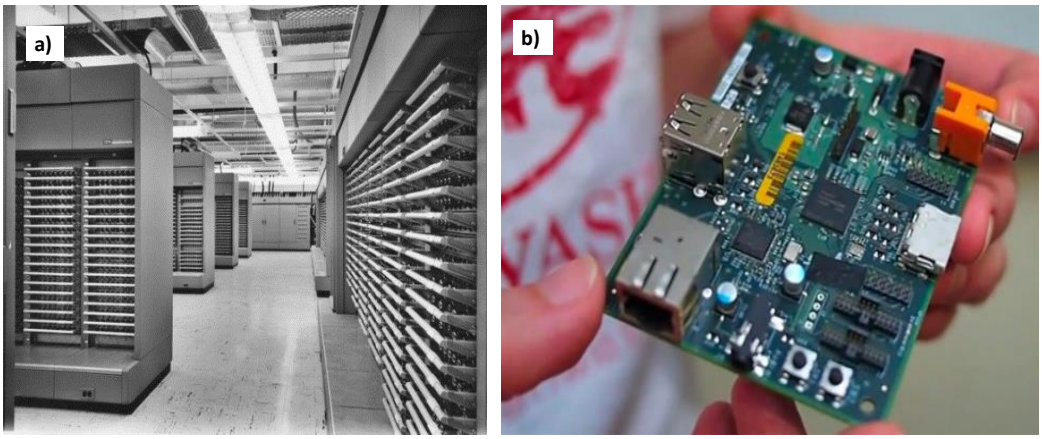

Fig. I. 1: Miniaturization of electronics: a) Computer System AN/FSQ-7 from the year 1958. [3] b) One of today's smallest computers: Raspberry Pi [4].

The top-down approach is being successfully implemented to create transistor in nanodimensions. For example the International Technology Roadmap for Semiconductors (ITRS) states that in 2014 the size of semiconductor devices has reached 14 nanometers and is expected to reach 10 nm in 2016. Multiple patterning lithography techniques have to be implemented. But physical limitations to downscaling are being reached and the progress will slow down, if new methods for nanofabrication are not implemented to reach such small dimensions. For further miniaturization of devices, the bottom-up approach has to be implemented and thus the understanding and controlling of self-organized processes becomes very important.

The civilization has gone a long way since the time first computers that filled an entire room and weighed 300 tons, were produced. In Fig. I.1a), the largest computer system ever built, from the year 1958, is shown. It took up the area of $\approx$ 2000 m^2 and performed 75 kilo instructions per second (kIPS). Nowadays, computers with the size of a credit card are being built, as for example the Raspberry Pi, shown in Fig. I .1b). This computer from the year 2012 weighs only about 45 g and performs 1.2 GIPS.

To achieve even smaller computers with higher performance, one has to be able to create transistors consisting of only a few atoms. Today, we are able to manipulate molecules and atoms to create electronics in nanodimensions or even make a movie by moving molecules, as has been done by IBM Research (shown in Fig. I.2). But as Richard P. Feynman stated in his famous talk to the American Physical Society in 1960 [5], "there is plenty of room at the bottom" and it is only up to the combined

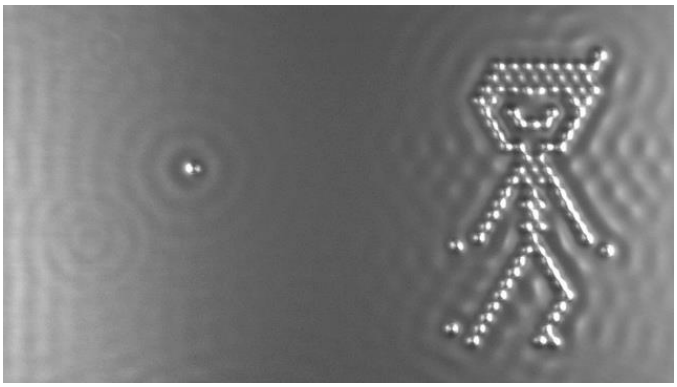

Fig. I. 2: An image from a stop-motion animated film of IBM Research, "A Boy And His Atom: The World's Smallest Movie", made by moving carbon monoxide molecules by STM [6].

effort of the world's scientific community to keep expanding the possibilities of today's technology.

In the present thesis we have tried to make a contribution to the field of nanotechnology by performing a fundamental study of the self-organized nanostructured Cu(110)-(2×1)O surface [7]. Our work has been motivated by three different aspects. Firstly, we are interested in understanding the fundamentals of the self-organization process and also in the possibility to control it. The self-organized systems have a potential application as templates for the bottom-up approach and the field of nanofabrication would greatly benefit from the possibility of tuning their morphology. We have chosen the Cu(110)-(2×1)O system for its simple preparation method and easy characterization. Additionally, this surface has already been used as a template for guided adsorption of organic molecules for application in organic electronics [8–13].

Our second objective was to use the control of the self-organization, to investigate the dependency of the morphology of a nanostructure on its reactivity. The ability to control a reaction by changing the morphology of the surface on which the reaction takes place finds application in both the field of catalysis and corrosion protection. For our study we have chosen the sulfidation of the tunable Cu(110)-(2×1)O surface. The reaction between sulfur and oxygen on metals is of industrial importance, because sulfur is a common catalyst poison. Furthermore, gases containing sulfur are corrosive and sulfur acts as a poison for corrosion protection.

Thirdly, in order to employ self-organized surfaces in nanotechnology, their stability is a crucial factor. Therefore we are also interested in studying the surface

dynamic evolution in UHV. Additionally, the dynamic behavior of islands nucleated on a surface give an insight into the kinetics of thin film growth.

Outline of the thesis

The present thesis is structured as follows:

The first chapter is dedicated to the motivation of our study and the state of the art of the work on the Cu(110)-(2×1)O nanostructure, as well as on the sulfidation of the clean and pre-oxidized Cu(110) surfaces. The objectives of the present thesis are pointed out in this chapter.

In the second chapter, we describe the experimental setup, as well as all experimental techniques used within the present thesis. We further discuss sample preparation and preparation of tips for scanning tunneling microscopy (STM). The experimental conditions of the experiments performed within this thesis are presented at the end of the chapter.

The third chapter presents results obtained from experiments aimed at tuning the Cu(110)-(2×1)O nanostructure by sulfur co-adsorption. The modified Marchenko-Vanderbilt model, describing the increase of the periodicity caused by the presence of sulfur, is presented.

The fourth chapter is dedicated to the sulfidation of the tunable Cu(110)-(2×1)O nanostructure. It includes results of a study of the reaction kinetics by Auger electron spectroscopy (AES) and the reaction mechanism by STM, in real time conditions. We present a comparison of the results for nanostructures with different widths of the oxidized stripes, but the same oxygen coverage. This way we can identify the influence of the structure on the reactivity without the influence of a changing oxygen coverage. The reaction mechanism observed for the case of wide oxidized stripes, namely the formation of sulfur islands on the oxidized stripes, is described. We present a detailed study of the island formation, as well as the study of the influence of the exposure conditions (pressure) on the mechanism.

The fifth chapter includes results of the experimental study of the stability of S-c(2×2) islands, formed by sulfidation of the Cu(110)-(2×1)O nanostructure, under UHV conditions. The surface diffusion of the islands has been followed by recording consecutive STM images, after the exposure to H_2S until all oxygen has been removed from the surface. A comparison of our data with theoretical and experimental observations on other systems is given.

The main results and conclusions of this thesis are summarized in the final part, Conclusions and perspectives. The perspectives which have been opened by the present study are also introduced.

Chapter 1

State of the art and objectives

In the beginning of the present chapter, we will discuss the self-organization in general and show different examples of this phenomenon known from the literature. We will also discuss how the self-organized nanostructures can be used as adsorption templates in the field of nanotechnology. Following is the presentation of the fundamental studies of the influence of morphology on the reactivity, which are important in the field of catalysis or corrosion protection. The rest of the chapter is dedicated to state of the art of the studies on the Cu(110)-(2×1)O nanostructure and the sulfidation of this surface. Finally, the theories and experimental observations about surface diffusion of large clusters known from the literature, are presented. The objectives of this thesis are given at the end of each section.

1.1 Self-organization

We find examples of self-organized or self-assembled systems everywhere in the nature. We can see them in patterns in cosmic arrays of galaxies, stripes on a zebra, down to atomic structures of a crystal [14–22]. Different forces are responsible for the arrangement. Gravitational forces play a role in creating galaxy arrays and crystal structures are created due to chemical bonds.

Self-ordering on crystals is the spontaneous formation of periodic domains in the 1–100 nm range under equilibrium conditions. Thanks to self-organized systems, we are able to grow nanostructures with regular size and spacing in an efficient and relatively simple way. The self-organization studied in the present thesis originates from an elastic relaxation of a strained surface. Strain can be induced by different processes, e.g. surface faceting processes, manipulating steps in a vicinal surface

or growth of a strained overlayer film. There are many examples of self-organized systems on crystal surfaces. 1D periodic patterns have been observed on Au(111) [23], Pt(110) [24] and Cu(111) [25]. There are also self-organized 2D patterns, e.g. N/Cu(100) and N/Cu(410) [26–28], facetted vicinal Si(111) [29, 30], chessboard superstructure of Br/Cu(100) [31], Pb/Cu(111) [32] and also O/Cu(110) [7], studied in the present thesis. 3D self-organized islands have been found in SiGe/Si films [33]. Some examples of these self-ordered systems are shown in Fig. 1.1.

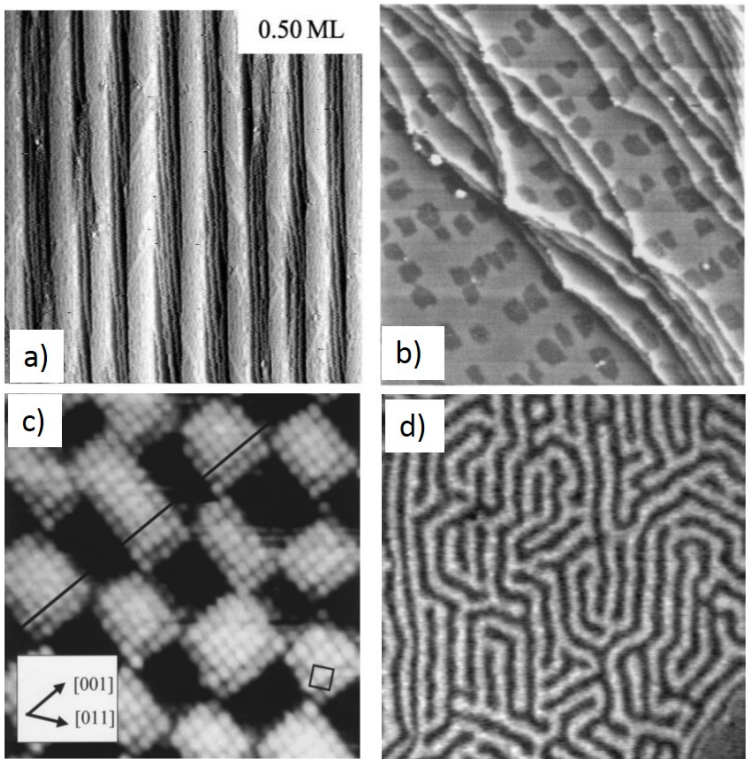

Fig. 1.1: Examples of self-ordered nanostructures from the literature. a) Ag-induced faceting of Cu(111) from Ref. 25; b) N/Cu(100) from Ref. 26; c) Br/Cu(100) from Ref. 31; d) Pb/Cu(111) from Ref. 32.

In some scientific fields the terms self-organization and self-assembly are understood as synonyms. We view the self-organization as a spontaneous process of organization of adsorbates on a substrate, which is driven by the properties of the substrate itself, and we leave the term self-assembly for the organization due to interaction of adsorbates between each other, as is the case in molecular assemblies.

As already mentioned, the self-organization on surfaces is of great interest for nanotechnology. Self-organization and self-assembly at the nanoscale on metallic surfaces has proven to be a valid bottom-up approach to nanostructuring, alternative

to the advanced capabilities of nanolithography [34]. Faceted vicinal surfaces can serve as templates for nanowires, reconstructed surfaces can be used to grow 2D lattice nanostructures. For example the N/Cu(100) system, which spontaneously organizes into a periodic pattern of square islands, can be used as a template for gold nanodots [35]. It has also been shown that one can create ordered magnetic domains with the help of self-ordered substrates [28].

The O/Cu(110) system, studied in the present thesis, has already been used as a template to create ultrathin ferromagnetic Ni films [36] or Ag nanowires [37]. Furthermore, this surface is a possible candidate for an adsorption template in the field of organic molecular electronics and applications such as organic solar cells, light emitting diodes or thin film transistors [8, 9, 11–13]. In the literature the Cu(110)-(2×1)O surface has been used as a template to grow thin films of para-sexiphenyl [8–10], pentacene [11], alpha-Sexithiophene [12] and to adsorb Single Ladder Molecules (SL) [13].

We can discuss in more detail how the Cu(110)-(2×1)O nanostructure can be used as an adsorption template on the example of SL molecules (Fig. 1.2). SL molecules adsorb with their board aligned along the $[1\bar{1}0]$ direction on clean Cu. On the nanostructured Cu(110)-(2×1)O surface, the molecules adsorb exclusively on the bare copper stripes, thus creating well-ordered 1D molecular chains. The main interaction between the molecule and the metal substrate is known to be the van der Waals attractive interaction between the central π board of the SL molecules and the metal. In the case of the oxidized copper stripes, the oxygen partially withdraws the charge density of the copper and the bonding to the substrate is therefore decreased. Large molecules with board longer than the width of a bare copper stripe in the template will change their orientation with respect to the orientation they adopt when adsorbed on a clean Cu surface. An example of the SL molecules adsorbed on the nanostructured Cu(110)-(2×1)O template is shown in Fig. 1.2. The possibility to control the adsorption orientation gives a great advantage over lithography techniques. This example demonstrates that it is possible to employ the O/Cu(110) nanostructure as a template and that with more possibilities to tune the width of the stripes come new possibilities for technical application.

1.2 STM and reactivity studies on nanostructures

In the past, studying reactions on model systems, such as single crystals under UHV conditions, has helped to reveal many fundamental processes, adsorption sites and

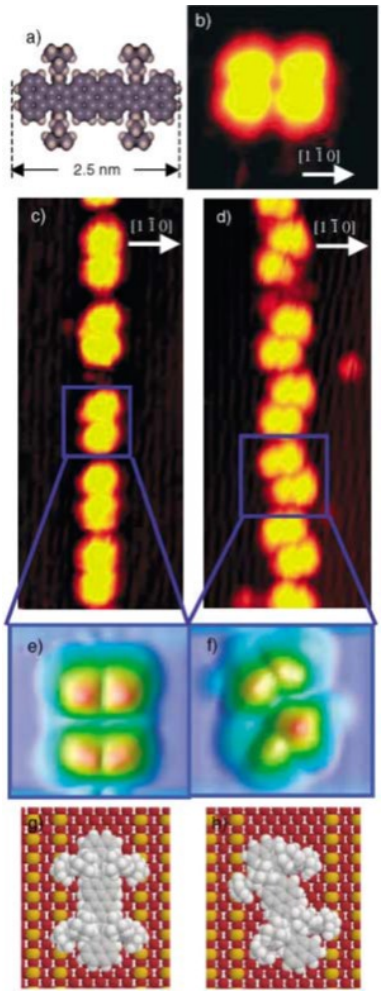

Fig. 1.2: SL molecules adsorbed on the O/Cu(110) template. The image shows the molecular chains formed after being deposited on the nanostructured Cu(110)-(2×1)O surface. The molecules adsorb exclusively on bare Cu stripes and their orientation is aligned with the direction of the stripes. From Ref. 13.

reaction mechanisms even at the atomic scale [38, 39]. The complexity of research increases drastically with the dimension of the surface reducing from the large domain for a uniform surface (single crystal) to the nanometer domain (small clusters). Many research groups dealing with heterogeneous catalysis are interested in the reactivity of supported nanoparticles. Traditionally, they would study single crystals of transition metals in UHV as model systems or try to bridge the so-called material gap between single crystals and real industry catalysts by implementing metal nanoparticles deposited on high surface area oxide supports. Yet such systems show a broad distribution in both particle size and distance between neighboring particles. This is a problem, since the catalytic activity and selectivity is known to depend on the structure of the catalytic active site [40–43]. Therefore such nanoparticles do not represent a good model for the study of this structural influence. Few catalysis groups have therefore chosen to study reactivity of model uniform nanostructured surfaces prepared by nanolithography [44–49]. However these studies were mainly kinetic studies and did not focus on the mechanism of the reaction. Bobrov and Guillemot [50, 51] have studied the reaction of the Cu(110)-(2×1)O-nanostructured surface with water. Their STM study at low temperature (200 K) revealed stages of the reaction mechanism, yet they did not try to modify the surface and study the influence of the dimensions of the oxidized stripes on the reactivity.

The main technique employed within the present thesis is the scanning tunneling microscopy described in detail in section 2.2.2. STM is a very powerful tool for studying local phenomena in reactivity, since we can image steps and defects and also obtain atomic resolution. In surface science, reactions are classically studied by the means of e.g. x-ray photoelectron spectroscopy (XPS), low-energy electron diffraction (LEED), surface x-ray diffraction (XRD) or secondary ion mass spectrometry (SIMS). However STM stands out from these techniques, since it provides the possibility to study a reaction locally. In spite of the obvious advantage of STM in imaging processes at the atomic level, STM image acquisition during a reaction deals with an obstacle due to surface mobility. Most atoms and many molecules are highly mobile at room temperature, therefore STM studies of reactions often require cooling down to temperatures around 150 K or lower.

In the present thesis, one of few STM studies, in which STM measurement has been performed during a reaction, was carried out. We performed STM measurements during exposure to a reactive gas at a pressure up to 10^{-6} mbar. The study of the reactivity of a nanostructure at room temperature and in real time conditions has revealed reaction mechanisms at the atomic scale.

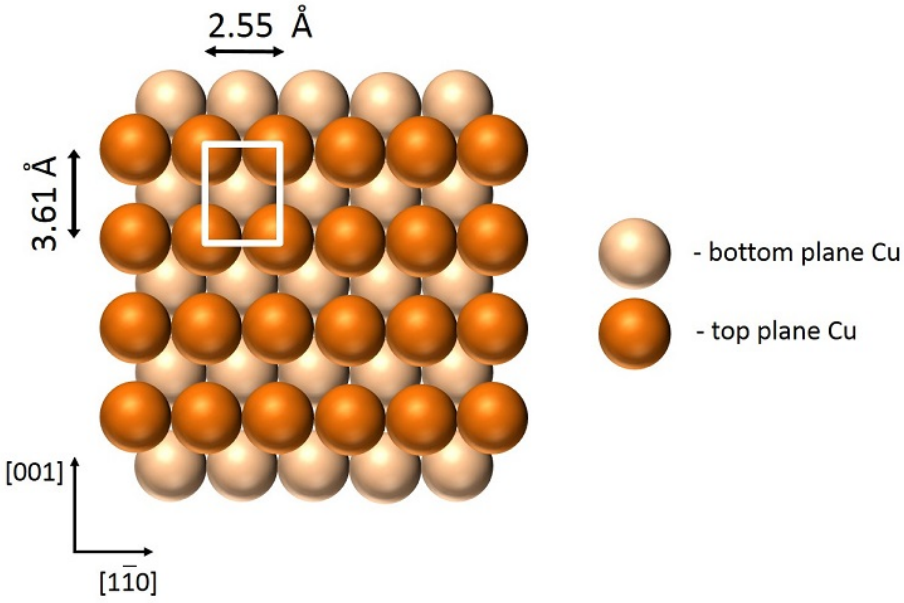

Fig. 1.3: Atomic ball model of Cu(110)

1.3 Cu(110)-(2×1)O nanostructure

This thesis is dedicated to the study of a self-organized nanostructured surface, the Cu(110)-(2×1)O. This surface serves as a model example for a self-organized template with nanodimensions. The following section summarizes the known information about the system from the literature and finally focuses on the objectives of the present study.

1.3.1 Cu(110)

Copper is a transition metal with a face-centered cubic (fcc) lattice and a lattice constant $a = 3.61$ Å. In Fig. 1.3, a ball model of the arrangement of atoms on the (110) plane is shown. The primitive surface unit cell has the dimensions $a = 3.61$ Å and $b = 2.55$ Å. The (110) surface is the most open and therefore the most reactive of all the low-index surfaces. The clean Cu(110) is thermodynamically stable in this unreconstructed state. The LEED pattern of a clean Cu(110) surface is shown in Fig. 1.4.

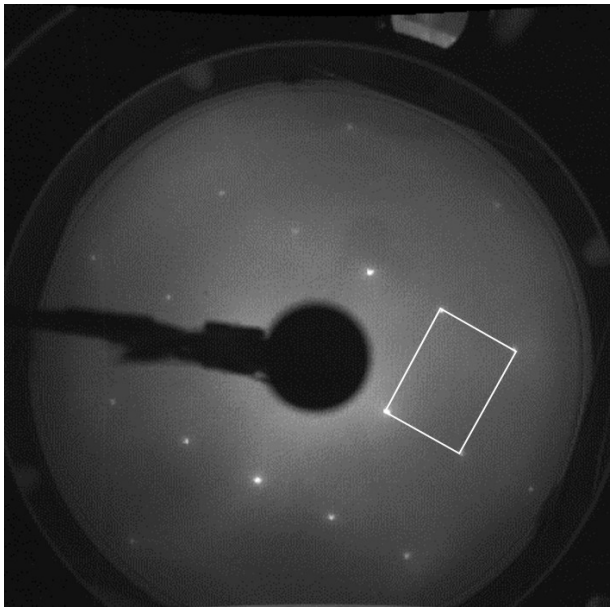

Fig. 1.4: LEED pattern of Cu(110) with the reciprocal unit cell. (Beam energy = 200 eV)

1.3.2 Interaction of Cu(110) with oxygen

Oxygen on Cu(110) has been studied extensively since the pioneering work of Ertl [52], revealing that molecular oxygen chemisorbs dissociatively on Cu(110), and that the LEED pattern shows a (2×1) structure at an O coverage of 0.5 monolayers (ML). A LEED pattern of an oxygen-saturated Cu(110) surface is shown in Fig. 1.5. The half- and integer-order spots of the LEED pattern of comparable intensity indicate a surface superstructure. The adsorbed oxygen is located at the long-bridge sites along the [001] rows [53–56], as seen in Fig. 1.6, which shows the rearrangement of the atoms on the (110) face of Cu after the (2×1) oxygen-induced reconstruction.

The reconstruction, previously believed to be of "missing-row" [57–61], or "buckled-row" [62–66] type, was studied and correctly identified for the first time in 1990 in the parallel work of Coulman, Jensen and Kuk [67–69]. The real mechanism is described as a (2×1) "added-row" reconstruction. A detailed STM analysis was needed to identify the mechanism, since the "added-row" model and "missing-row" model are equivalent at saturation coverage (θ_O = 0.5 ML), but the two differ significantly with respect to the mass transport. While for the "added-row" model, Cu atoms are supplied from step edges, the "missing-row" model would lead to mass transport from terraces to step edges.

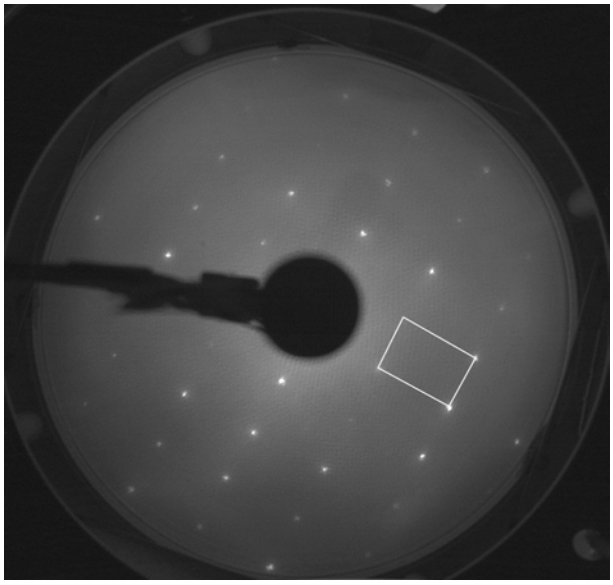

Fig. 1.5: LEED pattern of Cu(110)-(2×1)O with the reciprocal unit cell. (Beam energy = 200 eV)

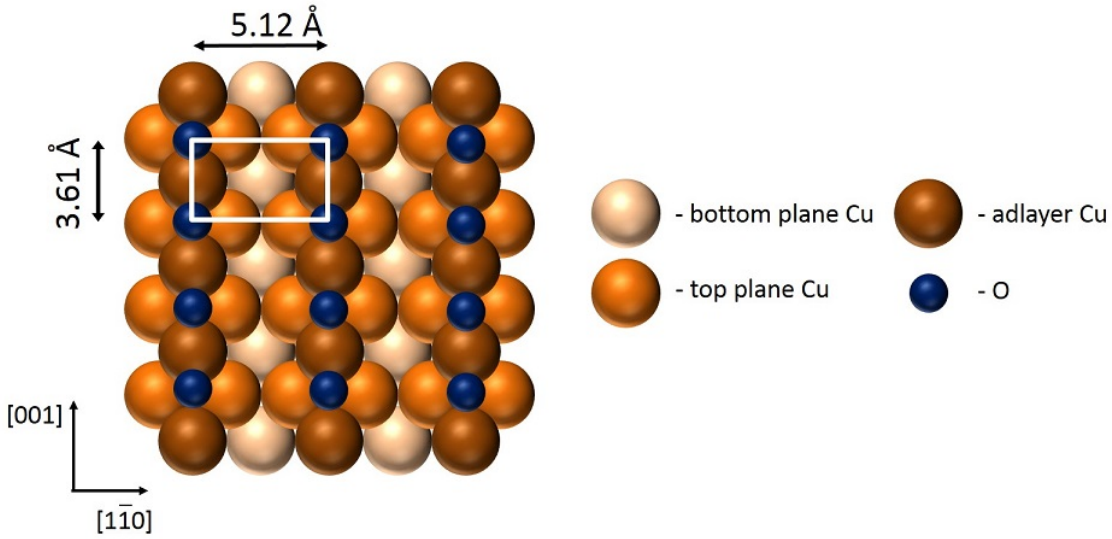

Fig. 1.6: Atomic ball model of the oxygen reconstructed Cu(110)-(2×1)O surface.

The mechanism can be described in detail as follows: At room temperature, adsorption of O_2 will lead to dissociation of the molecule. The atomic oxygen then traps mobile Cu adatoms on the terraces and condenses to form –Cu–O– rows in the [001] direction. This is due to the strong attractive Cu–O interaction along the [001] direction [70]. The source of the Cu adatoms for the "added-row" reconstruction are the step edges, from which the Cu atoms are extracted and diffuse across the surface, as shown in Fig. 1.7. We can see four STM images of the Cu(110) surface during exposure to oxygen at RT. Clearly, during oxygen exposure, Cu atoms are being removed from step edges, and simultaneously –Cu–O– rows are appearing on the surface. There are therefore two steps to the –Cu–O– row formation: the diffusion of Cu atoms from step edges to terraces and the combination of the Cu adatoms with the O atoms. The rate-limiting step is believed to be the supply of Cu adatoms from steps [70–72]. With increasing density of the formed –Cu–O– rows, they agglomerate into (2×1) reconstructed anisotropic islands. The transport of Cu adatoms becomes hindered by the (2×1) islands and their supply from the step edges is restricted by the stabilization of the step edges by the (2×1) rows. If this primary source for the Cu adatoms is blocked by the oxidized stripes, further oxidation will lead to a formation of monolayer deep troughs on flat terraces. The extraction of atoms from this second source is believed to have a much higher activation energy than the extraction from step edges and thus the process is much slower. Such monoatomic troughs have been observed during oxidation of Cu(110) in references 61, 67, 69, 71, 74, 75 and for the first time during oxidation of the pre-oxidized and nanostructured Cu(110) surface in Ref. 76. The formation of the troughs during oxidation proves that it is in fact the presence of oxygen that induces the extraction of Cu atoms. After further oxidation, these troughs were found to be covered by the (2×1)O phase.

In 1991, Kern has studied the formation of the Cu(110)-(2×1)O phase by He diffraction and STM and discovered that at submonolayer coverage and under simple annealing a periodic pattern of alternating clean copper and oxygen stripes is formed [7]. In Fig. 1.8, the He diffraction pattern obtained by Kern is portrayed. Apart from the expected specular peak and the weak and broad half-order diffraction peak at $Q = 1.23$ Å^{-1}, four unexpected diffraction peaks at wave vectors $|Q|= 0.094$, 0.188, 0.283 and 0.377 Å^{-1} showed up. This pattern proved the arrangement of the Cu–O islands into stripes of nearly equal width along the [001] direction, as sketched next to the diffraction pattern.

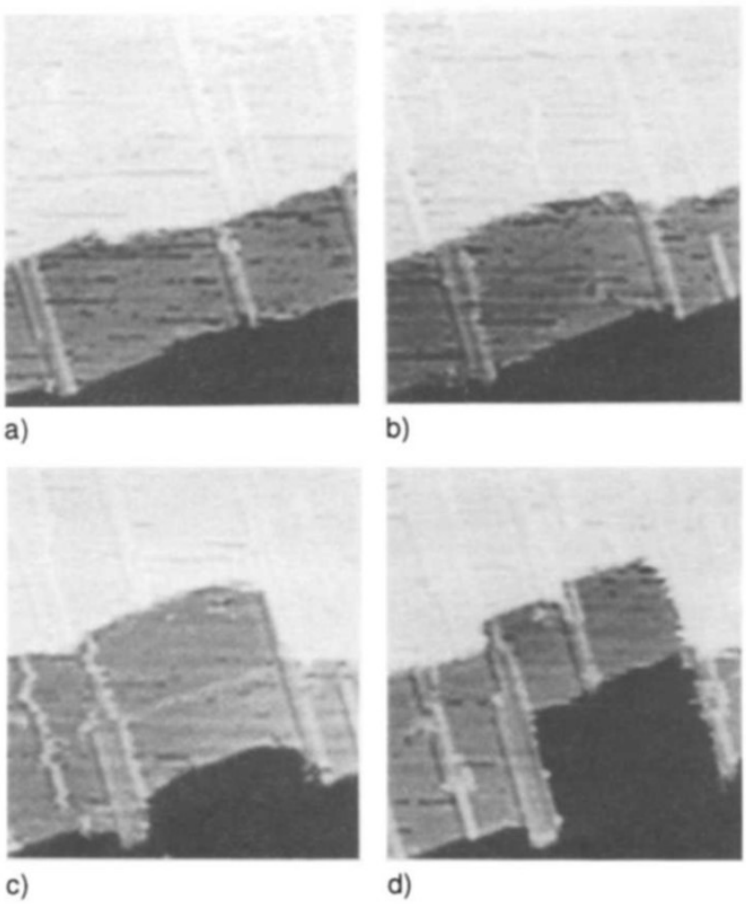

Fig. 1.7: STM images of Cu(110) recorded during oxygen exposure at RT. Attack of the step edges induced by oxygen adsorption. Step edges are the source of Cu adatoms for the –Cu–O– rows. From Ref. 73.

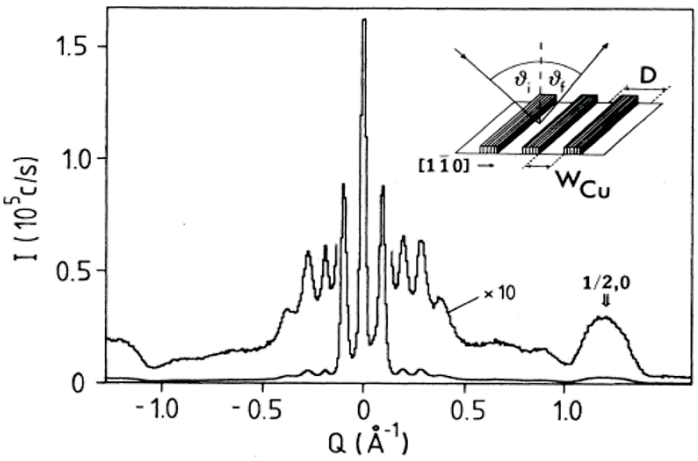

Fig. 1.8: He-diffraction pattern of Cu(110)-(2×1)O from Ref. 7. θ_O=0.28.

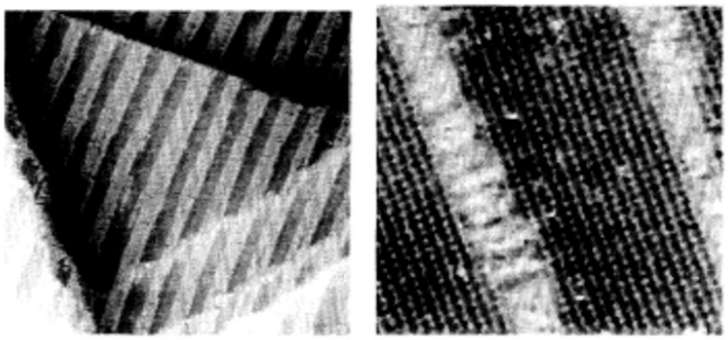

Fig. 1.9: First STM images of the Cu(110)-(2×1)O nanostructure from Ref. 7

Kern has observed periodic supergrating with the periodicity varying between 140 Å and 60 Å and depending on oxygen coverage and temperature, an example of which is shown in Fig. 1.9. For some oxygen coverages the supergrating has been formed already at temperatures $T > 450$ K, while for others the grating has been kinetically hindered below 600 K. Temperature of 640 K has been established as high enough to minimize all kinetic effects. The reported phenomena had not been explained at that time and so it encouraged more experimental [76–83] and theoretical work [79, 84–86]. Today, we know that the self-ordering into a supergrating is driven by elastic interactions and relaxation. The reconstructed Cu(110)-(2×1)O surface is anisotropically strained due to the stress difference between the clean copper stripes and CuO stripes. The formation of the periodic pattern is as follows: At initial stages of oxidation Cu–O chains nucleate on flat terraces due to the strongly attractive short-range interaction between Cu and O in the [001] direction. These chains are mobile on copper and can diffuse over several nanometers. Their mobility decreases significantly, when two or more chains are attached. With increasing oxygen amount, the medium-range attractive forces between Cu–O chains along the $[1\bar{1}0]$ direction induce creation of 2D islands. Finally under thermal annealing the mobility of the islands is enhanced and the surface is rearranged by elastic relaxation due to long-range repulsive interaction into a periodic grating, spatially separating stripes along the [001] direction. The self-ordering of the Cu(110)-(2×1)O system has been described in a theoretical model predicting the dependency of the periodicity on the oxygen coverage. It is thoroughly presented in the following section.

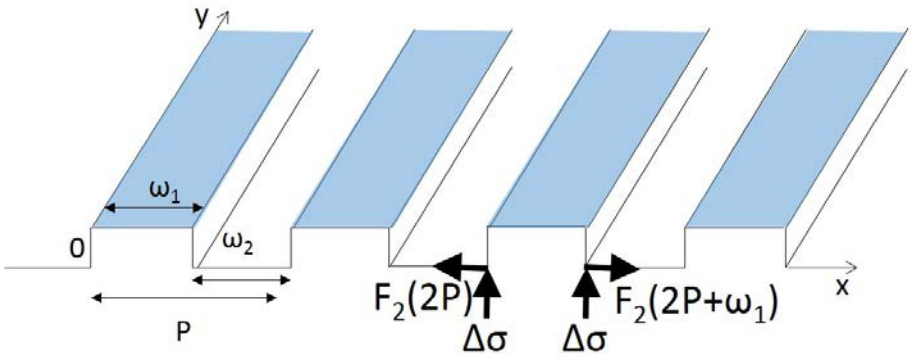

Fig. 1.10: Elastic continuum model: Schematic representation of a stripe phase consisting of two phases 1 and 2 with different intrinsic stress tensors σ_1 and σ_2. The widths of the stripes are ω_1 and ω_2 and the periodicity of the phase is P. The two phases are shown separated by steps for definiteness, but any kind of domain walls can be used for the model.

1.3.3 The Marchenko-Vanderbilt model

The pioneering theoretical work aimed to understand self-organization has been done by Marchenko [87], Alerhand and Vanderbilt [88]. They proposed elastic continuum models which describe the interplay between two opposing forces: the long-range elastic relaxation energy yielded by the underlying crystal and the domain boundary energy. The former is minimum when two phases A and B are as far apart as possible on the surface and the latter is minimum when they are present as a single domain. The result will be an equilibrium between these two states leading to the formation of a pattern.

A sketch for the stripe phase in elastic continuum model is shown in Fig. 1.10. ω_1 and ω_2 are the widths of the stripes and P is the periodicity, given by $P = \omega_1 + \omega_2$. The two coexisting phases on a surface have different values of intrinsic surface stress tensor σ_i, which will induce effective force monopoles F_i, applied to the domain boundaries. These forces will give rise to atomic displacements u_j in the whole crystal due to elastic relaxations. The gain in the elastic energy of the surface S is calculated by integrating the product of forces by displacements:

$$E_{\text{elastic}} = -\frac{1}{2}\int_S \sum_{i,j} F_i u_j \mathrm{d}S \tag{1.1}$$

As visible in Fig. 1.10, the force is acting along the x-direction at the domain boundary. The displacement will appear only in this direction. The force arising from the different intrinsic surface stress tensors is given by:

$$F_i(x) = -\Delta\sigma\delta(x - iP) + \Delta\sigma\delta(x - iP - \omega_1) \tag{1.2}$$

We can define the displacement u_j, which is applied periodically at each domain boundary as:

$$u_j(x) = \frac{(1-\nu^2)\Delta\sigma}{\pi E}\left(\frac{1}{x - jP} - \frac{1}{x - jP - \omega_1}\right) \tag{1.3}$$

Where E is the Young's modulus and ν is the Poisson ratio. Both of these parameters can be determined experimentally. The elastic constant of the system C_{elastic} is defined as:

$$C_{\text{elastic}} = \frac{2(1-\nu^2)\Delta\sigma^2}{\pi E} \tag{1.4}$$

If we consider the stripes of the two phases to have the same length ($\omega_1 = \omega_2$), the coverage Θ will be $\Theta = \frac{\omega_{1,2}}{P} = 0.5$, and we can write the term for the elastic energy as:

$$\Delta E_{\text{elastic}} = -\frac{C_{\text{elastic}}}{P}\ln\left(\frac{P}{2\pi a}\right) \tag{1.5}$$

Where a is the cut-off parameter for the continuum elastic theory and should be in the order of the inter-atomic distance.

There is also an electrostatic interaction due to the difference in the work function of the two phases, $\Delta\phi$. The electrostatic energy will be calculated with the electrostatic constant of the system, $C_{\text{elec.}}$:

$$C_{\text{elec.}} = \frac{\Delta\phi^2}{8\pi^2} \tag{1.6}$$

The total energy that is gained by the relaxation of the system into stripes is the sum of the elastic and the electrostatic energies, however for the case of the Cu(110)-(2×1)O surface, the electrostatic component is negligible. Prévot *et al.* have analyzed the periodic displacement field of this surface by grazing incidence x-ray scattering and compared the results to quenched molecular dynamic simulations and anisotropic linear elasticity calculations [79]. They determined that the elastic constant of this

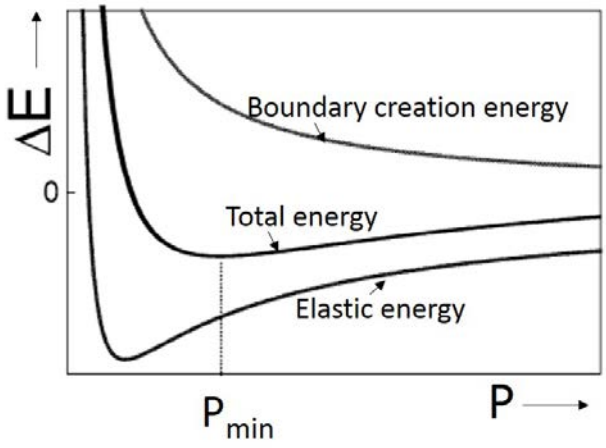

Fig. 1.11: Elastic continuum model: Energy curves adapted from Ref. 28. Bottom: elastic energy, middle: total energy, top: boundary creation energy.

surface is about 10 times larger than the electrostatic constant. This means that the main driving force for the self-ordering is in fact the elastic relaxation.

The total energy of the organized stress domains includes not only the gain of the relaxation energy, but also the energy cost of forming boundaries. The total energy per unit surface area is therefore:

$$\Delta E_{\text{total}} = \frac{\gamma}{P} - \frac{C}{P} \ln\left(\frac{P}{2\pi a}\right) \tag{1.7}$$

where γ is the local boundary creation energy per unit length and C is the sum of the elastic and the electrostatic constants of the system. The curves of the energies as a function of the periodicity are portrayed in Fig. 1.11. Due to the logarithmic dependence of the elastic relaxation energy on the periodicity P (see equation 1.5) we can calculate the minimum periodicity P_{min} by setting $\frac{\mathrm{d}E_{\text{total}}}{\mathrm{d}P}$ to zero:

$$P_{\text{min}} = 2\pi a \exp\left(1 + \frac{\gamma}{C}\right) \tag{1.8}$$

P_{min} exponentially varies with the ratio $\frac{\gamma}{C}$. Until now, we have considered the case where $\Theta = 0.5$. If we allow the coverage Θ to vary, we can calculate that the periodicity equals to

$$P = \frac{P_{\text{min}}}{\sin(\pi\Theta)} \tag{1.9}$$

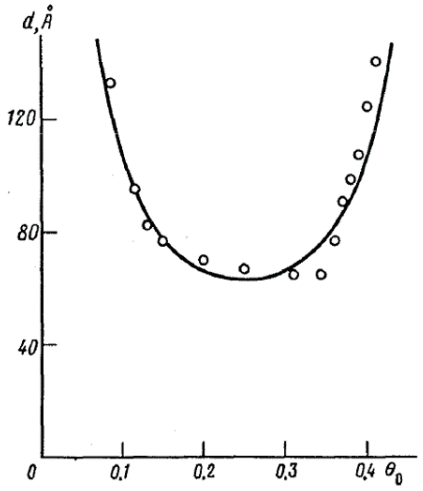

Fig. 1.12: Marchenko-Vanderbilt model from Ref. 84. The agreement of the model with the experimental points obtained by K. Kern [7] is shown.

The function defining the coverage dependency of the periodicity is therefore:

$$P(\Theta) = \frac{2\pi a}{\sin(\pi\Theta)} \exp\left(1 + \frac{\gamma}{C}\right) \tag{1.10}$$

If we use this function for the specific case of the nanostructured Cu(110)-(2×1)O surface, as has been done by Marchenko and Vanderbilt [84, 85], we obtain the curve in Fig. 1.12. In this case the two phases A and B are (2×1)O-Cu and bare Cu(110) phases. Because of the (2×1) reconstruction induced by oxygen, the oxygen coverage at saturation is $\theta_{\mathrm{O}}^{\mathrm{sat.}} = 0.5$ and not 1. The relationship between the coverage Θ, which gives the fraction of the surface covered by one phase and the coverage θ_{O}, which gives the fraction of the surface covered by oxygen atoms is therefore $\Theta = \frac{\theta_{\mathrm{O}}}{\theta_{\mathrm{O}}^{\mathrm{sat.}}}$. For the ratio $\frac{\gamma}{C}$ we calculate with the value 1.09, which was determined using grazing incidence x-ray diffraction by Prévot *et al.* [79]. If we take into account the value for $P_{\min}$ experimentally obtained by Kern of 6.5 nm, we obtain the value for the cut-off parameter $a = 0.13$ nm.

1.3.4 Objectives

As discussed in the introduction, self-organized nanostructures are very important in the field of nanotechnology. Apart from their direct application in electronics, these systems are also very interesting from a fundamental point of view. The self-organized processes need to be deeply understood in order for us to be able to

control them. Tunable self-organized nanostructures represent a relatively easy way to prepare templates with dimensions in the nanometer scale. The Cu(110)-(2×1)O surface is a good candidate for a model system of a self-organized nanostructure, since it is easy to prepare and characterize and has been studied in detail in the past. However this nanostructure is limited, since we cannot obtain different periodicities for the same oxygen coverage and the experimentally accessible periodicities with a good size distribution are only between 6.5 and 11 nanometers. Therefore there is a great interest in finding a way to control the size of the domains. A great effort has been done in this area in a thesis recently completed in our laboratory by Poulain [89]. It has been discovered that the surface electric or electrostatic properties can be changed by co-adsorption of sulfur and therefore the self-ordering process is modified and new nanostructures can be obtained. Poulain has provided proof that the presence of sulfur before the annealing allows to increase the periodicity, yet a systematic study of this process allowing to calculate a model describing the influence of sulfur was still missing and therefore is one of the objectives of the present thesis.

1.4 Interaction of clean and oxidized Cu(110) with sulfur

Chapter 4 deals with results obtained from sulfidation experiments on the nanostructured Cu(110)-(2×1)O surface. The present section is a summary of studies known from the literature on the interaction of copper and oxidized copper surfaces with sulfur. Examples of the reaction with sulfur on other clean and oxidized metals are discussed as well. Lastly, we focus on the objectives of the present study.

The reaction between sulfur and oxygen on metal surfaces is important for many catalytic processes. For example, it has been observed that the selectivity of carbon-free steam reforming of methane can be obtained by the presence of sulfur on the nickel catalyst [90]. On the other hand, sulfur is also a catalyst poison for the industrially important water-gas shift reaction [91, 92] and a poison for corrosion protection [93, 94]. Therefore studying its reaction on metal surfaces is of high importance.

1.4.1 Sulfur adsorption on clean copper

Different structures in which sulfur adsorbs on the (110) face of copper, depending on the concentration of sulfur, have been established. They are, starting from the

lowest concentration: c(2×2), p(5×2) and p(3×2) [95–99]. Other high concentration structures, such as c(8×2), have also been reported [100]. The structures of adsorbed sulfur have been studied by LEED [100, 101], STM [100, 102] and SEXAFS [103]. While the SEXAFS study of Atrei *et al.* showed that, independently of the sulfur coverage, the adatoms occupy the two-fold hollow site on Cu(110) with the same bond length of 2.37 ± 0.03 Å, the STM data of Parker *et al.* favored the model of sulfur adsorption in both hollow and bridge sites. A reconciliation came with the work of Carley [99] in the year 2000. In his STM study, Carley has noticed how sulfur present at low concentrations only became visible on STM images after oxygen co-adsorption. The previously highly mobile sulfur adatoms were hindered by the oxygen chains. The mobility of sulfur is especially enhanced along the $[1\bar{1}0]$ direction parallel to the copper rows, which provides the lowest diffusion barrier. The inability to image sulfur at low concentrations explains the discrepancy between the previous SEXAFS and STM studies.

In the present study, the two low concentration structures of sulfur on Cu(110) have been observed, the c(2×2) and the p(5×2), and therefore are discussed below in more detail.

1.4.1.1 S-c(2×2) phase

At the initial stage of the Cu(110) exposure to sulfur, islands of S in c(2×2) are being formed, which grow with increasing concentration of sulfur to build a complete c(2×2) structure with a primitive cell of 5.1 Å × 7.2 Å, as shown in the atomic ball model in Fig. 1.13. This structure is characterized by antiphase boundaries. The domains are about 14 Å wide and separated from each other by a single substrate unit cell and are out of phase. Such structure considered as a whole has dimensions 12 times the copper lattice in the $[1\bar{1}0]$ direction and 2 times the copper lattice in the [110] direction. An STM image of the c(2×2) phase with antiphase boundaries is shown in Fig. 1.14. This structure corresponds, according to Ref. 99, to a sulfur coverage of $\theta_S = 0.41$. A perfect c(2×2) structure without phase boundaries would represent exactly $\theta_S = 0.5$.

1.4.1.2 S-p(5×2) phase

For sulfur concentrations between 0.41 and 0.62, the p(5×2) structure has been observed. With increasing concentration, the c(2×2) and p(5×2) phases coexist on the surface until reaching concentration of approximately $4.4 - 6.6 \times 10^{14}\,\mathrm{cm}^{-2}$, where only the later phase can be found on the surface. The atomic model of the

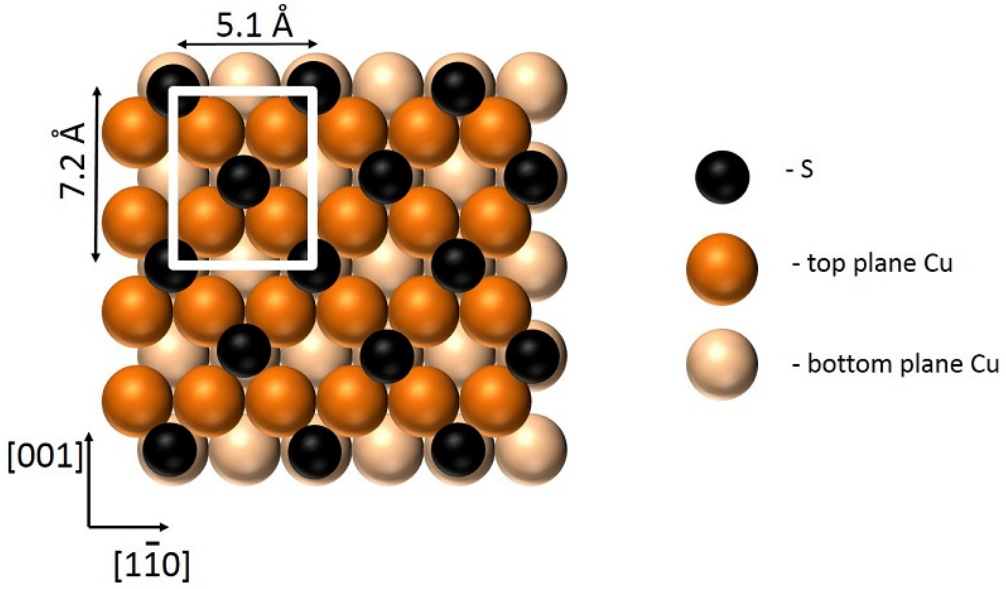

Fig. 1.13: Atomic ball model of S-c(2×2) on Cu(110)

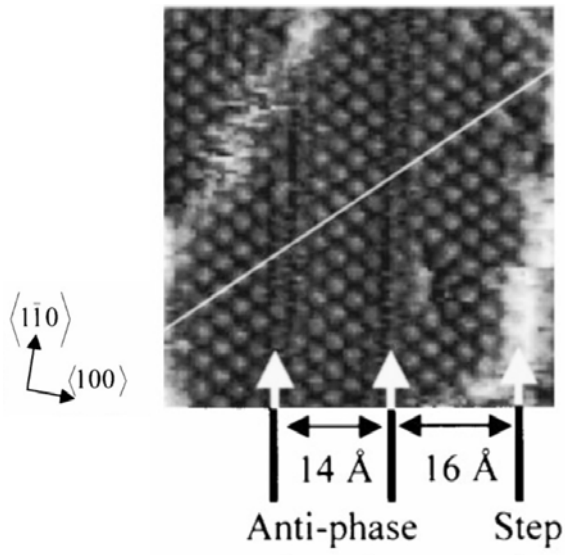

Fig. 1.14: STM image of S-c(2×2) phase with antiphase boundaries from Ref. 99.

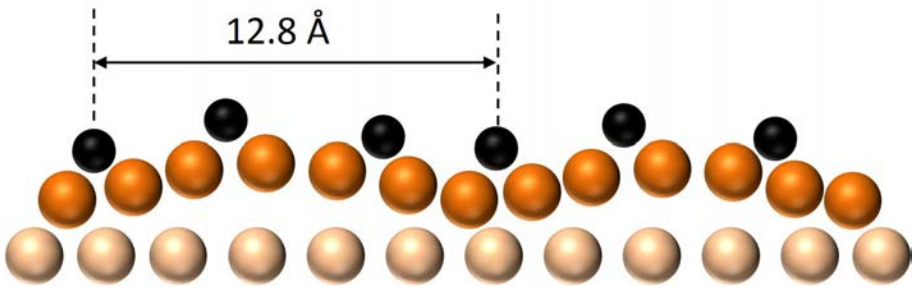

Fig. 1.15: Atomic ball model representing side view of the S-p(5×2) phase adapted from Ref. 99.

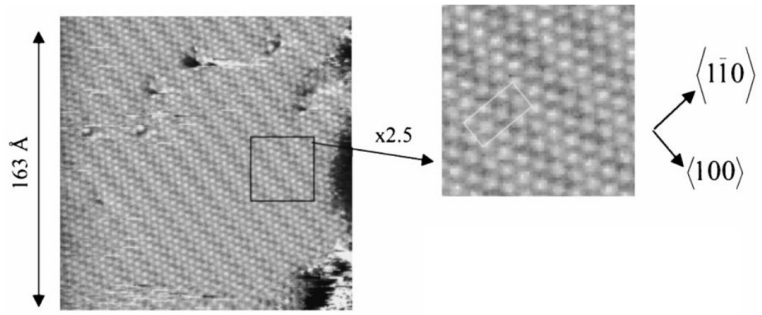

Fig. 1.16: STM image of the S-p(5×2) phase from Ref. 99.

p(5×2) phase is shown in Fig. 1.15. This structure is characterized by a compression of the copper/sulfur layer in the [1$\bar{1}$0] direction, leading to height variation and observed as dark and bright areas in the STM image, as shown in Fig. 1.16. This compression leads to a buckling of the uppermost copper and sulfur adlayer. There is a relaxation of this upper layer away from the second layer and the adsorbed sulfur is locally retained in the two-fold hollow adsorption sites. The copper/sulfur layer is compressed by 16.3%.

1.4.2 Sulfur adsorption on oxidized copper

The reaction of sulfur on oxidized copper surfaces has been previously studied by several research groups [99, 104–110]. Since the mechanism of the reaction is believed to be analogous to the ammonia oxydehydrogenation [99], we will also discuss the experiments dealing with this reaction on copper surfaces [111–115]. In the present thesis, we have chosen to study the H_2S adsorption on the nanostructured Cu(110)-(2×1)O. Despite the many studies in this field, no previous study of the reactivity of this surface with tunable dimensions has ever been performed.

Early studies of oxygen covered metal surfaces have established that chemisorbed oxygen can activate bonds in reactants, such as water, hydrocarbons, ammonia and hydrogen sulfide, and promote their reaction [116–119]. They have shown that oxygen activates the bonds in the adsorbates through H-abstraction. In general, it has been found that the oxygen atoms present either isolated or at the periphery of copper-oxygen chains or oxygen islands are most active towards the oxydehydrogenation. In fact, a completely oxygen-saturated copper surface has been found to be inactive towards the reaction with ammonia [111]. However such surface has been found active for the reaction with hydrogen sulfide. The reaction undergoes transient stages, but the total reaction equation can be written down as:

$$H_2S + O_{ad} \longrightarrow S_{ad} + H_2O \uparrow$$

H_2S reacts with pre-adsorbed oxygen on metal surfaces by formation of water, which desorbs at RT, leaving adsorbed S. This reaction has different activation energy depending on the supporting metal. On Cu(110) desorption of H_2O has been detected at temperatures above 120 K [107], while on Ni it is 235 K [120], 96 K on Pt [121] and only 85 K on Pb [116].

Sulfur adsorbs on the previously oxidized metal surface in the same structure as on a clean one and therefore the same phases, c(2×2) and p(5×2), will be observed at saturation. The reaction of the oxygen-saturated surface with hydrogen sulfide is initiated at defect sites in the (2×1)O overlayer and step edges. During the reaction between H_2S and O on another fcc metal, namely nickel, Ruan *et al.* [122] have observed, how the flat reconstructed (2×1)O covered surface changes to a rough surface with many small islands and troughs covered with the c(2×2) phase. With longer exposure this intermediate phase is substituted by a thermodynamically stable (4×1)S reconstructed phase. The formation of this phase at room temperature is surprising since this process has previously been observed only when activated by higher temperatures [123, 124]. Apparently, the rough surface has a higher surface energy than the flat S-c(2×2) surface and thus the energy barrier for sulfur to react with the surface is reduced. In contrast to Ni(110), the reaction on Cu(110) is heterogeneous and the S-c(2×2) domains are larger. This is due to the diffusivity of Cu, which is significantly higher than that of Ni and thus the Cu from the (2×1) added rows agglomerates into larger islands onto which sulfur chemisorbs.

1.4.3 Objectives

The first objective of the present thesis was to study a new preparation method for the Cu(110)-(2×1)O nanostructure, which allows to tune the periodicity. New perspectives for this system are being opened, as we can now choose the parameters P and θ_O, which are no more dependent on each other. We are therefore able to test the influence of the structure on the reactivity with model reactions. Showing that we can control a reaction by changing the morphology of the surface is very important for both the field of heterogeneous catalysis and corrosion protection. The model reaction we have chosen is the sulfidation. The objective of this thesis was to study the mechanism and reactivity of H_2S adsorption on the Cu(110)-(2×1)O nanostructures prepared by the new method with different periodicities but the same oxygen coverage, and thereby to directly study the influence of the morphology on the reactivity of the copper surface.

1.5 Surface diffusion of large clusters

Chapter 5 is dedicated to the study of the surface dynamics and diffusion mechanisms of islands on the Cu(110) surface. Here we briefly introduce the theoretical concept of surface diffusion for large clusters.

Real crystalline surfaces are generally not in equilibrium, but are covered by clusters of adatoms and vacancies, also called islands and pits. In order to reach an equilibrium, the surfaces will relax, via different ripening mechanisms. The driving force for the redistribution on the surface will be the tendency to minimize the total surface energy. By redistributing the material into fewer islands (in the ideal limit into one single island), the free energy cost associated with the island edges is reduced and the total free energy therefore minimized. One of the mechanisms of coarsening is the so-called Ostwald ripening, originally observed for grains in a solution [125], which involves diffusion of atoms from small clusters towards the large ones. A theory based on this observation has been developed by Lifshitz, Sloyozov and Wagner [126, 127] and applied to surfaces by Chakraverty, Wynblatt and Gjostein [128, 129]. While in the past, experimental techniques only allowed the observation of the size distribution of the ensemble of clusters, with use of the modern techniques, such as STM, one can follow locally the dynamic evolution of a single cluster. The diffusion process, known as Ostwald ripening, can be theoretically described with the help of the Gibbs-Thomson equation. When we are considering a decaying island of adatoms,

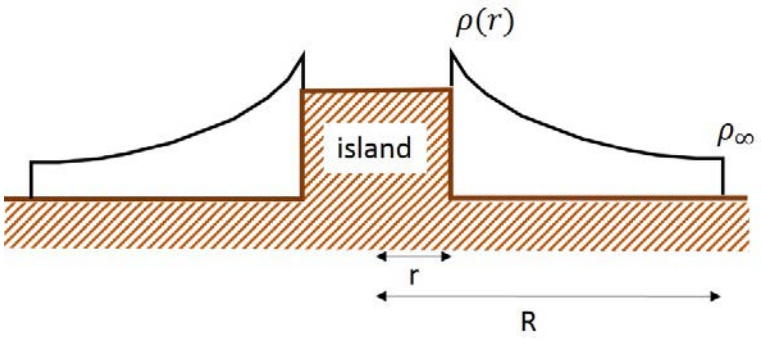

Fig. 1.17: Model for island decay: Schematic representation of an island and adatom concentrations in the surroundings

there is a flux of atoms from the island to the environment and *vice versa*. The steady state average net current away from the island can be described as:

$$J = \kappa \, \Delta\rho \tag{1.11}$$

where κ is a rate constant and $\Delta\rho = \rho_{\mathrm{eq}}(r) - \rho_\infty$ is the driving force for the decay. $\rho_{\mathrm{eq}}(r)$ is the equilibrium adatom concentration of an island with the radius r and ρ_∞ is the equilibrium concentration of the environment, which is reached at a radial distance R from the center of the island, as shown schematically in the model of the Fig. 1.17. The Gibbs-Thomson relation for the equlibrium concentration is:

$$\rho_{\mathrm{eq}}(r) = \rho_\infty \, \mathrm{e}^{\frac{\gamma}{kTn_s r}} \tag{1.12}$$

where k is the Boltzmann constant, T is the temperature, n_s is the atomic density at the surface and γ the line tension. The Gibbs-Thomson relation successfully predicts the behavior on a surface with islands of different sizes. Adatoms will diffuse away from high curvature islands, towards low curvature islands. In this process, two cases can be distinguished: either the limiting step is the detachment of the adatoms from the island ("interface limited") or mass transport between the islands ("diffusion limited"). For islands on metal surfaces, the diffusion limited case is expected, for which $\kappa = 2\pi a^2 v_D / \ln(R/r)$, where a is the lattice constant and v_D is the adatom diffusion frequency.

The decay of an adatom island can be expressed as:

$$J := -n_s \pi \frac{\mathrm{d}r^2}{\mathrm{d}t} = \frac{2\pi a^2 v_D \rho_\infty}{\ln(R/r)} (\mathrm{e}^{\frac{\gamma}{kTn_s r}} - 1) \tag{1.13}$$

Approximations have been made to the classical model based on the Gibbs-Thomson equation, which lead to a general power scaling relation [130, 131]:

$$r \propto (t_{\mathrm{f}} - t)^{\beta} \tag{1.14}$$

where t_{f} is the time at which the island disappears. The exponent β depends on the driving force governing the mass transport. In theory, its value is 1/3 for diffusion limited decay and 1/2 for interface limited decay. The assumptions that lead to the former power law are that the islands are small, the effect of the local adatom environment surrounding the islands is negligible and the step energies are isotropic.

Next to the Ostwald ripening, the second coarsening mechanism is the dynamic coalescence, also called Smoluchowski ripening. The name has been given after Smoluchowski, who was the first to formulate a kinetic theory of coarsening via dynamic coalescence for colloid particles [132]. A general scaling relation for the diffusion coefficient D, $D \propto L^{-n}$, with L being the island's side length, has been established [133–137]. The theoretical values for the 3 main island diffusion mechanisms are: $n = 1$ for evaporation and condensation, $n = 2$ for terrace diffusion limited movement of islands (correlated EC) and $n = 3$ for diffusion via mass transport along the island periphery. Experimentally obtained values are mainly noninteger since the diffusion depends on the exact island form and is influenced by the macroscopic surface structure as well as point defects.

Both processes, Ostwald and Smoluchowski ripening, are faster for smaller islands. The main difference is that while the mass transport during Ostwald ripening is driven by the chemical potential difference between islands of different size, the mass transport during the Smoluchowski ripening is only a result of two islands accidentally colliding and combining.

1.5.1 Objectives

In this thesis, we have used the nanostructured Cu(110)-(2×1)O surface as a template for sulfidation. As a result, we have created large clusters of Cu adatoms on which sulfur is adsorbed, which we call S-c(2×2) islands, according to the phase of sulfur. These islands have been found to be mobile at room temperature.

It is generally believed that the controlled use of growth kinetics may provide a valuable tool for the fabrication of nanostructures of various shapes and sizes. Furthermore, in order for nanostructured surfaces to act as templates in nanofabrication, they have to be stable over a long period of time. The stability and dynamic evolution

of nanostructures is therefore both scientifically and technologically significant. The third objective of the present thesis was to analyze the surface diffusion mechanisms of the S-c(2×2)/Cu(110) system, until an equilibrium is reached.

Chapter 2

Experimental

This chapter describes the ultra high vacuum setup used in the present thesis and also explains the working principles of the used surface science techniques, namely, scanning tunneling microscopy (STM) and Auger electron spectroscopy (AES). The sections 2.3 and 2.4 deal with the sample and tip preparation, respectively. The section 2.5 describes the use of STM in praxis. In the final section, the experimental conditions of all performed experiments are given.

2.1 Experimental setup

All experiments performed during this thesis were carried out in ultra high vacuum (UHV) conditions in an experimental setup, consisting of two interconnected UHV chambers, preparation chamber and STM chamber, with base pressure of 10^{-10} mbar. The preparation chamber is equipped by facilities to perform AES (Omicron, NGE52 with analyzer - CMA100), LEED (Riber, OPD-304) and to bombard (Varian, 981-2043) and anneal (Omicron) the sample. The employment of LEED has been limited to occasionally verifying the surface quality and therefore its functioning will not be described in more detail. The STM chamber is equipped with a scanning tunneling microscope (Omicron, STM1 with SCALA control system).

The UHV setup is portrayed in a photographic image in Fig. 2.1 and schematically in Fig. 2.2. A carefully prepared sample can be introduced to vacuum via the introduction load lock. This part of the system is pumped by a turbomolecular pump (Edwards) and the pre-vacuum is provided by a rotary vane pump (Edwards). Once the sample is in vacuum, it can be transferred by a transfer rod into the preparation chamber, where surface preparation as well as the experiments are carried out. The

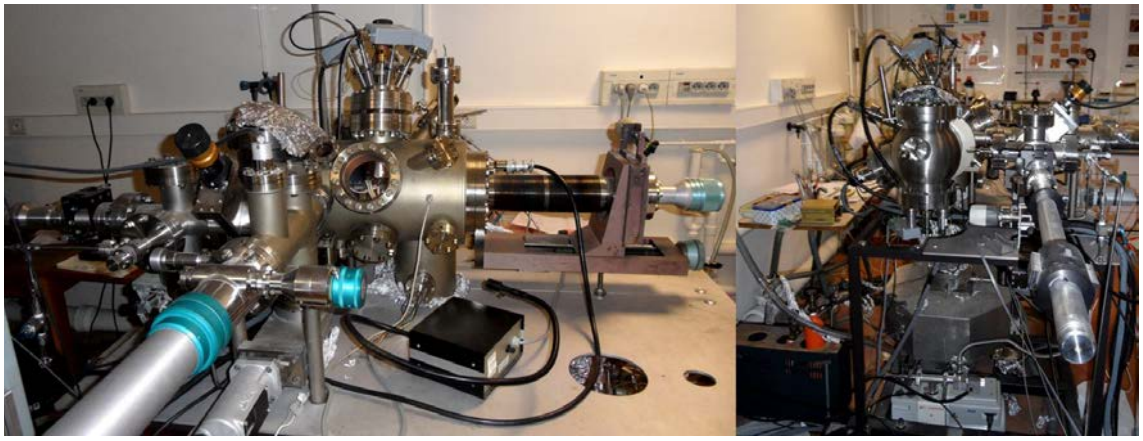

Fig. 2.1: Photographic images of the UHV setup: front and side view

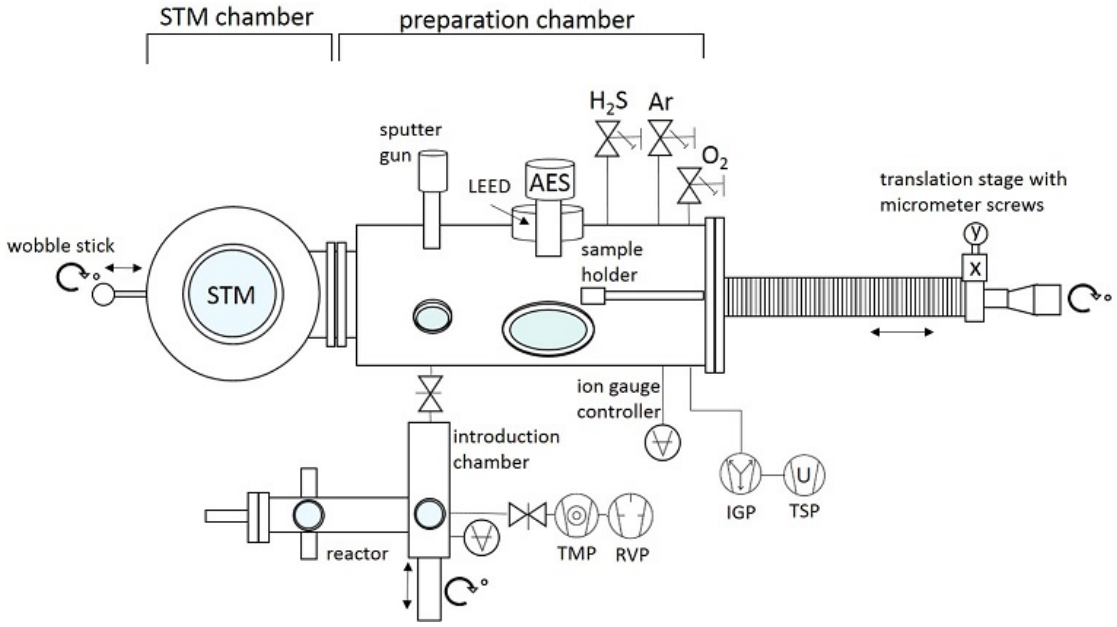

Fig. 2.2: Schematic image of the UHV setup. TMP-turbo molecular pump, RVP-rotary vane pump, IGP-ion getter pump, TSP-titanium sublimation pump.

vacuum in this part is provided by an ionic pump (Riber, model 401-1000) connected with a titanium sublimation pump (Meca 2000). The pressure in the chamber can be controlled by an ion gauge controller (Arun Microelectronics, model PGC2D). The sample can be treated by Ar^+ sputtering and annealing and thus the cleanliness of the surface can be reestablished after each experiment. For this purpose a sputter gun from Varian (model 981-2043) is attached to the chamber. The high purity Ar-gas (N56), as well as O_2 and H_2S (N25, Alphagaz), used during the experiments, can be introduced into the chamber by precision leak valves. The sample placed in a sample holder can be moved inside the chamber by a translation rod and a manipulation stage with micrometer screws. The sample can thus be placed in front of the sputter gun, in front of LEED or AES. For STM measurements the sample has to be transferred together with the sample holder to the STM chamber. The preparation chamber is connected with the STM chamber by a narrow tunnel. The transfer is done by a wobble stick which has the form of a crane and can grab the sample or tip holder. In the STM chamber there is also a carousel for parking samples and tips. The tips and samples can thus be exchanged without breaking the vacuum. The UHV setup also has a reactor part for experiments in high pressure, which has not been employed in present work.

2.2 Methods

2.2.1 Ultra high vacuum

Many surface science studies require vacuum for two principal reasons: to avoid interactions of the probe and detected particles (electrons, ions, atoms etc.) used by the experimental technique with the gas phase molecules and to ensure atomically clean surfaces during the experiments. We will now try to evaluate what kind of pressure is needed to fulfill these conditions.

The collision free condition is fulfilled, when the mean free path, λ, of the particles in the vacuum is significantly greater than the distance from the source to the sample and from the sample to the detector. The mean free path, which is the distance a particle can travel on average without a collision, is given by:

$$\lambda = \frac{kT}{\sqrt{2}P\sigma}, \tag{2.1}$$

where P is the pressure, k is the Boltzmann-constant, T is the temperature and σ is the collision cross section. We can hereby evaluate that the pressure needed to

avoid collisions with the residual gas molecules for the distance of 1 m (calculating with σ of the order of 10^{-19} m^2) at room temperature, has to be lower than 10^{-4} mbar. However, lower pressures are often required in order to extend the lifetime of the detector (channeltron, multiplier detector). To evaluate the order of vacuum necessary to fulfill the clean surface condition, we need to be able to estimate how fast a surface will be covered by contaminations from the gas phase in certain conditions. For successful surface science experiments we need the time after which the surface will be covered by a monolayer (ML) of contaminations to be in the order of hours. Assuming the sticking probability to be one and the ML coverage to be 10^{19} per m^2, the time it takes to build up one ML is proportional to $10^{19}/F$, where F is the incident flux on the surface, which is related to the gas density above the surface by:

$$F = \frac{1}{4} n \bar{c}, \tag{2.2}$$

where n is the molecular gas density and $\bar{c}$ is the average molecular speed. The molecular gas density is given by the ideal gas equation:

$$n = \frac{P}{kT} \tag{2.3}$$

where P is the gas pressure, k is the Boltzmann constant and T the temperature. The average molecular speed obtained from the Maxwell-Boltzmann distribution of gas velocities is equal to:

$$\bar{c} = \sqrt{\frac{8kT}{M\pi}} \tag{2.4}$$

where M is the molecular mass. The combination of the three equation gives us the Hertz-Knudsen formula:

$$F = \frac{P}{\sqrt{2\pi MkT}} \tag{2.5}$$

With the help of these formulas we can estimate that at the pressure of 10^{-6} Torr, a surface will be covered by a monolayer in roughly 1 second, while at the pressure of 10^{-10} Torr, this will take around 2.75 hours. In order to have an atomically clean surface for several hours we will need to work at a pressure typically lower than 10^{-10} Torr. The amount of gas to which a surface has been exposed to is defined as gas exposure, and given in Langmuir (L) where 1 L = 10^{-6} Torr $\times$ s.

Table 2.1: Variation of parameters with pressure. Values given are approximate and dependent on factors such as temperature, molecular mass and sticking coefficient.

Degree of vacuum	Typical pressure (Torr)	Mean free path (m)	Time/ML (s)
Atmospheric	760	7×10^{-8}	10^{-9}
Low	1	5×10^{-5}	10^{-6}
Medium	10^{-3}	5×10^{-2}	10^{-3}
High	10^{-6}	50	1
Ultra high	10^{-10}	5×10^{5}	10^{4}

In the table 2.1, the approximate values of the mean free path and the time it would take to form a monolayer on the surface for certain degrees of vacuum are given. To briefly summarize, the requirements for typical experiments in surface science are a pressure lower than 10^{-4} Torr for useable collision free conditions, and pressures lower than 10^{-10} Torr to maintain a clean sample surface for several hours.

The experiments of the present thesis have been carried out in an ultra high vacuum (UHV) system. We call a vacuum "UHV" for pressures lower than 10^{-9} mbar (1 Torr = $\frac{1013.25}{760}$ mbar).

2.2.2 Scanning tunneling microscopy

Scanning tunneling microscopy (STM) is a powerful tool in surface science, whose strong point is undoubtedly its ability to resolve a surface structure at the atomic scale and in real space. Together with single crystals and UHV conditions, it provides an optimal system to study fundamental processes on metal surfaces, such as reaction mechanisms, atomic diffusion or adsorption and desorption processes. STM has been developed by Binnig and Rohrer, two physicists of the IBM Research Division, in the beginning of the 1980s [138, 139]. In 1986 they have been awarded the Nobel Prize for their design of the scanning tunneling microscope. The basic operational principle of STM is schematically portrayed in Fig. 2.3. An atomically sharp metal tip, which can be made of for example W, Au, Rh/Ir or Pt/Ir, is used to raster a conductive surface. It is brought to a distance of a few Ångstroms from the surface, so that a tunneling current can pass through the gap, if a bias voltage is applied to the sample. The principle of tunneling will be described later in detail. If the tip is grounded, then the bias voltage V, is the sample voltage. If $V > 0$, the electrons tunnel from the occupied states of the tip into the empty states of the sample and if $V < 0$, the electrons tunnel from the occupied states of the sample into the empty

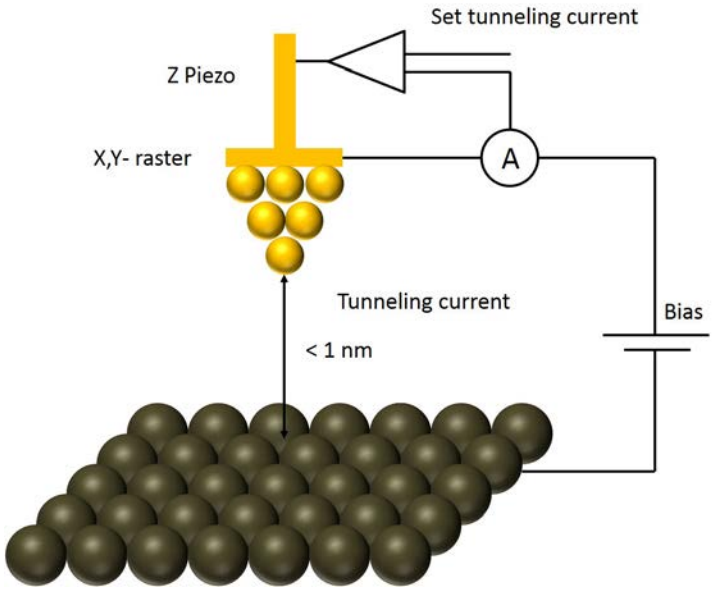

Fig. 2.3: Working principle of a scanning tunneling microscope

states of the tip. The tip is placed on piezoelectric rods, usually fabricated from lead zirconium titanate, which contract and expand according to the voltage applied. This allows very fine adjustment of the tip position (precision better than 0.01 Å), allowing the tip to keep constant tunneling current during the scanning. If the absolute value of the tunneling current is larger than a reference value, a voltage is applied to the z piezo so that the tip is withdrawn from the sample surface and *vice versa*. Alternatively, the constant height mode can be used for STM measurements. In this case, the vertical position of the tip is constant and the tunneling current is the signal. The two modes of STM, constant-current and constant-height mode, are portrayed schematically in Fig. 2.4. The constant-height mode is fast, but only provides reasonable images for flat surfaces. For detecting rougher surfaces with precision, the constant-current mode is advised. In the recorded STM images, the protrusions will be imaged with a lighter contrast and the depressions will be darker. However, one has to keep in mind that the tip will move further away from the surface to keep the tunneling current constant when the imaged surface species is more conductive than the rest of the surface. Therefore STM does not show the real topography of the surface, but a function of the electronic state of the surface and the tip.

STM measurements are highly dependent on the behavior of the piezoelectric elements and are sensitive to the non-linearity between the applied voltage and the displacement. Effects, such as temperature dependence, depolarization, hysteresis

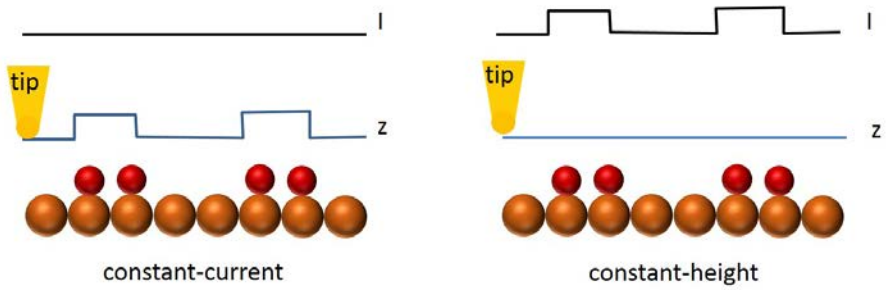

Fig. 2.4: Schematic representation of the constant-current and the constant-height modes of STM. In the constant-current mode, the signal is the tip height, z. In the constant-height mode the signal is the tunelling current, I.

effects or creep, can cause images to be stretched or compressed and a calibration is needed, if true dimensions are to be extracted from STM images. There are different methods for the calibration of an STM with respect to the movement of the piezoelectric elements. For example for observation of hysteresis loops we can employ an inductive displacement transducer or a Michelson interferometer [140]. Known technique for STM calibration is also the detection of the reciprocal unit cell in Fourier space for estimating the lateral calibration factors and the drift in the fast scanning direction, developed by Jorgensen *et al.* [141]. In our praxis we calibrate by scanning a material with well defined and known dimensions and by comparing these with the dimensions actually measured by the STM, we can determine the factor by which the scanning parameters have to be altered. For example for calibrating our STM in the z-direction we have measured a profile over several steps and divided the measured height difference by the number of steps. By measuring an average over several steps, and not only one, we minimize the error. Finally, we adjust our height measurements so that the measured height of a monoatomic copper step corresponds to the theoretical value of 128 pm.

Vibration isolation is another essential factor if atomic resolution is to be reached. This is why short tips are more suitable than long ones for STM measurements. Furthermore the STM itself has to be placed on a table protected from vibrations, such as air support table, where heavy plates rest on inflated supports. Small STM setups used for measurements in air can be suspended by rubber bands or springs. STM systems in UHV can be suspended from the chamber using springs with eddy current dampers. Other damping systems can for example be composed of piezoelectric actuators, stack of metal plates with Viton sandwiched between the plates or shape memory alloys [142]. The working principle of the eddy current

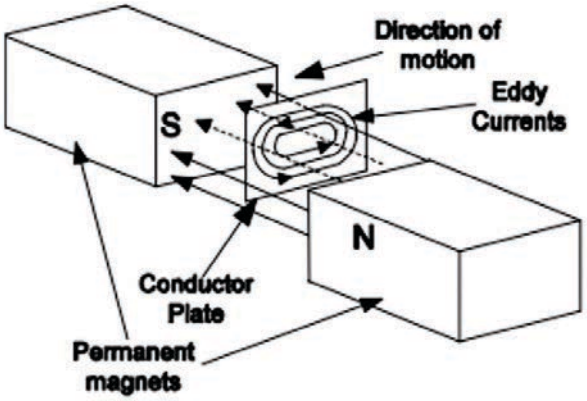

Fig. 2.5: Principle of eddy current damping [142]

damping, which is employed in the STM system used in this thesis is shown in Fig. 2.5.

Eddy currents are generated when a non-magnetic conductive metal is placed in a magnetic field. These currents circulate in such a way that they induce their own magnetic field with opposite polarity of the applied field, causing a resistive force. However, due to the electrical resistance of the metal, the induced currents will be dissipated into heat and the force will disappear. The ideal configuration is when the conductive metal is directly between two oppositely poled magnets with the metal moving perpendicular to the magnets poling axis, because the magnetic field is concentrated between the two magnets causing the magnetic flux applied to the conductor to be greater and thus the damping force to be increased.

Tunneling effect

The principle of STM is based on the quantum mechanical phenomenon of tunneling. The quantum theory says that electrons have a finite probability to tunnel through a barrier, which could not be crossed if only classical laws of physics were being considered, and therewith produce the tunneling current. Such a barrier is the vacuum gap between the tip and the sample. The tunneling effect is schematically portrayed in Fig. 2.6.

We will now present different approximations which can be used, when modeling STM. First, there is the approximation using the one dimensional Schrödinger equation. Secondly, the Tersoff and Hamann method, based on the Bardeen's

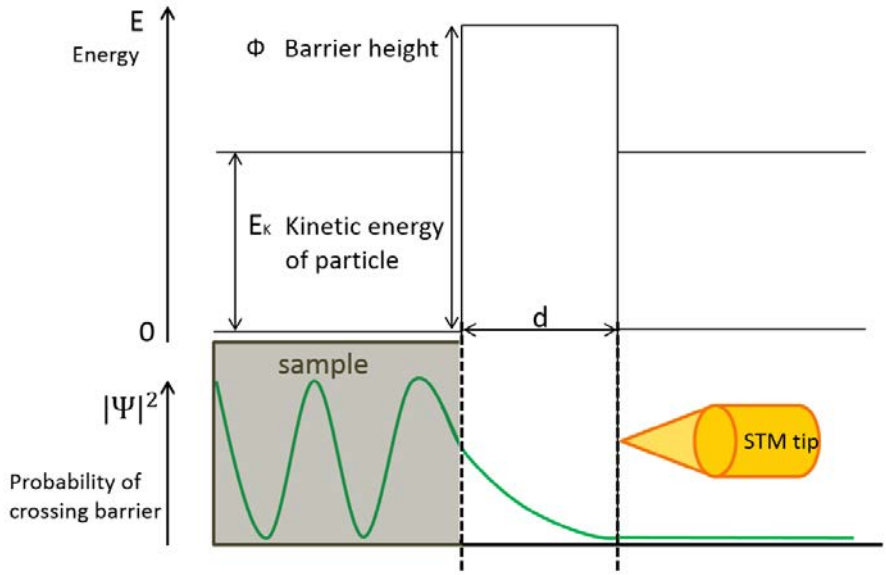

Fig. 2.6: Diagram representing the quantum mechanical tunneling effect between STM tip and sample. The probability P (shown at the bottom) of a particle with kinetic energy E_k tunneling through a potential barrier (shown at top) is plotted as a function of the distance between the sample and the tip. Adapted from [143]

approach, which describes the problem between a wave function of an atom and a surface.

The quantum mechanical tunneling can be mathematically described using the one-dimensional time-independent Schrödinger equation as a first approximation:

$$-\frac{\hbar^2}{2m}\frac{\mathrm{d}^2}{\mathrm{d}x^2}\Psi(x) + V(x)\Psi(x) = E\Psi(x) \tag{2.6}$$

where x stands for the distance measured in the direction of motion of the electron, Ψ is the Schrödinger wave function, m is the mass of an electron, $\hbar$ is the reduced Planck's constant and V is the potential energy of the electron. In Fig. 2.7 the wave function tunneling through a potential barrier of the width α is represented. In order to calculate the probability of the electron crossing the barrier from region I to region III, one needs to solve the Schrödinger equation for each individual region. The wave function solutions are as follows:

$$\Psi_\mathrm{I} = \mathrm{e}^{\mathrm{i}kx} + A\,\mathrm{e}^{-\mathrm{i}kx}, \qquad k = \sqrt{\frac{2mE}{\hbar^2}} \tag{2.7}$$

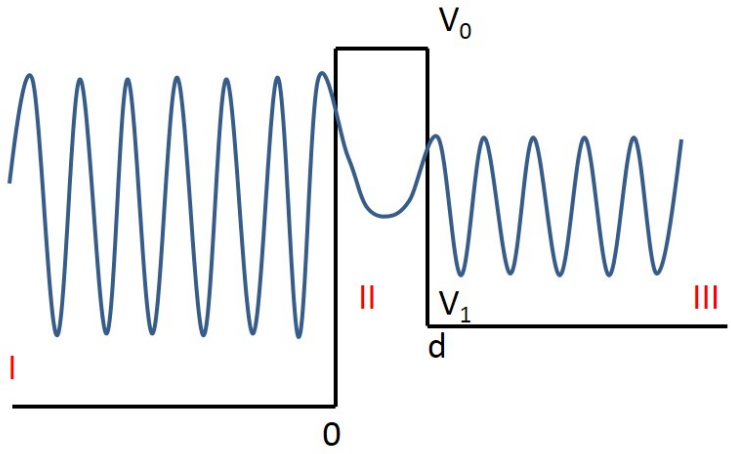

Fig. 2.7: Wave function tunneling through 1D rectangular potential barrier of width d

$$\Psi_{\mathrm{II}} = B\,\mathrm{e}^{\omega x} + C\,\mathrm{e}^{-\omega x}, \qquad \omega = \sqrt{\frac{2m(V_0 - E)}{\hbar^2}} \tag{2.8}$$

$$\Psi_{\mathrm{III}} = D\,\mathrm{e}^{\mathrm{i}qx}, \qquad q = \sqrt{\frac{2m(E - V_1)}{\hbar^2}} \tag{2.9}$$

The coefficients A, B, C and D are given by the boundary conditions, considering that the wave function and the derivatives should be continuous. Further we can define the current density j:

$$j = \frac{\hbar}{2\mathrm{i}m}\left(\Psi^* \frac{\mathrm{d}\Psi}{\mathrm{d}x} - \frac{\mathrm{d}\Psi^*}{\mathrm{d}x}\Psi\right) \tag{2.10}$$

If the transmission, T, equals to $\frac{j_{\mathrm{III}}}{j_{\mathrm{I}}}$, the calculations lead to:

$$T = \frac{(2\omega)^2 kq}{\omega^2(k+q)^2 + (\omega^2 + k^2)(\omega^2 + q^2)\sinh^2 \omega d} \tag{2.11}$$

We can apply this simple "electron tunneling through a barrier" model to STM if we consider that the barrier width corresponds with the tip-sample distance and its height with the work function. In the case of STM the typical distance is few

Ångstroms and the work function around 5 eV, so that the sinh term becomes dominant and we find the dependence:

$$T \propto e^{-2\omega d} \tag{2.12}$$

To derive a general formula for elastic tunneling we start with the so-called Fermi's golden rule, which states that the transmission rate from the initial state $|\mathrm{i}\rangle$ to a final state $|\mathrm{f}\rangle$ is given by

$$R_{\mathrm{i}\to\mathrm{f}} = \frac{2\pi}{\hbar} \mid M_{\mathrm{fi}} \mid^2 \delta(E_{\mathrm{i}} - E_{\mathrm{f}}) \tag{2.13}$$

Where M_{fi} is the matrix element of the perturbation potential between the initial and final state and δ is the Dirac distribution that ensures energy conservation. Naturally an electron can only tunnel from occupied into unoccupied states. At zero Kelvin, there is a sharp Fermi edge separating occupied and unoccupied states while at elevated temperatures the Fermi edge is smeared out. We can express the tunneling current as:

$$I = \frac{2\pi e}{\hbar} \int \mid M_{\mathrm{ts}} \mid^2 N_t(E - eV) N_s(E)[1 - f(E - eV)] f(E) \mathrm{d}E \tag{2.14}$$

Where $f(E)$ is the Fermi-Dirac distribution and $N(E)$ the density of states. The occupied tip states ($N_{\mathrm{t}} f_{\mathrm{t}}$) can tunnel into unoccupied sample states ($N_{\mathrm{s}}[1 - f_{\mathrm{s}}]$). The common energy scale is chosen to be that of the sample, so that the tip energy scale is shifted by $\Delta E = eV$. At absolute zero temperature, the Fermi-Dirac distribution is a step function, and one can express the total current as:

$$I(T = 0) = \int_{E_{\mathrm{F}}}^{E_{\mathrm{F}}+eV} \mid M_{\mathrm{ts}} \mid^2 N_{\mathrm{t}}(E - eV) N_{\mathrm{s}}(E) \mathrm{d}E \tag{2.15}$$

where E_{F} is the Fermi level. The STM has the ability to access both occupied and unoccupied states of the substrate by changing the sign of the bias voltage.

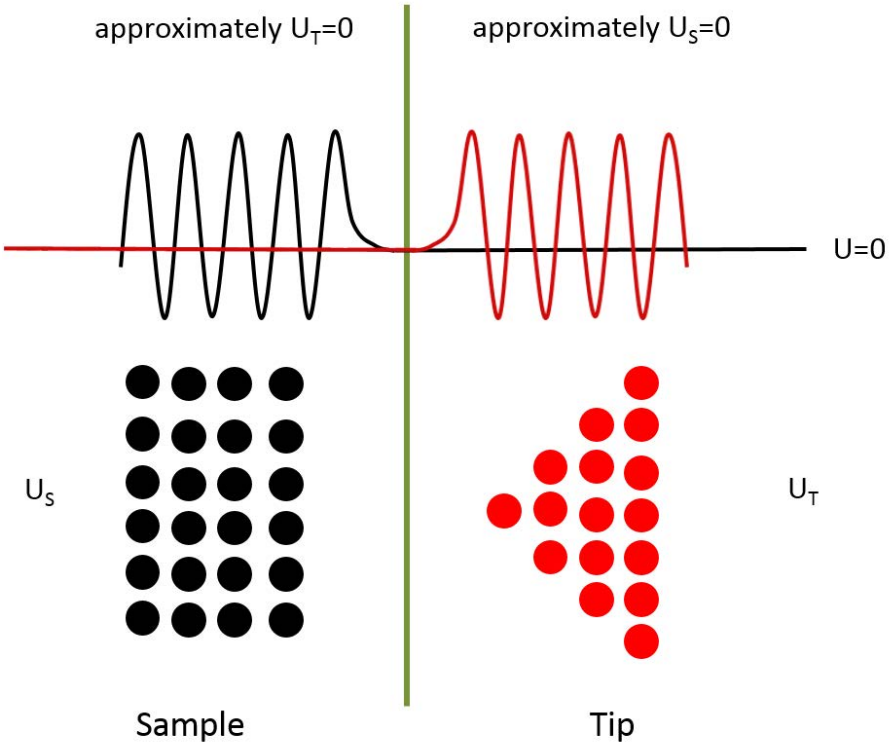

Fig. 2.8: Diagram representing the Bardeen approach: tip and sample region separated by a separation surface. The tip potential is zero in the sample region and *vice versa*.

The Bardeen approach

Bardeen's approach [144] for evaluating the matrix element M_{ts} considers the overlap of the tip-sample wave functions and applies time dependent perturbation theory to the problem.

Fig. 2.8 explains the principle of the approximation made in the Bardeen approach. We see two independent regions, the tip and sample region, separated by a separation surface. The wave functions exponentially decay in the barrier so that the tip potential in the sample region is zero and *vice versa*. Due to the separation of the two regions we can write two independent Schrödinger equations:

$$(K + U_{\mathrm{s}})\Psi_{\mathrm{s}} = E_{\mathrm{s}}\Psi_{\mathrm{s}} \tag{2.16}$$

$$(K + U_{\mathrm{t}})\Psi_{\mathrm{t}} = E_{\mathrm{t}}\Psi_{\mathrm{t}} \tag{2.17}$$

Here K is the operator of the kinetic energy of a single electron and U_s and U_t are the potentials of the sample and the tip respectively. The wave function Ψ can be expanded in any of the basic sets Ψ_S or Ψ_T, as $\Psi = \sum_\mathrm{t} a_\mathrm{t}\Psi_\mathrm{t}$. Now we can apply the time-dependent perturbation theory and take the electron at the initial time $\tau = 0$ to be in the sample state. The correspondent wave function at the time τ is then:

$$\Psi(\tau) = \Psi_\mathrm{S}\,\mathrm{e}^{-\mathrm{i}\omega_\mathrm{s}\tau} + \sum_\mathrm{t} a_\mathrm{t}(\tau)\Psi_\mathrm{t}\,\mathrm{e}^{-\mathrm{i}\omega_\mathrm{t}\tau} \tag{2.18}$$

where $a_\mathrm{t}(0) = 0$ and $E = \hbar\omega$. We can now insert Ψ in a time dependent Schrödinger equation and calculate the effective matrix element M_ts to be:

$$M_\mathrm{ts} = \langle\Psi_\mathrm{t} \mid U_\mathrm{t} \mid \Psi_\mathrm{s}\rangle = \int \Psi_\mathrm{t}^* U_\mathrm{t}\Psi_\mathrm{s}\mathrm{d}\vec{r} \tag{2.19}$$

Since according to the Bardeen approximation $U_\mathrm{t} = 0$ outside of the tip region, the integration needs to be done only in the tip region volume, where $U_\mathrm{s} = 0$ would be zero according to the approximation. After integrating partially the volume integral and rewriting it as a surface integral we obtain:

$$M_\mathrm{ts} = \frac{\hbar^2}{2m}\int_\mathrm{S}(\Psi_\mathrm{s}\nabla\Psi_\mathrm{t}^* - \Psi_\mathrm{t}^*\nabla\Psi_\mathrm{s})\mathrm{d}S \tag{2.20}$$

where S is the separating surface between the tip and the sample.

Tersoff and Hamann's model

Since the exact atomic structure of an STM tip and also the chemical nature of the tip apex is unknown, we need to make an assumption regarding the tip, in order to calculate the Bardeen's matrix element M_ts. Such an assumption has been done by Tersoff and Hamann [145]. In their model, they replaced the unknown structure of the tip by a simplified system, in which the wave function of the atom at the very end of the tip has an atomic s-wave-function. Since the tunneling current depends on the overlap of the tip and sample wave functions and since these functions decay exponentially into the vacuum, only the orbitals localized at the outermost tip atom will be of importance for the tunneling process. Assuming low (or zero) temperature and low bias voltage, the total tunneling current flowing from tip to sample can be expressed as:

$$I = \frac{2\pi e}{\hbar}V\sum_\mathrm{s} \mid M_\mathrm{ts} \mid^2 N_\mathrm{t}(E_\mathrm{F})\delta(E_\mathrm{s} - E_\mathrm{F}) \tag{2.21}$$

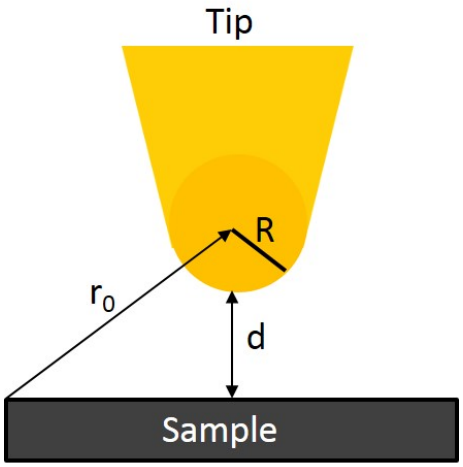

Fig. 2.9: Diagram representing the Tersoff and Hamann's model: tip modeled as a local spherical potential with curvature R and the center r_0

The surface wave function can now be written as a 2D Bloch expansion with K as the 2D reciprocal lattice vector and be inserted into the Schrödinger equation resulting in:

$$\Psi_{\mathrm{s}}(\vec{r}) = \sum_{K} a_K(0)\, \mathrm{e}^{-\sqrt{\kappa^2+(k_{\mathrm{II}}+K)^2}}\, \mathrm{e}^{\mathrm{i}(k_{\mathrm{II}}+K)\vec{r_{\mathrm{II}}}} \tag{2.22}$$

where $\kappa^2 = \frac{2m(V-E)}{\hbar^2}$. If $E = E_{\mathrm{F}}$ then $\kappa^2 = \frac{2m\phi}{\hbar^2}$ with ϕ being the work function of the surface.

The main idea of the Tersoff and Hamann's model is in the choice of the wave function of the tip. The Fig. 2.9 shows the tip modeled as locally spherical potential with the position of the center r_0 and the curvature R. The tip wave function is chosen to have the form of an s-wave:

$$\Psi_{\mathrm{t}}(\vec{r}) = \frac{1}{\sqrt{N}} \kappa R\, \mathrm{e}^{\kappa R}\, \frac{\mathrm{e}^{-\kappa|\vec{r}-\vec{r_0}|}}{\kappa \mid \vec{r}-\vec{r_0} \mid} \tag{2.23}$$

Now we consider the separation surface S to be parallel with the surface and write the tip wave function as a 2D Fourier sum. We find that the matrix element is proportional to the sample wave function evaluated at the tip center of curvature:

$$M_{\mathrm{ts}} \propto \Psi_{\mathrm{s}}(\vec{r_0}) \tag{2.24}$$

The total current flowing from the tip to the sample is then proportional to:

$$I \propto V N_{\mathrm{t}}(E_{\mathrm{F}}) \sum_{\mathrm{s}} \mid \Psi_{\mathrm{s}}(\vec{r}_0) \mid^2 \delta(E_{\mathrm{s}} - E_{\mathrm{F}}) \tag{2.25}$$

The sum in the expression 2.25 is the local density of states (LDOS) at the Fermi level evaluated at the tip center. STM images the LDOS of the sample and thus we can use this equation for interpretation of STM images. In the expression we find once again the exponential relationship $I \propto \mathrm{e}^{-2\kappa d}$. It shows how the tunneling probability and therefore also the tunneling current, depend exponentially on the size of the gap, d, so that 1 Å change in the tip-sample distance, results in an order of magnitude change in the tunneling current. As a consequence, STM has an exceptional spatial resolution. The lateral resolution of STM can be in first approximation expressed as:

$$L_{\mathrm{eff}} \approx 2\sqrt{\frac{R+d}{\kappa}} \tag{2.26}$$

The expression implies that a lateral resolution much smaller than the radius of the tip's apex, R, is possible, if the distance between the surface and tip, d, is much smaller than the tip's radius. Tersoff and Hamann used this expression to simulate the first experiments by Binnig on Au(110). The images showed atomic rows with lateral periodicity of 8 Å and a height corrugation of 0.45 Å. To reproduce the results, Tersoff and Hamann had to assume a tip radius of 9 Å, a tip-sample distance of 6 Å and a value for κ of 1.2 $\mathrm{Å}^{-1}$. For smaller atomic-scale surface structures the validity of the expression for the lateral resolution breaks down. Nowadays, achievements of STM exceed this expected resolution, and the lateral resolution can reach less than 1 Å. In 1990, Chen proposed to use another tip model, instead of the s-wave orbital [146]. For most widely used tip materials the DOS at the Fermi level is dominated by d-states. A d-state pointing towards the sample will make tip "sharper" and extend further into vacuum than the s orbital, thus achieving a better resolution.

2.2.3 Auger electron spectroscopy

The Auger electron spectroscopy (AES) is a surface sensitive analysis technique, whose name comes from the phenomenon, the Auger effect, firstly observed by Meitner in 1922 [147] and Auger in 1923 [148]. Auger gave the first theoretical interpretation of the effect in 1925 [149]. Electron-excited Auger electrons were used to study surface impurities for the first time in 1953 by Lander and in 1968 Harris demonstrated

usefulness of the technique when he differentiated the energy distribution of Auger electrons emitted from a bombarded surface [150]. Meanwhile Weber and Peria started employing LEED optics as Auger spectrometers [151]. In 1969 Palmberg *et al.* invented the cylindrical mirror analyzer (CMA) which greatly improved the speed and sensitivity of the technique [152]. Since the mid 80's Schottky field emitters have been implemented as electron sources, allowing analysis of features of less than 20 nm in size, creating a new microscopy technique. Today AES is routinely used for analysis of metals for its advantage of being a non-destructive, surface sensitive method, capable of giving chemical information and also quantitative information about the sample surface.

An example of the experimental setup of AES with a CMA as it looks today is shown in Fig. 2.10. A cylindrical mirror analyzer has also been used in the present work. It consists of two cylinders with entrance and exit apertures cut in the inner cylinder and a deflection potential applied between the two cylinders. The electron gun produces an electron beam which is focused on the sample. The emitted Auger electrons are deflected around the electron gun through an aperture towards the electron multiplier. Scanning the deflection potential and recording the signal as a function of electron energy provide distribution in energy of electrons leaving the sample surface. To improve the signal to noise ratio, a lock-in amplifier is used, which produces derivative spectra. An example of raw and derivative AES spectra is shown in Fig. 2.11. An oscillator superimposes a sinusoidal modulation on the potential applied to the outer cylinder of the analyzer. A lock-in amplifier takes the signal, multiplies it with a reference signal (provided by the internal oscillator) and integrates it over a specified time. In the resulting signal, any contributions to the signal having a different frequency than the reference, are attenuated to zero.

Auger emission

The main principle of the technique is the analysis of Auger electrons. The energy level diagram for an Auger transition is portrayed in Fig. 2.12. If an atom is ionized in an inner level it can relax to a lower energy by a process in which an electron from a higher level fills the vacancy. To compensate the energy difference two processes compete: photon emission and emission of an electron. If an electron is emitted, this electron is then called an Auger electron. Its emission is a radiationless transition in an ionized atom after which the atom is doubly ionized. In the example in Fig. 2.12 a primary electron beam removes an electron from the K shell of an atom, an electron from the level L_1 fills in the vacancy and the energy difference from this

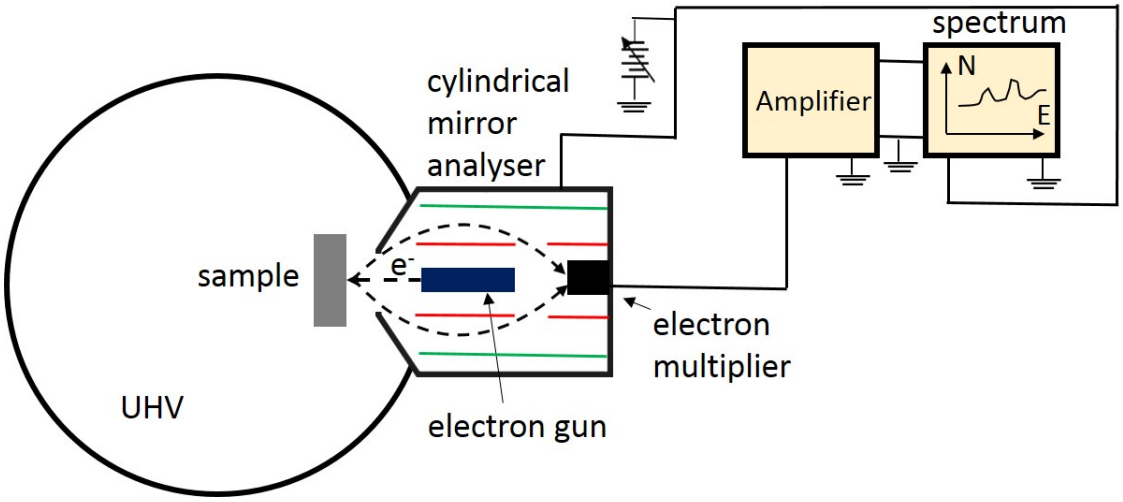

Fig. 2.10: Diagram representing the experimental setup of AES. The inner cylinder of CMA is portrayed as a red line, the outer cylinder as a green line.

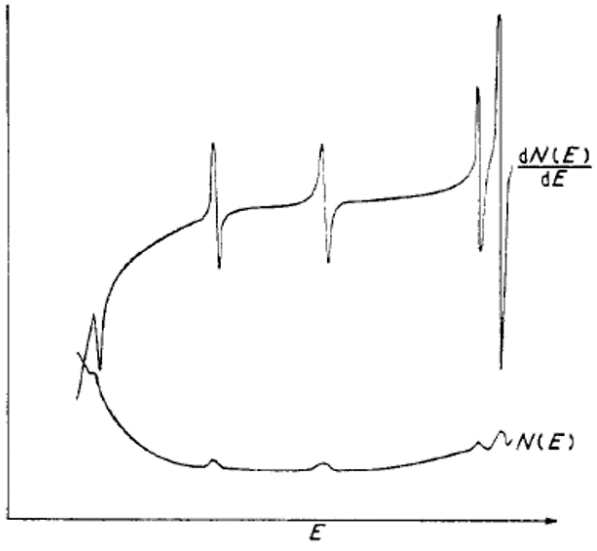

Fig. 2.11: Example of AES spectrum: $N(E)$ - raw spectrum, $\frac{\mathrm{d}N(E)}{\mathrm{d}E}$ - derivative spectrum. From Ref. 153.

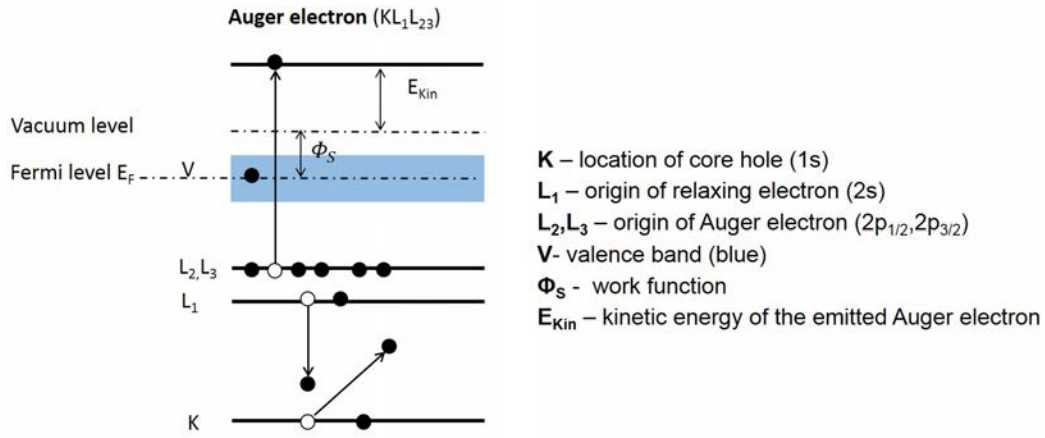

Fig. 2.12: Schematic energy level diagram for the Auger process

process is compensated by an ejection of an Auger electron from the $L_{2,3}$ level. The notation for this Auger electron will be $KL_1L_{2,3}$, according to all shells participating in the process. The kinetic energy of the Auger electron is characteristic of the energy levels of the ejecting atom and is independent of the energy of the ionization source. The kinetic energy of the $KL_1L_{2,3}$ Auger electron will correspond to:

$$E_{\mathrm{kin}}(\mathrm{KL_1L_{2,3}}) = E_{\mathrm{K}} - E_{\mathrm{L_1}} - E_{\mathrm{L_{2,3}}} - E_{\mathrm{inter}}(\mathrm{L_1L_{2,3}}) + E_{\mathrm{R}} - \phi_{\mathrm{S}} \tag{2.27}$$

where $E_{\mathrm{inter}}(\mathrm{L_1L_{2,3}})$ is the interaction energy between the holes in the L_1 and $L_{2,3}$ shell, E_{R} is the sum of the intra-atomic and the extra-atomic relaxation energies and ϕ_{S} is the work function. Since the kinetic energies of the Auger electrons are characteristic for energy levels of individual atoms, by detecting the electrons and determining their energy in an analyzer, the chemical species of the emitting atom can be found.

The ionization of atoms can be induced by any mechanism. Typically used in AES are electron beams with the energy of primary electrons in the range from 1 to 5 keV. The disadvantage in employing an electron beam as the ionization source is that the Auger electrons have to be separated from the background of secondary electrons in the spectra. Fig. 2.13 shows the excitation volume in the sample during interaction with an electron beam, which illustrates the surface sensitivity of AES. The Auger electrons come from the depth of only about 0.4 to 5 nanometers. This is because electrons coming from deeper levels will lose their energy due to inelastic collisions. The average distance traveled before such a collision is known as the

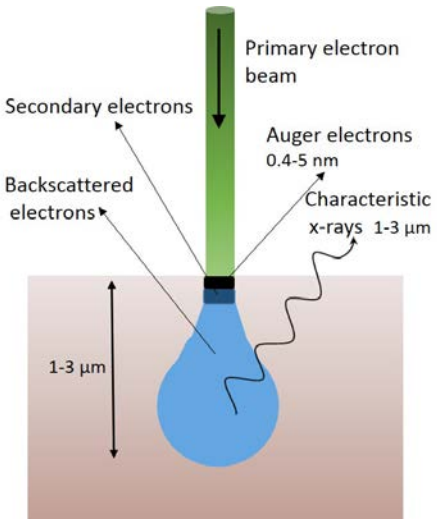

Fig. 2.13: Schematic image of the excitation volume in the sample interacting with an electron beam

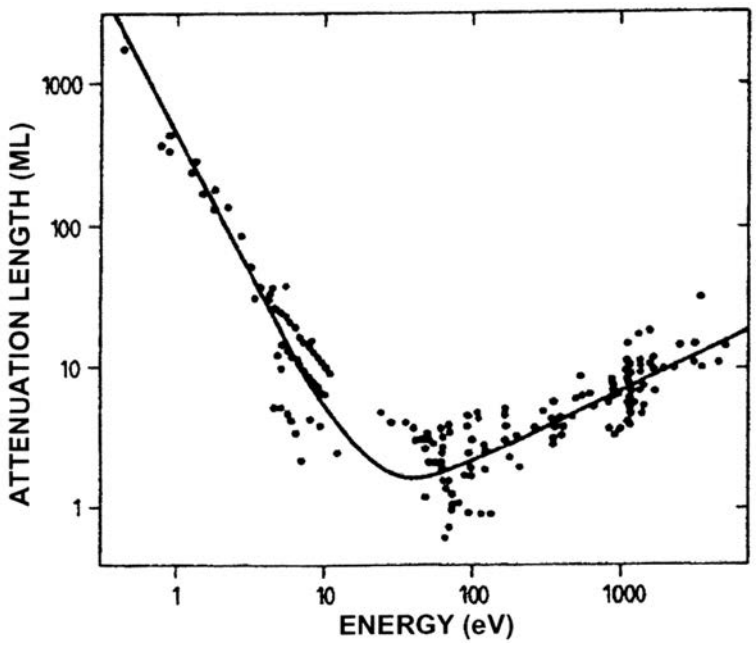

Fig. 2.14: Universal curve. Compilation of measurements of inelastic mean free path as a function of electron kinetic energy made by Seah and Dench [154]. The solid line is a least-squares fit.

inelastic mean free path (IMFP). The Fig. 2.14 shows a compilation of measurements of the IMFP made by Seah and Dench [154], in terms of atomic monolayers. This curve is known also as the universal curve. In AES, the energy range of the escaped electrons is typically 20 to 1000 eV. From the universal curve we can estimate that these electrons come from the depth of about two to six monolayers.

2.3 Sample preparation

The sample studied throughout this thesis, a copper single crystal with the (110) orientation, was purchased from the *Surface Preparation Laboratory* [155]. The sample has the form of a disk with a diameter of 10 mm and the thickness of 2 mm. A photographic image of the sample on a sample holder is shown in Fig. 2.15. The delivered surface has been polished by the manufacturer and its misorientation was estimated by STM to be 0.2°. Before the first introduction of the new sample into the UHV chamber it has been annealed at 1000 K in hydrogen (99.999%) for four hours in our laboratory. This procedure mainly served to remove sulfur from the sample, as this contamination segregates from the bulk during annealing and reacts with hydrogen once at the surface. Since the first introduction of the sample, the surface has been re-polished electrochemically. Once the sample has been introduced into vacuum a typical cleaning procedure consisting of cycles of ionic bombardment, also called sputtering, and annealing has been employed to prepare the surface before each individual experiment. The principle of sputtering consists in bombarding the surface with accelerated noble gas ions, whose impact will remove the uppermost atomic layer of the sample. In the sputter gun, electrons are emitted from a filament and accelerated into a cylindrical grid cage by a positive potential. Electron impact on the inert gas atoms within the grid cage produce ions that are accelerated towards a lens by the extractor, then out of the gun in the direction of the sample that has been placed in front the gun under a certain angle. We have used argon at the pressure of 10^{-5} mbar for the sputtering. The parameters of the sputter gun that we have used were 1.5 kV and 30 mA (sample current $I_S \approx 3.5$ μA) for removing of step bunching after experiments and once the sample has shown good enough structural quality, few cycles of 600 V and 20 mA ($I_S \approx 2$ μA) were employed to fine clean the surface. Higher voltage removes more atomic layers, but can create defects in the surface, which is why it is important to finish with low voltage sputtering. Each sputtering has been done for 30 minutes.

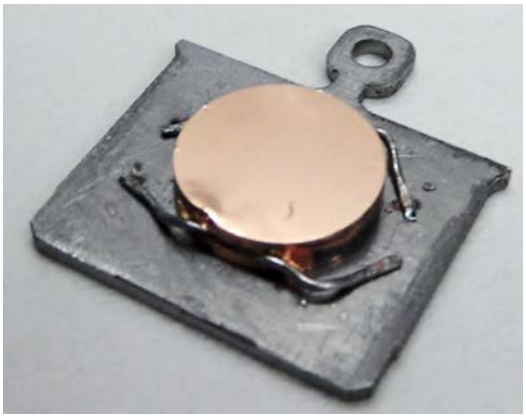

Fig. 2.15: Photographic image of the sample on a sample holder.

After the sputtering the surface is atomically rough and rather unsuitable for STM measurements. In order to obtain a flat surface the sample has to be annealed at a temperature around 2/3 of its melting point. We have found that annealing to 870 K is sufficient to reorganize the surface, but not to induce too much segregation of contaminations from the bulk. The annealing has been done by heating a tungsten filament protected by a ceramic cover which has been placed under the sample holder. A calibration had to be performed beforehand to determine the voltage settings for the regulated power supply. The process of cleaning a sample is controlled by AES. In Fig. 2.16, AES spectra show the evolution of contaminations on the surface during cleaning. After the sample is introduced into UHV, it is contaminated typically by C, O, Cl and S. After one annealing for 30 minutes, the amount of contaminations decreases, but to achieve a surface with no contaminations in the spectrum, several annealing and bombarding cycles have to be repeated. As will be discussed in section 2.5, STM requires extremely clean surfaces and therefore the annealing and bombarding has to be continued even after AES shows no more contaminations.

After performing hundreds of series of experiments involving annealing of the surface with adsorbed oxygen and sulfur, the surface has been found to be covered mainly by very small terraces, due to step bunching, and not suitable for further experiments. The step bunching effect is especially bothering, since we have found that its presence significantly influences the periodicity of the nanostructure on surrounding flat terraces and thus had to be removed. For this purpose the sample has been taken out of the UHV chamber and electropolished. The electropolishing has been done in H_3PO_4 (60 vol%) with a voltage of 1.4 V for 10 minutes, using copper as a counter electrode. The setup for electropolishing is illustrated in Fig. 2.17. Before electropolishing, the surface needs to be cleaned from impurities with

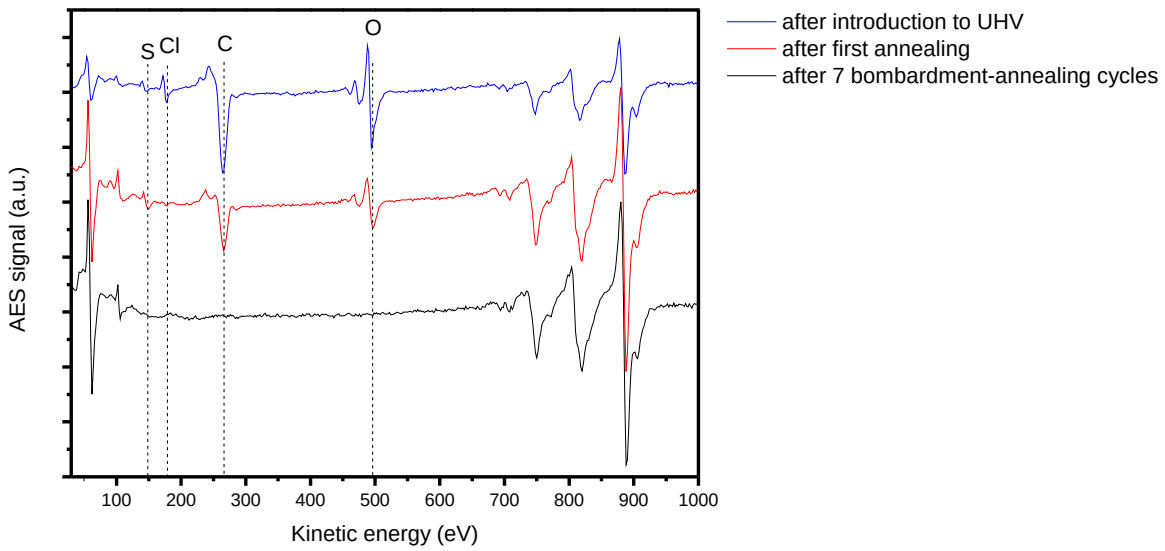

Fig. 2.16: AES spectrum of contaminated and clean sample. The peaks which are not assigned are Cu-peaks.

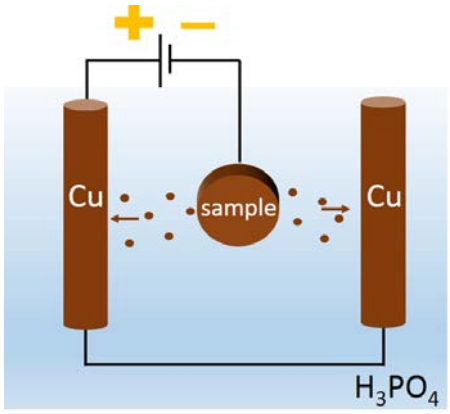

Fig. 2.17: Principle of electropolishing: the copper disk sample is immersed in an electrolyte and connected to a circuit as the anode.

acetone, ethanol and purified water. Next, the metallic sample is immersed into a bath of electrolyte and serves as an anode. A current passes from the anode, where metal is oxidized and dissolved in the electrolyte. In this manner thin layers of the sample are removed and the rough surface is being polished. The reduction reaction at the cathode produces hydrogen, which we can observe as bubbles going up in the electrolyte. After the electropolishing time has passed the surface is quickly rinsed by 10% H_3PO_4 and in the end by at least 1 liter of purified water to remove all electrolyte. Finally the sample is dried in N_2 flow.

2.4 Tip preparation

The tip is perhaps the most crucial element in obtaining atomic resolution in STM. Ideally a tip would have a single atom at its apex. More atoms present at the end of tip result in the tunneling current passing through more than one atom and consequently a fuzzy image. The preparation of such atomically sharp tip depends on the material used. For example Pt/Ir tips are generally prepared by cutting the wire with a wire cutter under a certain angle. In present thesis a W wire of the diameter 0.25 mm has been used to prepare the STM tip. For tips used in UHV, the cutting technique is not recommended, as it gives unreproducible tips. The preparation method of choice is therefore electrochemical etching. After cutting about 1.5 cm long piece of the wire, rinsing it with purified water and drying, we connect it to a circuit with a platinum electrode and a direct current source. We use 3 M NaOH as the electrolyte.

As shown in Fig. 2.18, we immerse the very end of the tip inside the solution and set the source to 10 V potential difference. The setup for this part of the preparation is shown in Fig. 2.20a. The following electrochemical reaction can be observed as bubbles going up in the solution [156].

$$W(s) + 2OH^- + 2H_2O \rightarrow WO_4^{2-} + 3H_2(g)$$

The corresponding half-reactions on the anode and cathode respectively are:

$$\text{Anode} : W(s) + 8OH^- \rightarrow WO_4^{2-} + 4H_2O + 6e^-$$

$$\text{Cathode} : 6H_2O + 6e^- \rightarrow 3H_2(g) + 6OH^-$$

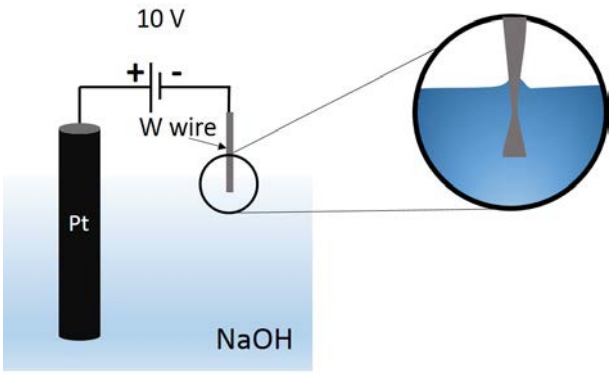

Fig. 2.18: Electrochemical etching: 1st stage. The tip is positioned vertically and immersed in the electrolyte. The electrochemical reaction attacks the immersed part of the wire.

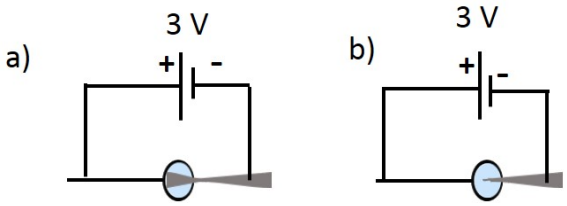

Fig. 2.19: Electrochemical etching: 2nd stage. The tip is positioned inside a ring with the electrolyte. a) The tungsten wire is placed inside a NaOH bubble and a closed electric circuit. b) The thinned part of the wire is cut-off by the electrochemical reaction and thus a very sharp tip is created.

The tungsten wire is getting thinner as the reaction proceeds. When the wire is thin enough, it is removed from the solution and a new setup is used to finish cutting of the tip (as illustrated in Fig. 2.20b). In this setup, the tip is not immersed in the solution, but merely placed inside a droplet of NaOH, which is formed inside a ring of Pt wire. The circuit is closed and this time 3 V potential is set. The tip is placed so that the thinned part is exactly in the middle of the droplet and cut off by the electrochemical reaction, forming a very sharp tip. The principle of this preparation step is illustrated in Fig. 2.19. Before introducing the tip into UHV, it needs to be rinsed in ethanol and purified water.

Once the tip is introduced to the UHV chamber, we do not have much control over the tip's shape. If the STM tip does not work, we can sputter the tip in the UHV chamber and try to completely change its structure. However sputtering can round off a sharp tip and should therefore be considered as a last option. Other

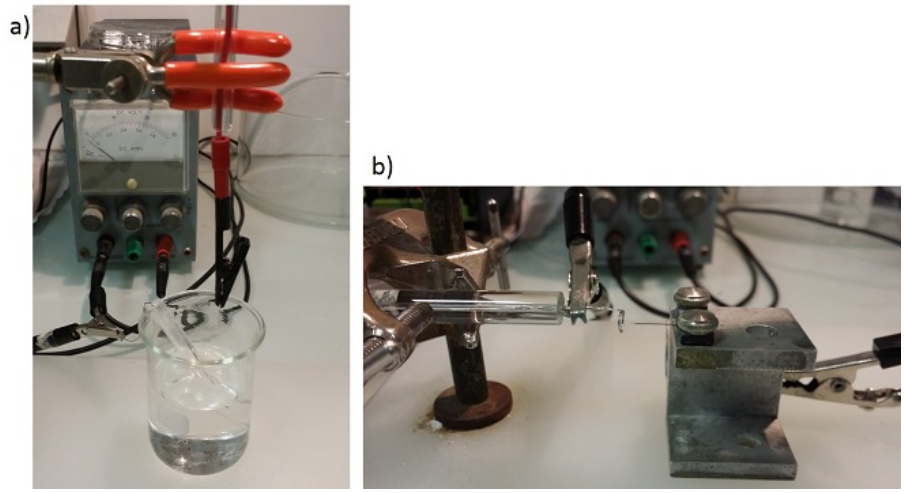

Fig. 2.20: Photographic images of the setup for tip preparation. a) Setup for the thinning of the as-cut W wire. b) Setup for cutting off of the thinned W wire to create the final tip form.

milder techniques to improve the STM tip would include pulses of high voltage or fast scanning over step edges, which could help to remove contaminations from the tip. We can also bring the tip close to the surface by choosing a high tunneling current and low voltage and perform spectroscopy. The strong electric field will lead to field emission of electrons at the very end of the tip, where the electric field pro surface is the highest and this can lead to the growth of a sharp microtip at the apex of the STM tip.

2.5 STM in praxis

The theory of STM has been already discussed in the previous section 2.2.2, however in praxis, much more information and experience is needed to be able to really use this technique. With STM we are able to obtain atomic resolution under ideal conditions, but to obtain such conditions is rather difficult. First of all, for a successful experiment we need a surface free of contaminations and ideally with few crystallographic defects. Even if we do not detect any contaminations in AES, the surface is not necessarily clean enough for STM. Examples of dislocations in a copper single crystal and a contaminated copper surface are shown in Fig. 2.21a) and b) respectively. Scanning on a contaminated surface can cause the STM tip to crash into the surface, after which resolution can be lost completely. In order to obtain a surface suitable for STM imaging, a careful preparation by sputtering and

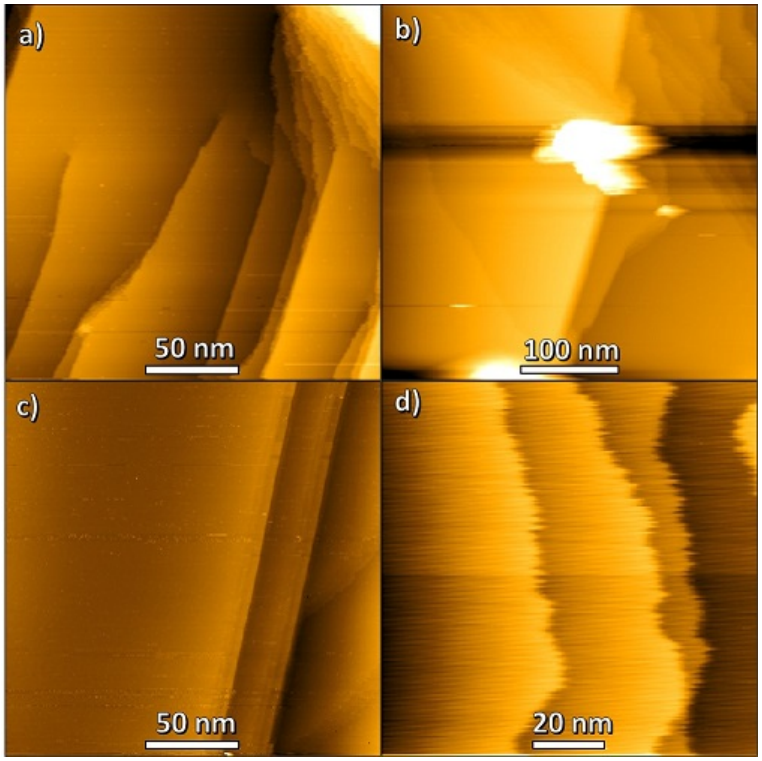

Fig. 2.21: STM images of copper: a) screw dislocations ; b) contamination; c) clean copper surface; d) "fuzzy" step edges of clean copper. Tunneling parameters: a) $I = 0.2$ nA, $V = 1.5$ V; b) $I = 0.5$ nA, $V = -1.5$ V; c) $I = 0.2$ nA, $V = -1.5$ V; d) $I = 0.2$ nA, $V = -0.7$ V.

annealing cycles, as described in section 2.3, is necessary. Fig. 2.21c) and d) show examples of STM images of a clean copper surface. No contaminations are visible and the terraces are aligned along the [001] direction. Fig. 2.21d) additionally shows a "fuzzy" appearance of a step, which is typically observed by STM on clean copper [71]. This effect is caused by the mobility of copper adatoms, which are typically present at the step edges. The tip interacts with the mobile atoms causing them to move back and forth during scanning.

Once we have obtained a clean surface, it is necessary to have a good tip for STM imaging. The tip preparation is described in section 2.4. Fig. 2.22 shows examples of STM images recorded with a defective tip. In Fig. 2.22a) the tip itself is being imaged on the surface. This case can be distinguished from a contaminated surface by identifying the exactly same shape of the artifact repeated on the surface. In Fig. 2.22b) a strong unwanted interaction between the tip and the surface is causing a change to the terraces. The orbitals of the tip and the atoms on the surface overlap, starting to form a chemical bond and thus atoms are being moved by the tip during

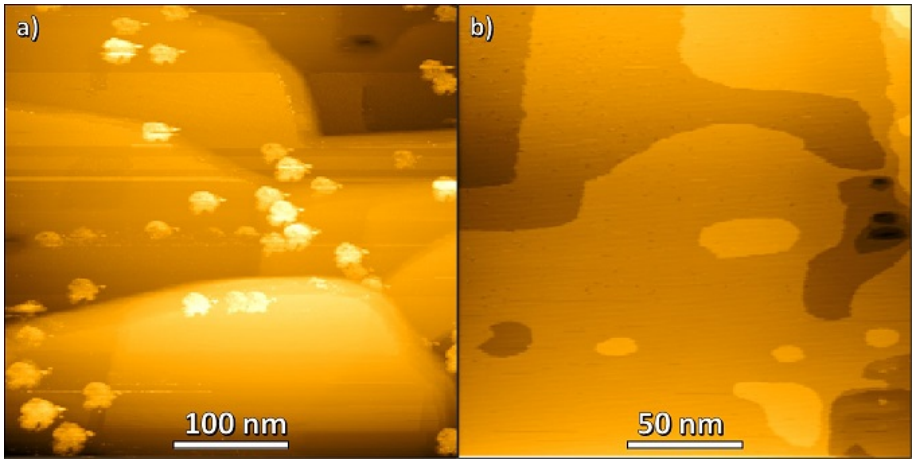

Fig. 2.22: Artifacts of STM: a) STM tip is being imaged on the surface ; b) strong interaction between STM tip and the surface. Tunneling parameters for a) and b): $I = 0.2$ nA, $V = -1.5$ V.

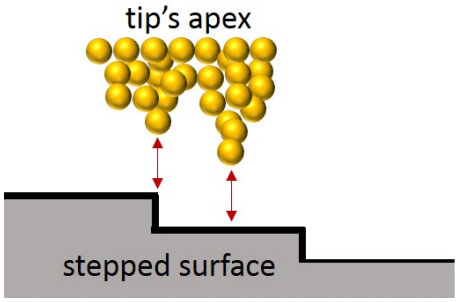

Fig. 2.23: Schematic representation of a multiple STM tip. The red arrows show the places where tunneling current will pass between the surface and the tip.

the scanning. We identify this problem when scanning several times at one place causes a change of the surface. Another typical problem present when doing STM experiments is a so-called "multiple tip". In this case, the surface is not being imaged only by the apex of the tip, but also by other sharp extensions present at the end of the tip, as portrayed in Fig. 2.23. If imaging with such a tip, we will see the same area of the surface more times on different places of the STM image.

In the present thesis all STM images were obtained in the constant current mode. The recorded STM images are subsequently treated by a suitable software. In the present thesis the software Gwyddion [157] and WSxM [158] were used, mainly to correct the drift, subtract background (offset, line or parabola) and increase the contrast by choosing how the data values are mapped to colors.

2.6 Experimental conditions

2.6.1 Preparation of the Cu(110)-(2×1)O nanostructure: Classical and S co-adsorption method

The nanostructured surface has been prepared by exposing a clean Cu(110) to oxygen in the pressure range $1 \times 10^{-8} - 1 \times 10^{-6}$ mbar for several minutes at room temperature. The amount of adsorbed oxygen has been measured by AES. The surface was then annealed for 30 minutes. Two different temperatures have been used throughout the present study, 670 K and 720 K. After annealing, the sample has been cooled down to room temperature before beginning STM measurements. For preparing nanostructures with the new method, the surface has been exposed to both oxygen and H_2S (in any desired order) before the annealing. Typical exposure for H_2S were in the range of $1 \times 10^{-8} - 1 \times 10^{-9}$ mbar for one minute. We have found that exposition to H_2S partially removes the pre-adsorbed oxygen, therefore the adsorbed amounts of both species have to be verified by AES and, if needed, an additional oxidation can be added.

2.6.2 Sulfidation of the Cu(110)-(2×1)O nanostructure

2.6.2.1 Kinetics by AES

The measurement of the kinetics presented in section 4.2, has been performed by stepwise exposure of the surfaces to H_2S at room temperature, while the sample was in the preparation chamber. Exposures of 1×10^{-8} mbar or 3×10^{-9} mbar for 30 seconds have been chosen. After each exposure step, we have pumped the chamber and recorded an AES spectrum. Exposures have been continued until the signal of sulfur in the differentiated AES spectrum saturated.

2.6.2.2 Mechanism by STM

The sulfidation experiments presented in sections 4.3 and 4.4, have been performed by exposing a nanostructured surface to H_2S, while scanning by STM. Since the pressure gauge and the leak valve are both situated in the preparation chamber, the pressure in the STM part is lower than the one we measure. It has been estimated that during exposure, the difference between the local pressure at the sample position and the position where the pressure is measured, is around two orders of magnitude. For the sulfidation experiments, the sample has been exposed typically to pressures

in the range $1 \times 10^{-8} - 1 \times 10^{-7}$ mbar for several minutes. All experiments have been performed at room temperature.

Chapter 3

Tuning the Cu(110)-(2×1)O nanostructure

In the present chapter, a technique for tuning the Cu(110)-(2×1)O nanostructure by co-adsorbing low amounts of sulfur is presented. This new approach has been implemented to prepare numerous nanostructures with increased periodicity with respect to the classical model, which were then studied by STM. The fabrication method has been successfully tested for sulfur coverages between 0.025 and 0.15. The highest periodicity we have been able to prepare was 200 ± 20 nm. Finally, a model has been developed by modifying the existing Marchenko-Vanderbilt model to describe the influence of the presence of sulfur.

3.1 STM of the Cu(110)-(2×1)O surface

During this study, numerous STM images of the nanostructured Cu(110)-(2×1)O surface have been obtained. STM has the capability to probe the geometric and electronic structure of a surface with real space atomic resolution, however the discrimination between chemically different atoms is less direct than desirable. Therefore the distinction between oxygen and copper in STM images of the Cu(110)-(2×1)O nanostructure has to be carefully considered. Oxidized and clean copper stripes obviously differ in height. Yet STM is not a simple topographic tool and is influenced also by the electronic state of the surface, and of the STM tip itself. It is known that by changing the chemical identity of the apex of the tunneling tip, we can inverse the contrast for the O and Cu atoms in the STM image [82, 159, 160]. As schematically explained by Fig. 3.1, with a clean W-tip only the oxygen atoms

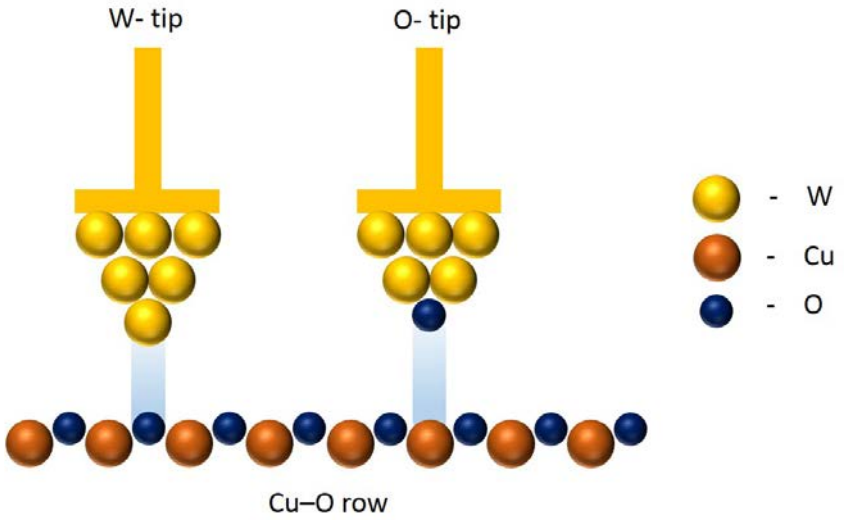

Fig. 3.1: Schematic representation of contrast inversion in STM

of the Cu–O chains are visualized with atomic resolution. They appear with dark contrast and their height seems lower than the substrate. When an oxygen atom is caught at the end of the tip, the Cu atoms of the Cu–O chains are imaged by STM and they appear higher than the substrate. Since we cannot image both Cu and O atoms of the Cu(110)-(2×1)O phase at the same time, the entire oxidized stripe will appear darker, when scanned with a clean tungsten tip and it will appear brighter, when scanned with a tip ended by an oxygen atom. So the contrast of the image changes with the tip conditions, an example of which is shown in Fig. 3.2. In order to correctly assign each stripe to either oxidized or clean metal stripe, we need to zoom in the area of the stripes and obtain atomic resolution. The (2×1)O phase has a double periodicity with respect to the (1×1) structure of clean Cu and therefore it is much easier to see the oxygen rows, than the Cu rows.

The chemical identity of the STM tip can easily change during the scanning. For example in Fig. 3.2a) the STM tip ended by an oxygen atom at the beginning of the scanning, but the O atom has been removed and then caught back on during the scanning. This is why the contrast inverses back and forth in the image. As we scan from bottom of the image to the top, we first see CuO stripes as protrusions. Then, in the zone 1 of the image, the tip has been cleaned from the oxygen atom and we see the CuO stripes as depressions. The STM image in Fig. 3.2b) has been recorded with an O-tip and c) with a W-tip.

Furthermore, in the STM profiles in Fig. 3.2, we can see that the height difference between clean copper stripes and oxidized copper stripes is not always the same, but

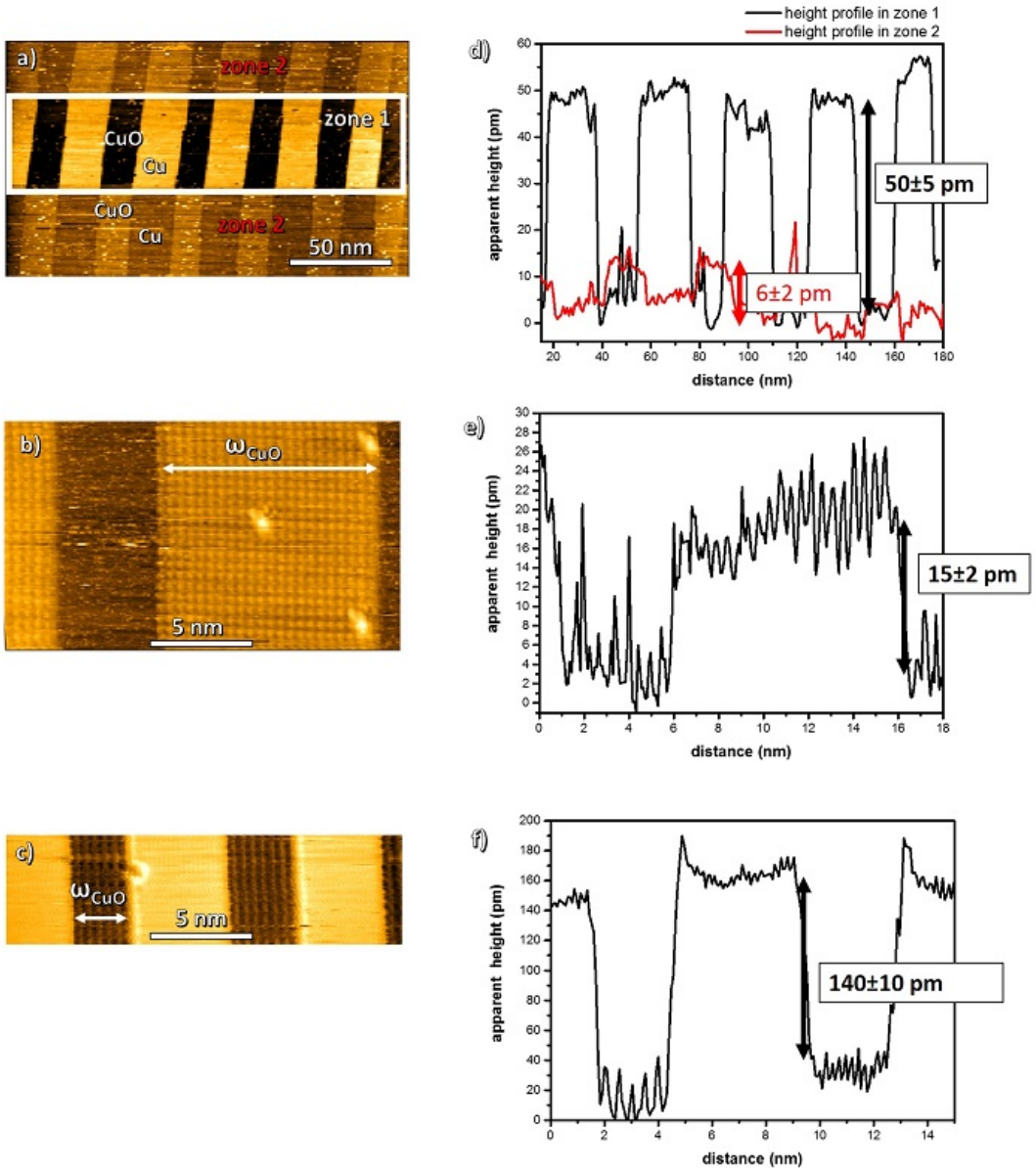

Fig. 3.2: STM images with inversion of contrast and corresponding profiles. a) STM image with a contrast inversion during the measurement caused by adsorption of an oxygen atom at the apex of the tip. The image is divided into two zones. Zone 1 was scanned with a W-tip (protrusions are Cu stripes), zone 2 with an O-tip (protrusions are CuO stripes). d) STM profiles in zone 1 and 2 of the image a). b) STM image obtained by an O-tip. e) STM profile from image b). c) STM image obtained by an W-tip. f) STM profile from image c). Tunneling parameters: a) $I = 0.2$ nA, $V = 0.7$ V; b) $I = 2.0$ nA, $V = 1.0$ V; c) $I = 0.1$ nA, $V = 1.0$ V. All the profiles have been shifted so that the lowest point is at height = 0 pm and taken in the direction across the stripes.

Table 3.1: Summary of height differences between Cu and CuO in STM images for different types of STM tips and different tunneling conditions. For better overview, identical tunneling conditions are highlighted by the same color.

Δheight$_{\text{Cu–CuO}}$ (pm)	I (nA)	V (V)	W-tip	O-tip
140 ± 10	0.1	1.0	×	
100 ± 10	0.2	−1.5	×	
83 ± 5	0.2	0.7	×	
77 ± 5	0.2	−0.7	×	
50 ± 5	0.2	0.7	×	
45 ± 5	0.8	1.5	×	
−23± 2	0.2	−0.7		×
22 ± 2	0.2	−1.5	×	
21 ± 2	2	0.1	×	
20 ± 2	0.5	1.5	×	
18 ± 2	0.2	−0.7	×	
−15± 2	2	1.0		×
12 ± 2	0.2	−1.5	×	
−6± 2	0.2	0.7		×

depends on the electronic structure of the tip, as well as tunneling conditions. In order to analyze the influence of the tip identity on the measured height in STM profiles, a summary has been made in table 3.1. When scanning with a W-tip, the measured height differences between clean copper and oxidized copper stripes were between 12 and 140 pm. For O-tip the values were significantly lower, between 6 and 23 pm. The largest height difference and therefore the strongest contrast has been found for low currents (0.1–0.2 nA) and high voltages (0.7–1.5 V). Strong contrasts were found for both positive and negative polarities.

3.2 Nanostructures prepared by S co-adsorption

As discussed in detail in the section 1.3, after partial oxidation of Cu(110) and annealing to a temperature superior to 640 K, we will create a self-organized pattern, consisting of alternating clean and oxidized stripes. Recent work in our laboratory [89] has led to the introduction of a new method for preparation of such surface, which allows the creation of nanostructures with larger stripes than the classical method. As discussed in section 1.3.3, the self-ordering process is the result of an elastic

relaxation and is therefore influenced by the elastic and electrostatic properties of the surface. These properties can be modified by the presence of adsorbates, foreign atoms of different chemical element than the substrate. The new preparation method, which has been employed in the present thesis, consists in co-adsorbing sulfur before the annealing of the oxidized surface. In the recent thesis of Poulain, sulfur coverages up to $\theta_S = 0.05$, leading to the largest periodicity of < 40 nm, have been used for the preparation. In the present work, we have tested sulfur coverages up to 0.15 and reached a periodicity of ≈ 200 nm. Furthermore, the systematic study of the new preparation method has led to a new theoretical model, which successfully describes the experimental data [161].

The preparation has been done by the exposure to H_2S under the conditions described in section 2.6. The amount of sulfur on the surface has been measured by AES. This technique is very surface sensitive, but measures the average concentration on the surface. Therefore, if the sulfur is not distributed uniformly over the surface, but aggregated into islands, the amount of sulfur which is really influencing the nanostructure formation would not correspond to the amount measured by AES. Yet we believe that such agglomeration occurrence is seldom, since we do not observe sulfur in STM images after annealing (for $\theta_S \leq 0.15$, typical for the preparation method). Sulfur is known to be mobile on a copper surface, unless its diffusion is limited, like in the case of saturation or island formation around contaminations. So if sulfur islands occurred on the surface after annealing, we would have observed the c(2×2) phase, known for sulfur and described in section 1.4.

We have noticed an obvious trend that with increasing sulfur amount on the surface, the periodicity of the nanostructure with the same oxygen coverage increases. In Fig. 3.3, we can see examples of STM images with increased periodicity, prepared by sulfur co-adsorption.

In order to systematically follow this behavior, a study had to be performed, which covers all possible oxygen and sulfur coverages. Numerous nanostructures (totality of 104 nanostructures) have been prepared in order to test the preparation method and to find its limitations. The experimental conditions used for the preparation of nanostructures by S co-adsorption are given in section 2.6. After the exposure to reactive gases (O_2, H_2S), the surface was annealed to either 670 or 720 K. We have not observed a difference between the nanostructures annealed to one or the other temperature. From our experience, the order of the exposure to oxygen and sulfur does not affect the final structure. The increase in periodicity has been found to be very sensitive to the sulfur presence and already a sulfur coverage of 0.025

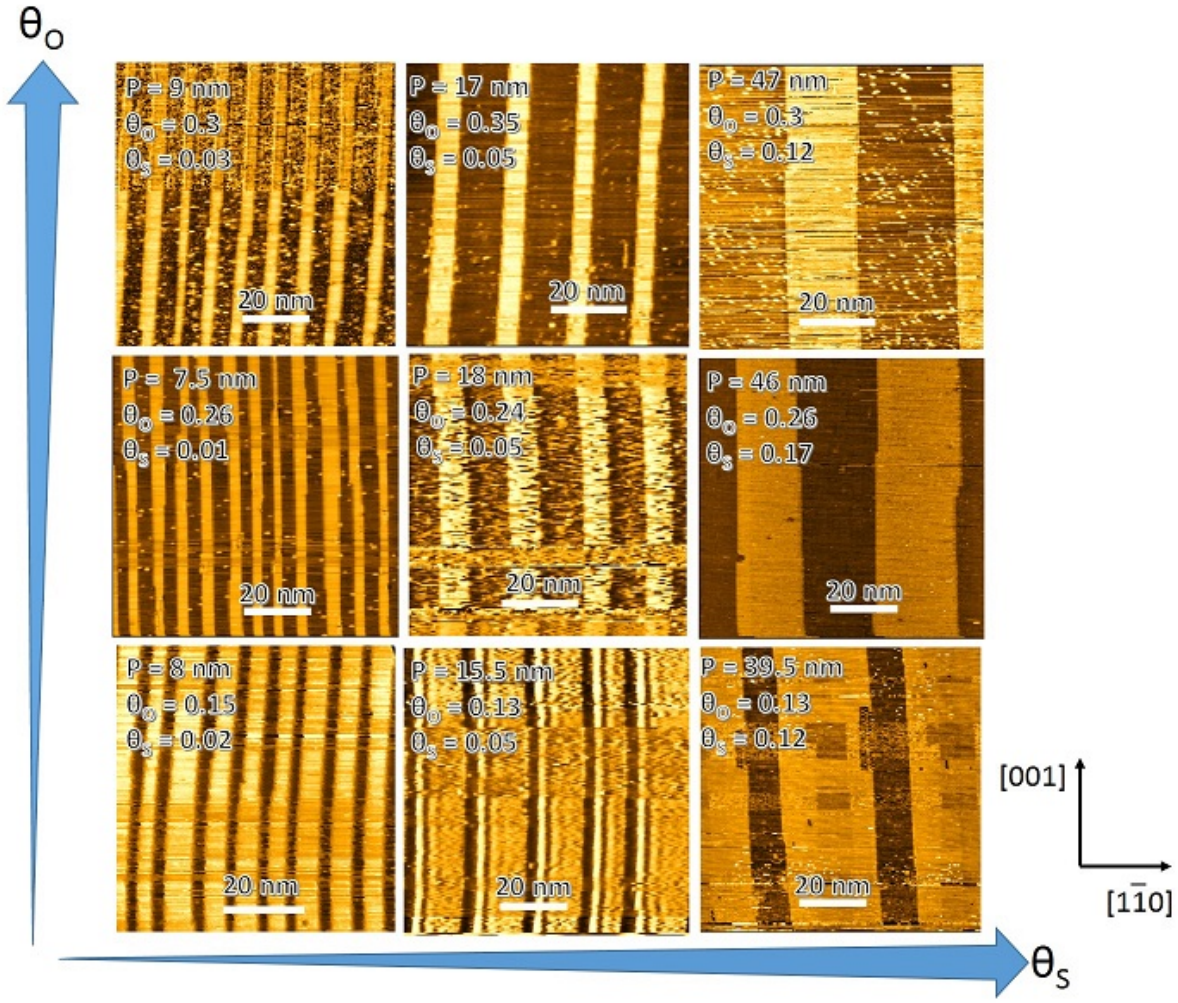

Fig. 3.3: STM images of nanostructures prepared by S co-adsorption ordered by increasing oxygen and sulfur coverage. The color gradient scale is different for each image, as it has been adjusted to show the best contrast.
Tunneling parameters of STM images from left to right:
$I = 0.2$ nA, $V = -1.5$ V; $I = 0.2$ nA, $V = -1.5$ V; $I = 0.2$ nA, $V = -1.5$ V;
$I = 0.2$ nA, $V = -0.7$ V; $I = 0.1$ nA, $V = 1.0$ V; $I = 0.8$ nA, $V = 1.5$ V;
$I = 0.2$ nA, $V = 0.7$ V; $I = 0.1$ nA, $V = 1.0$ V; $I = 0.5$ nA, $V = 1.5$ V.

showed a modified behavior. We have been able to prepare nanostructures with increasing periodicity by increasing the sulfur amount until reaching the value of approximately $\theta_S = 0.15$. For higher sulfur coverages the nanostructures tend to be much less periodic. The limit of the periodicity which can be reached is given by the size of the terraces, which was in most cases 200–400 nm.

The prepared nanostructured surfaces were studied by STM in order to systematically determine the periodicity (P) of the formed nanostructures, as well as the width of the oxidized (ω_{CuO}) and clean copper (ω_{Cu}) stripes. The values have been extracted from profile measurements on the STM images. As many periodicities as possible on one terrace were measured and averaged for the final result. Terraces are limited in size, therefore for larger periodicities, less stripes could be measured. This is the reason why they are given with a larger error than the smaller periodicities. We have not averaged over periodicities on different terraces, in order to keep the determination of the oxygen coverage local. The importance of the local measurement is discussed at the end of the chapter. Furthermore, it is important to study each surface at large scale (800×800 nm) in order to follow macroscopic changes to the surface, changes to step edges and terraces. The oxygen coverage θ_O is determined locally from the STM images by the equation:

$$\theta_O = \frac{\omega_{CuO}}{P}\theta_O^{sat.} \tag{3.1}$$

Because of the (2×1) reconstruction, the oxygen coverage at saturation $\theta_O^{sat.}$ is 0.5.

The sulfur coverage θ_S is determined by AES from the ratio of the AES peak height of sulfur (h_S at 152 eV) and the peak height of Cu (h_{Cu} at 920 eV) of the differentiated spectra. The peaks with the highest intensity have been chosen for both elements. The surface saturated with the c(2×2) phase of sulfur has a ratio $h_S/h_{Cu} = 0.5 \pm 0.1$. Since the coverage of such saturated surface corresponds approximately to a coverage θ_S of 0.5, we can calculate with the conversion factor of 1.

In Fig. 3.4 the parameters P, ω_{CuO} and ω_{Cu} of nanostructures prepared by the new method for different sulfur amounts are plotted and compared to the Marchenko-Vanderbilt model for the Cu(110)-(2×1)O nanostructure described in section 1.3.3. The equation of the model used in the graphs is the equation 1.10, with $a = 0.13$, $\theta_O^{sat.} = 0.5$ and $\frac{\gamma}{C} = 1.09$.

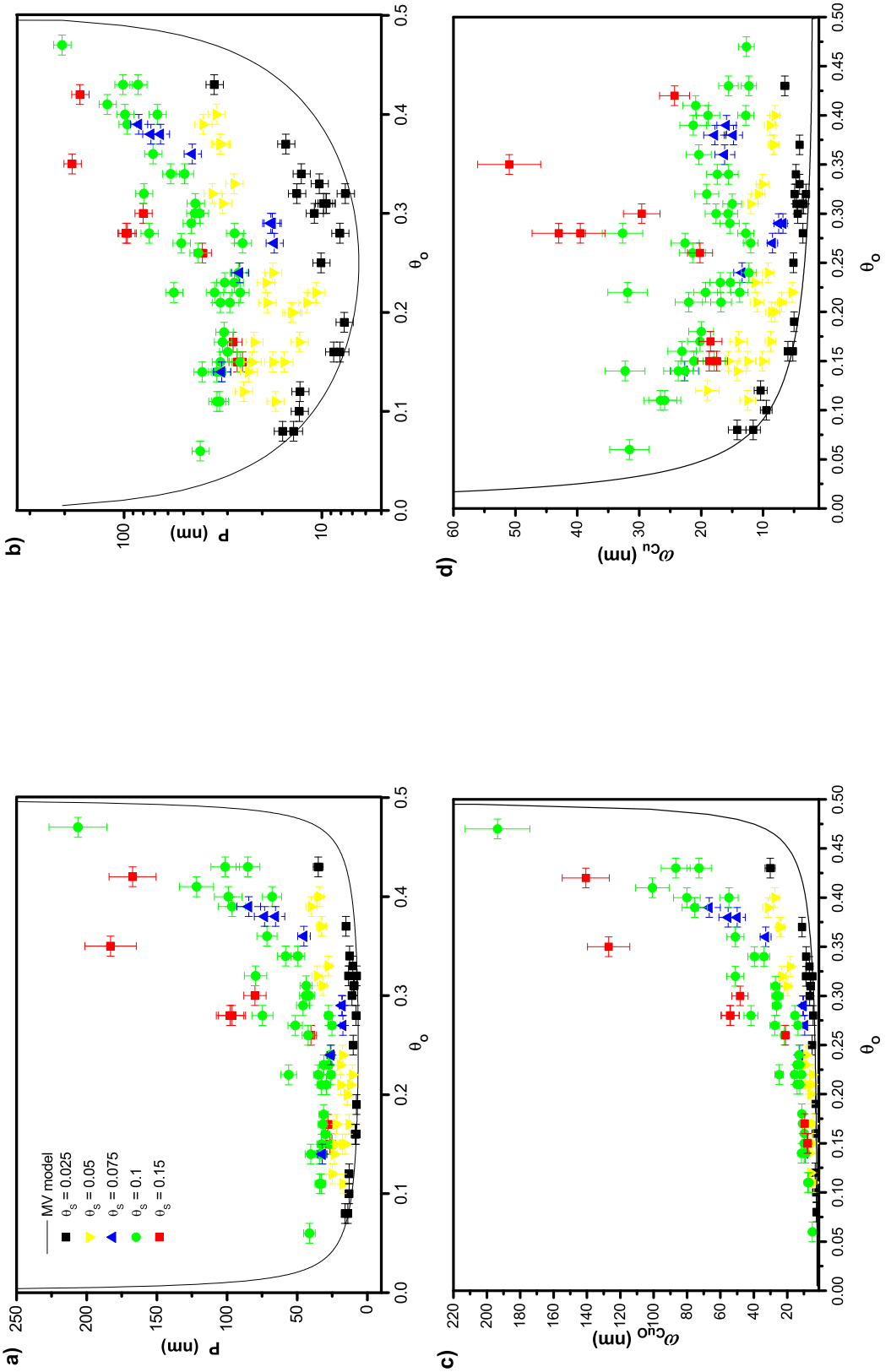

Fig. 3.4: Graphs of a) $P(\theta_O)$; b) the same graph with logarithmic scale; c) $\omega_{CuO}(\theta_O)$; d) $\omega_{Cu}(\theta_O)$. All graphs contain experimental data obtained for sulfur amounts of $\theta_S = 0.025$ (black squares), $\theta_S = 0.05$ (yellow triangles), $\theta_S = 0.075$ (blue triangles), $\theta_S = 0.1$ (green dots) and $\theta_S = 0.15$ (red squares). The black curve is the Marchenko-Vanderbilt model.

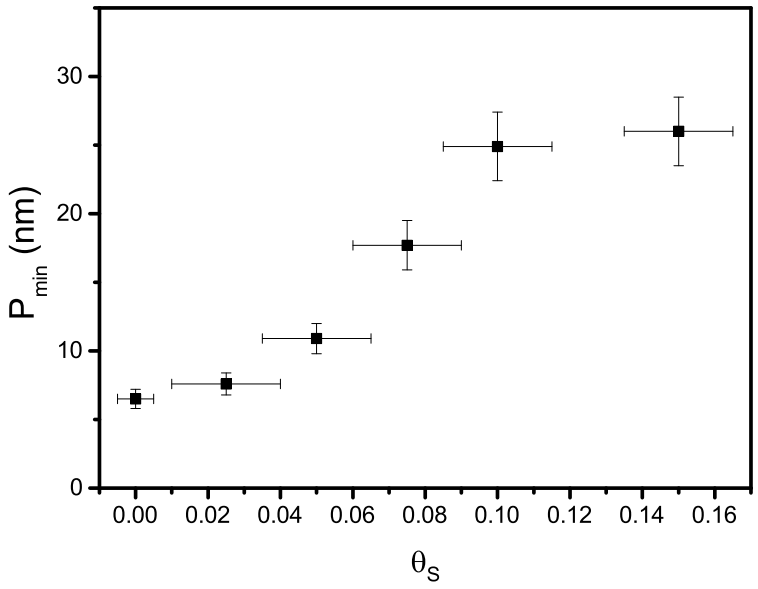

Fig. 3.5: Graph of $P_{\min}(\theta_S)$. The presence of sulfur increases the minimum periodicity.

The $P(\theta_O)$-graph has been plotted in a logarithmic scale (Fig. 3.4b)) for better visualization of differences between the points, but also in linear scale (Fig. 3.4a)), to simplify the comparison with other data. As we can see from the graph, contrary to the case of the classical preparation for the nanostructure, we are now able to obtain various periodicities for the same oxygen coverage. The periodicities that can be reached with the classical method for $0.1 < \theta_O < 0.4$ are only between 6.5 and 11 nanometers. By sulfur co-adsorption we can reach periodicity of several tens of nanometers for $\theta_O = 0.25$ (minimum of the Marchenko-Vanderbilt model). In Fig. 3.4c) and 3.4d) we can also see the behavior of the width of the individual stripes with increasing sulfur amount.

In the $P(\theta_O)$-graph, we notice that the minimum periodicity is increasing with increasing sulfur amount. To better visualize this trend, we have plotted the estimated minimum periodicity $P_{\min}$ as a function of the sulfur amount in Fig. 3.5. The increase in this range seems linear.

The periodicities obtained for the same sulfur amount show a large variation and it would be difficult to describe their behavior by a function without a large error. One of the factors that plays a role here is the already discussed error in the sulfur amount determination, which is caused by using a non-local technique, such as AES. This determination also lacks precision because of the relatively large error for the h_S/h_{Cu} value. Yet this is not the only reason causing the large distribution of the points in the $P(\theta_O)$-graph. We found that the presence of sulfur is not the only influence increasing the periodicity of the nanostructures and thus we are in

fact observing the result of a combination of different factors. The other influences will be discussed in the following section.

3.3 Influence of step bunching

In order to analyze the influence of the presence of sulfur on the change of the periodicity, it is necessary to identify all the factors having an influence on this change. From the literature we know the work of Bobrov and Guillemot [74], which have also increased the periodicity of the Cu(110)-(2×1)O nanostructure. The authors have introduced a method using a thermally assisted oxygen adsorption and precursors for the domain formation. Fig. 3.6 is adapted from Ref. 74 and shows the periodicities that they have been able to prepare by this method. The authors explain the increased periodicity by a size-dependent elastic relaxation. We have however observed increased periodicities even without using precursors, when we annealed the surface numerous times or to higher temperatures (870 K). This procedure is known to cause step bunching on the surface. In fact, the authors anneal their precursors in the temperature range from 400–880 K, where the step bunching is believed to be formed. And therefore we conclude that the increased periodicity is not only the outcome of the precursor method, but is directly linked to the extra strain induced by the step bunching. Additionally, annealing to high temperatures, especially in the presence of oxygen, could have led to segregation of contaminants, such as sulfur, from the bulk to the surface, which would also increase the periodicity.

Since we have now identified an additional factor influencing the increase of the periodicity, we can more closely discuss the variations we have observed for periodicities with the same sulfur amount. An example of a variation of the periodicity is shown as the two green points in Fig. 3.7, which have the exact same oxygen and sulfur coverage, yet differ in periodicity.

The reason for the existence of two different periodicities for the same sulfur and oxygen amounts can be found, when looking at the macroscopic structure of the two surfaces. We have found that increased periodicities are present on surfaces with large terraces separated by step bunches. An example of such surface is shown in Fig. 3.8a). Surface faceting is known to occur on vicinal Cu surfaces exposed to oxygen at elevated temperatures [162–164]. During annealing, the width of the terraces increases and step bunches of different heights are formed as long as the gain of energy from the surface faceting is larger than the energy loss from increasing

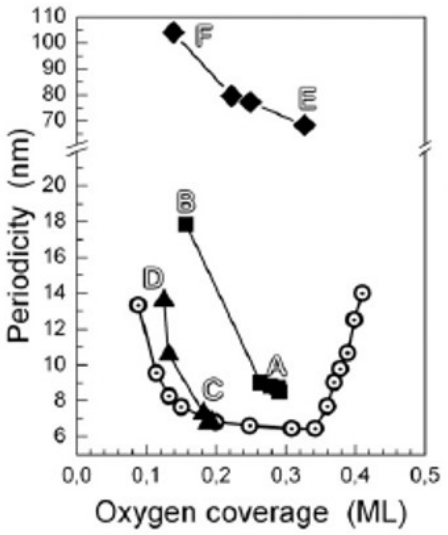

Fig. 3.6: P(θ_O) adapted from Ref. 74. The black forms represent periodicities of nanostructures prepared by Bobrov *et al.* by the thermally assisted precursor method and the blank circles are points from Ref. 7.

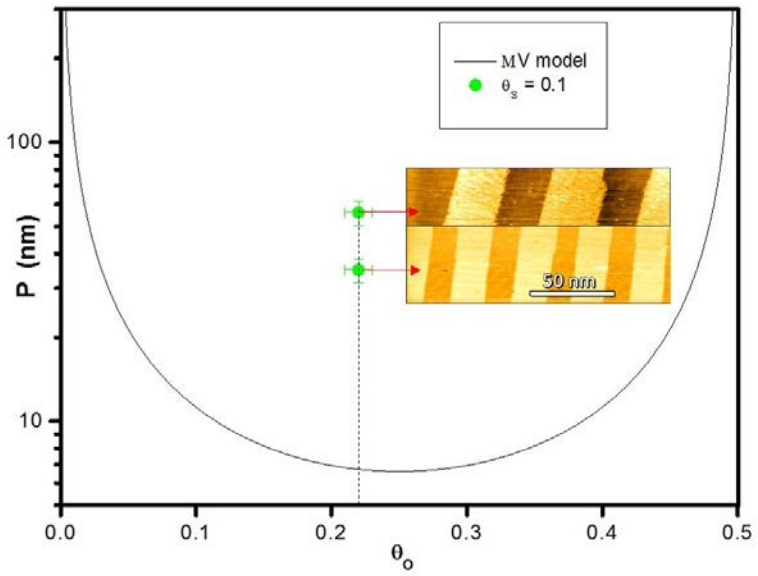

Fig. 3.7: Influence of step bunching: Graph of P(θ_O) showing two experimental points with same oxygen coverage and same sulfur amount, but different periodicities. The corresponding STM images are shown next to the points. W-tip in both images. The increased periodicity is caused by the effect of step bunching.

step density in the bunches. Guillemot and Bobrov observed step bunching of the Cu(110)-(2×1)O surface in the 455–570 K temperature range [75]. Annealing at temperatures superior to 570 K does not lead to an increase in step density, however the surface is still being rearranged. The authors have found the terrace width to increase from an average of 220 nm to 450 nm in the 570–810 K temperature range. The corresponding step bunch height has been found to increase up to 14 monoatomic steps. Since the step density remains constant, there is no more energy being won by this surface rearrangement. The authors explain the mechanism as follows. During thermal annealing a "fluid phase" is formed which can precipitate when the surface is cooling down via two different channels. Either Cu–O fragments attach to already existing CuO stripes or Cu–O further dissociates by incorporation of Cu atoms into terrace edges, making terraces grow in the lateral direction. The freed mobile oxygen abstracts Cu atoms preferentially from the edges of the terrace with lower CuO stripe density. Therefore terraces with lower stripe density will shrink and *vice versa*. Such rearrangement of surface will induce new surface strain and therefore have an influence on the periodicity of the formed nanostructure. The introduction of local strain into the Cu(110)-(2×1)O surface by thermal annealing has been reported in Ref. 165 and 81.

In our experiments we have annealed in the temperature range 670–720 K and our observations are in agreement with the surface rearrangement presented in Ref. 75. In Fig. 3.8 we can see an example of a surface with large terraces and step bunches, as well as a surface with narrow terraces alternating with monoatomic steps. Both STM images and corresponding profiles are shown. We have observed terraces with width in the range 400–600 nanometers alternated by step bunches of several steps (5–20). A clean surface without step bunching would have typically terraces with widths in the 30–90 nm range.

The presence of step bunches on a nanostructured surface is believed to have an influence on the diffusion of the Cu–O chains. Guillemot and Bobrov have shown, how oxidized stripes on a high-lying terrace are aligned with the stripes of the neighboring low-lying terrace if the two terraces are separated by one monoatomic step. This is due to the short-range interactions between the stripes. They have found that the stripes are not aligned if terraces are separated by a step bunch consisting of several steps, which represents a larger barrier for the interactions [75]. In Fig. 3.9 these STM images from literature are shown next to our STM images, which do not confirm this observation. We have seen non-aligned stripes for terraces divided by only one step, as well as perfectly aligned stripes separated by a step

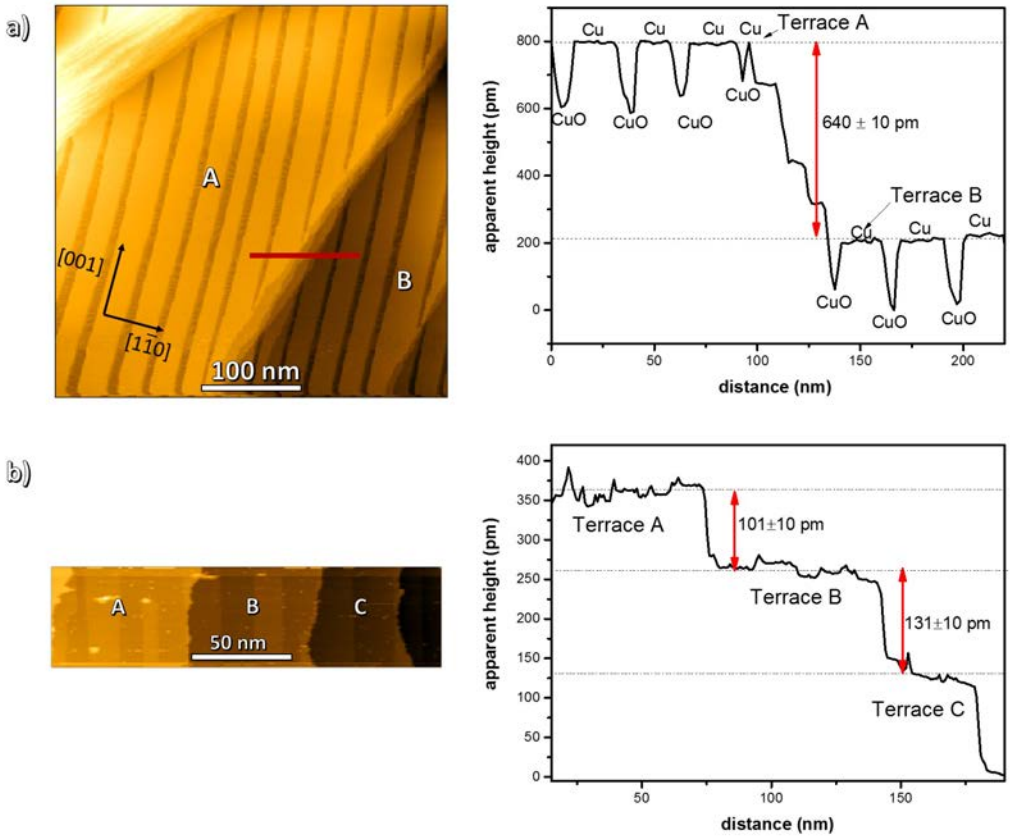

Fig. 3.8: a) STM image and a height profile of a typical step bunch. The profile has been measured along the red line in the image. The step bunch consists of 5 monoatomic steps which are not covered by oxygen. Theoretical height of a monoatomic copper step is 128 pm. The terraces are 280 ± 10 nm (A) and 150 ± 10 nm (B) wide. b) STM image and a height profile of terraces divided by monoatomic steps. The profile has been measured perpendicular to the step edges. The measured step heights are 101 ± 10 and 131 ± 10 pm. The terraces are 69 ± 5 nm (A), 67 ± 5 nm (B) and 55 ± 5 nm (C) wide. Tunneling parameters: a) $I = 0.2$ nA, $V = 0.7$ V; b) $I = 0.2$ nA, $V = -1.5$ V. W-tip in both images.

bunch. However, according to our experience, inhomogeneous oxygen coverage is more likely found on a faceted surface. This in fact implicates a lower diffusion of oxygen over the surface, but we have evidence that there is a short-range interaction between oxidized stripes causing their alignment even over several steps.

In conclusion, we have identified other factors that can influence the periodicity of the Cu(110)-(2×1)O nanostructure, namely the presence of step bunching. We have found that the effect of step bunching is larger for nanostructures with low oxygen coverage and the effect of sulfur co-adsorption for the ones with high oxygen coverage. We can anneal a nanostructured surface prepared by sulfur co-adsorption and further increase the periodicity by combining both effects. While introducing strain into the surface by step bunching can lead to increased periodicity, the increase is not as significant as for preparation via S co-adsorption and even more importantly, this method is much less precise and controllable than the S co-adsorption method.

As a direct result from the previous observations for our experiments, we have learned that if we wish to see only the effect of sulfur on the change in the periodicity, we need to keep the number of annealing cycles and the annealing temperature as low as possible. This will minimize the step bunching. In our experience several cycles of annealing at 670 or 720 K do not cause a significant change to P due to step bunching. We have observed visible faceting of the surface, when annealing to 870 K with the presence of sulfur and oxygen.

3.4 Modified Marchenko-Vanderbilt model for the S co-adsorption method

In our experiments, we have seen that the change in periodicity is very sensitive to the sulfur amount on the surface. In order to calculate a model for $P(\theta_O)$ in the presence of sulfur, we need to make sure that all points for one $P(\theta_O)$-curve were measured with the same amount of sulfur. We have done this by measuring the periodicity for one sulfur amount and different oxygen coverages consecutively. First, we prepared a nanostructure with a certain sulfur amount and low oxygen coverage and then we oxidized in steps to obtain points in the $P(\theta_O)$-graph going from low to high θ_O. In this way, each surface has been exposed to exactly the same amount of sulfur. After obtaining such a curve for a certain sulfur amount, several cycles of sputtering and annealing were performed, in order to get rid of the possible step bunching. To obtain results for one sulfur coverage we annealed up to 10 times to

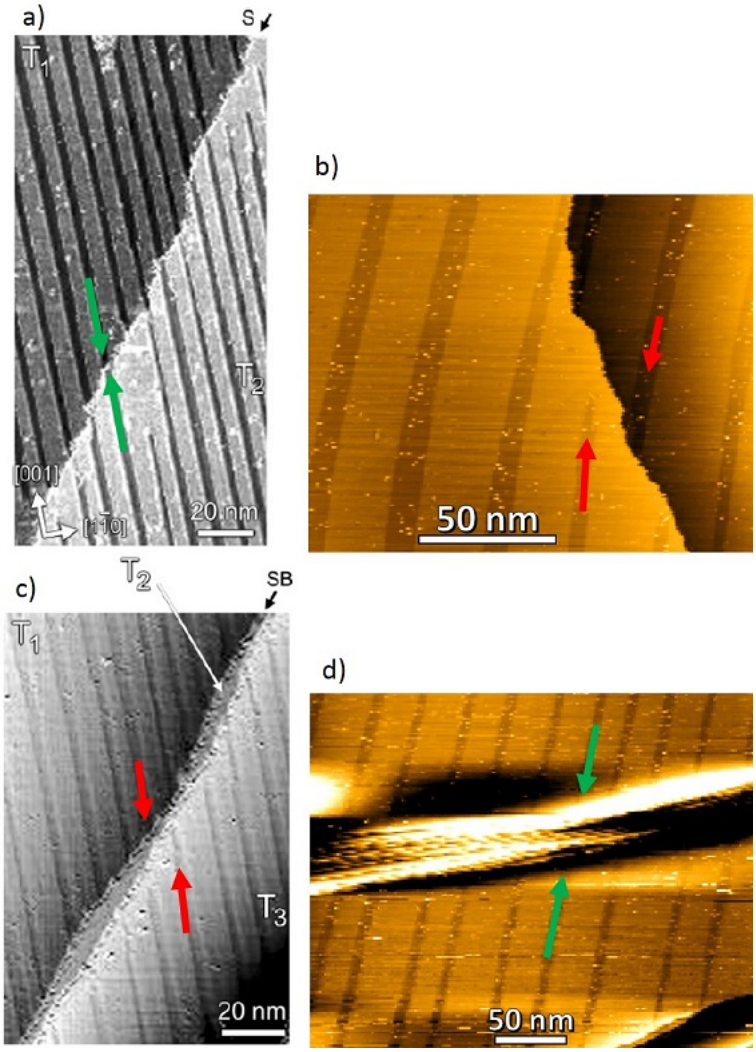

Fig. 3.9: a) and c) are STM images from Ref. 75 showing that alignment of oxidized chains is only present on terraces separated by one step. b) STM image of two terraces separated by one step with stripes not aligned. d) STM image of two terraces separated by a step bunch with stripes aligned. Tunneling parameters: $I = 0.2$ nA, $V = -1.5$ V for b) and d). W-tip in both images.

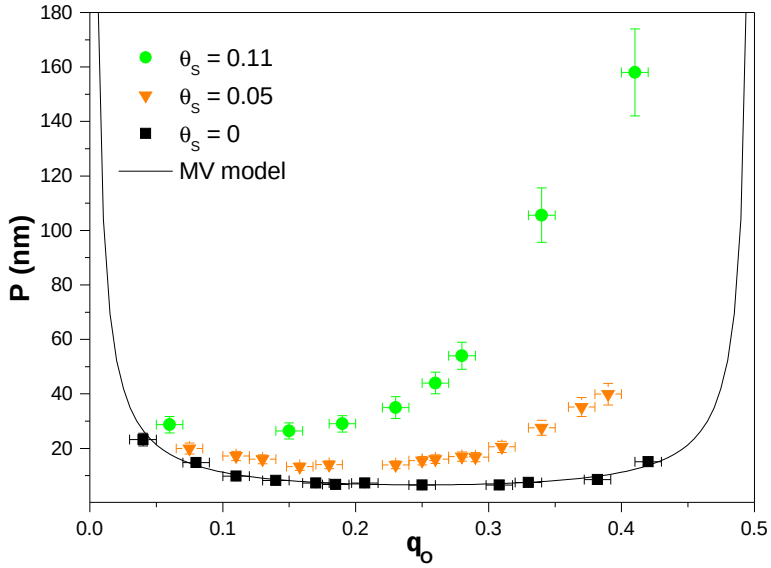

Fig. 3.10: Graph of $P(\theta_O)$ for sulfur amounts $\theta_S = 0$ (black squares), $\theta_S = 0.05$ (orange triangles) and $\theta_S = 0.11$ (green dots). The curve is the Marchenko-Vanderbilt model.

670 or 720 K, which according to our observations is not enough to influence the periodicity due to step bunching.

In Fig. 3.10, we can see the results obtained for three different sulfur amounts. In contrary to the graphs in Fig. 3.4, the points clearly describe a curve. Our method has been successful in eliminating the different factors causing large distribution of periodicities for the same θ_O and θ_S. Points are shown for the sulfur amounts of $\theta_S = 0$, $\theta_S = 0.05$ and $\theta_S = 0.11$.We have previously seen that the sulfur presence increases the values of P_{min}. From the graph in Fig. 3.10, it becomes obvious that P_{min} is also shifted in the direction of lower oxygen coverage with increasing sulfur amount. While the Marchenko-Vanderbilt model is symmetrical and has a minimum at exactly half coverage ($\theta_O = 0.25$), the minimum for $\theta_S = 0.05$ is at $\theta_O = 0.17$ and for $\theta_S = 0.11$, the minimum is at $\theta_O = 0.11$.

To describe the influence of sulfur, we propose a modification to the Marchenko-Vanderbilt model by adding a term A, which will take into account the change of the term $\frac{\gamma}{C}$, the ratio between the local boundary creation energy and the sum of the elastic and electrostatic constants of the system. The term $\frac{\gamma}{C}$ is surface specific

and therefore it is understandable that the presence of an adsorbate influences its value. The modified model is as follows:

$$P(\theta_{\mathrm{O}}) = \frac{2\pi a}{\sin\left(\pi \frac{\theta_{\mathrm{O}}}{\theta_{\mathrm{O}}^{\mathrm{sat.}}}\right)} \exp\left(1 + \frac{\gamma}{C} + A\right) \tag{3.2}$$

We have seen that P_{min} increases with increasing sulfur amount, which means that the parameter A depends on θ_{S}. The fact that P_{min} is shifting to lower θ_{O} values indicates that A also depends on θ_{O}. In order to evaluate this dependency we have calculated the values of A for each point in the $P(\theta_{\mathrm{O}})$-graph, obtained by the successive measurements, using the expression:

$$A = \ln\left[\frac{P \sin\left(\pi \frac{\theta_O}{\theta_O^{\mathrm{sat.}}}\right)}{2\pi a}\right] - 1 - \frac{\gamma}{C} \tag{3.3}$$

The calculated values of $A(\theta_{\mathrm{O}})$ are shown in Fig. 3.11 for different sulfur amounts. A clearly depends linearly on θ_{O}. We have found the slope of $A(\theta_{\mathrm{O}})$ to be proportional to θ_{S} with the proportionality factor of 69.5 ± 3.5. Therefore $A = 69.5\ \theta_{\mathrm{O}}\theta_{\mathrm{S}}$. As we can see in the graph, the calculated values for A, for the case without sulfur, are around 0. With the corrective term A equal to zero, we obtain the classical Marchenko-Vanderbilt model. Furthermore, we can notice that the value for A seems to saturate at the value of around 2.6 for $\theta_{\mathrm{S}} = 0.11$ and $\theta_{\mathrm{O}} > 0.34$. This saturation is probably linked to the saturation of the total surface coverage $\theta_{\mathrm{O}} + \theta_{\mathrm{S}}$.

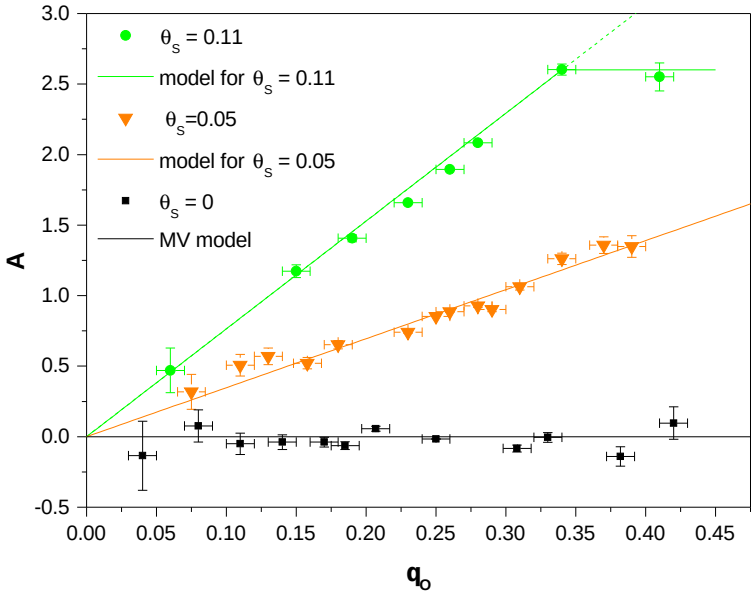

Fig. 3.11: Graph of calculated values of A as a function of θ_O for the sulfur amounts $\theta_S = 0$ (black squares), $\theta_S = 0.05$ (orange triangles) and $\theta_S = 0.11$ (green dots). The curves correspond to the function $A = 69.5\ \theta_O\theta_S$. The value seems to saturate at $A \approx 2.6$ for $\theta_S = 0.11$ and $\theta_O > 0.34$.

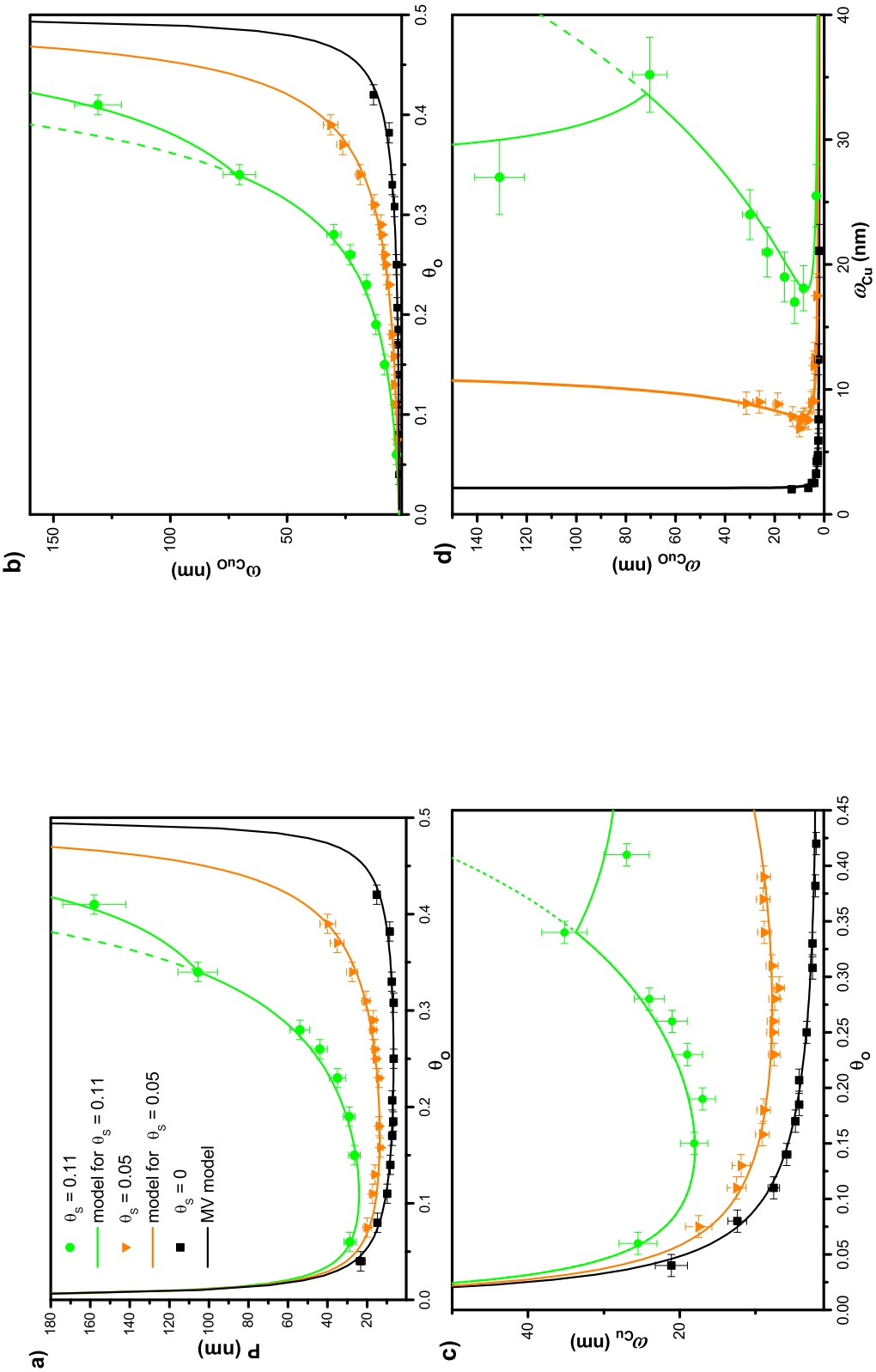

Fig. 3.12: Experimental data for a) $P(\theta_O)$; b) $\omega_{CuO}(\theta_O)$; c) $\omega_{Cu}(\theta_O)$ and d) $\omega_{CuO}(\omega_{Cu})$, obtained for sulfur amounts $\theta_S = 0$ (black squares), $\theta_S = 0.05$ (orange triangles) and $\theta_S = 0.11$ (green dots). The curves are the modified Marchenko-Vanderbilt model.

Fig. 3.12a) shows the curves $P(\theta_O)$ with the modified Marchenko-Vanderbilt model. In Fig. 3.12b) and 3.12c) the graphs for $\omega_{CuO}(\theta_O)$ and $\omega_{Cu}(\theta_O)$ are shown. We have seen that the term A tends to saturate for high oxygen coverages. As a consequence there is a discontinuity in the increase of P. We have also observed a decrease for the width of the clean copper stripe ω_{Cu} for high oxygen coverages. In the $\omega_{Cu}(\theta_O)$-graph (Fig. 3.12c)), we can see that according to the modified model for $\theta_S = 0.11$ (green line + green dashed line), the values for ω_{Cu} should rapidly increase for $\theta_O > 0.2$. However, the largest copper stripe width for $\theta_S = 0.11$ experimentally observed has been $\omega_{Cu} = 35 \pm 3$ nm. The fact that there is a limit to the value of ω_{Cu} confirms the observed saturation of A for high oxygen and sulfur coverages. In all the graphs, the modified model is shown as a dashed line in the region where it comes to saturation. The continuation of the curves are thereafter calculated for the value $A = 0.26$. It is to show that the model is valid until a certain coverage, but describes the experimental data better for higher coverages, when a saturation of the corrective term is assumed.

Our experimental results for classically prepared nanostructures show a very good agreement with the Marchenko-Vanderbilt model. We insist on the importance of measuring the periodicity by a local method, like STM. We have found that the oxygen coverage on different terraces can vary, due to hindered diffusion of oxygen by steps. By calculating the oxygen coverage from the width of oxidized stripes in STM images for each terrace separately, we obtain more precise results than would be possible with a non-local method. In the past, diffraction methods (e.g. He-diffraction, grazing incidence x-ray diffraction) have been used to determine the periodicity and oxygen coverage of the system [7, 79]. Using these methods, one can determine only the overall oxygen coverage of the whole sample. Local inhomogeneities in oxygen coverage will not be considered and therefore the results often are not in agreement with the elastic model. This is especially pronounced for oxygen coverages lower than 0.1 and higher than 0.4, where the structure tends to be less periodic. The distribution of the periodicities is larger, which is explained by the steep slope of the $P(\theta_O)$-curve for $0.1 > \theta_O > 0.4$. The distribution of periodicities prepared by the S co-adsorption method is also defined by the slope of the $P(\theta_O)$-curve. In Fig. 3.13, the intervals where good distribution is expected for each sulfur coverage are highlighted by the colored rectangle. We can see that the modified Marchenko-Vanderbilt model for high sulfur amounts has a small slope in only limited interval around the minimum. So while the classically prepared nanostructures will be highly periodic for $0.1 < \theta_O < 0.4$, this range for nanostructures with $\theta_S =$

0.11 will be only between 0.05 and 0.2. This is why it is more difficult to obtain highly periodic nanostructures with increased periodicity. Nevertheless the local determination of the oxygen coverage by STM shows that the results agree with the prediction of the model.

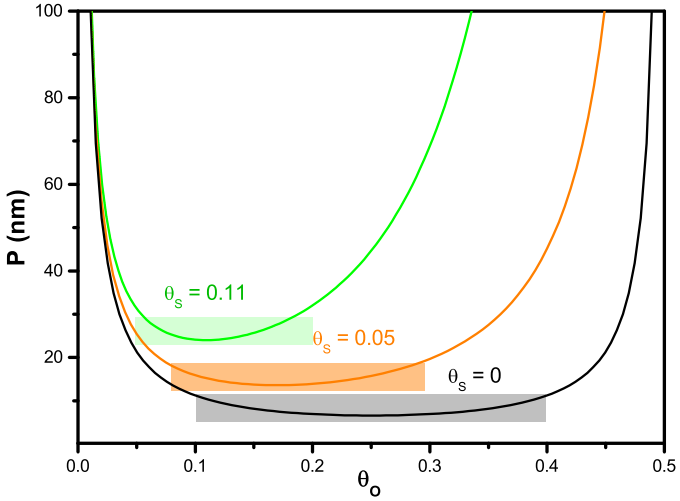

Fig. 3.13: Distributions of periodicities: the intervals highlighted by the colored rectangles are the range in which the slope of the $P(\theta_O)$-curve is small and therefore a good distribution of periodicities is expected.

3.5 Summary and discussion

In this chapter, we have presented the new preparation method for the Cu(110)-(2×1)O nanostructure, consisting in co-adsorption of low amounts of sulfur. With this method, we have been able to prepare periodic nanostructures with periodicities reaching up to 200 nanometers. More than 100 nanostructures were prepared during the study and we have characterized the limitations and advantages of this method. First of all, this method presents a relatively easy and straightforward way to prepare self-organized nanostructures with increased periodicities. Contrary to the classical method, we can now prepare nanostructures with different periodicities for the same oxygen coverage. We simply choose the parameters P and θ_O we wish, by choosing respectively the ω_{CuO} and ω_{Cu} value, and adsorb the corresponding oxygen and sulfur amount on the surface. The desired nanostructure can so be prepared in just one step. We have added a corrective term, A, to the Marchenko-Vanderbilt model, which describes the influence of sulfur. A can be seen as an added term to the surface energy creation, probably associated with the interaction between oxygen and sulfur, as it is proportional to the product of the oxygen and sulfur coverages. In order to better

understand the role of sulfur in the change of periodicity, it is important to know, on which sites the sulfur is adsorbed and where it is found after the annealing. However we cannot answer this question by the means of STM measurements, since sulfur is highly mobile on copper and therefore cannot be imaged at room temperature. To clarify the position of sulfur on the surface we would thus need to either cool down to very low temperatures to hinder the diffusion of sulfur or perform different experiments. We hope that by the means of XPS it could be possible to identify where the sulfur is bound.

While preparing the many nanostructured surfaces during the study, we have been able to identify possible sources for deviations from the model. First of all, it is the influence of step bunching described previously in detail. It seems to us that the presence of sulfur on the surface during annealing causes even more step bunching than just the presence of oxygen. Therefore after a multitude of annealing cycles with adsorbed sulfur and oxygen, the surface had to be carefully sputtered. During our study we even had to re-polish the sample electrochemically to remove the faceting, which came about after the many months of repeating the preparation of a nanostructured surface. Introducing step bunching on purpose can be a method to further increase the periodicity of a nanostructure, yet it is not possible to do so in a controlled way.

Another source of deviations from the model can be the presence of contaminations on the surface, which also induce a local strain to the surface. Variations in sulfur amount can also be caused by segregation of sulfur from the bulk during annealing. Since sulfur is a typical contaminant found in copper, the annealing temperature has to be carefully chosen. We have rarely observed an increase in sulfur amount after annealing to 670/720 K.

Chapter 4

Sulfidation of the Cu(110)-(2×1)O nanostructure

The present chapter is dedicated to the study of sulfidation of the nanostructured Cu(110)-(2×1)O surface. The influence of the width of oxidized stripes on the surface reactivity has been studied by STM during exposure to H_2S and the kinetics of the reaction have been studied by AES. Using the new fabrication method for the nanostructure described in chapter 3, we have prepared surfaces with wide oxidized stripes ($\omega_{CuO} > 17$ nm) and we have observed a new reaction mechanism: The combination of Cu–O chain detachment from stripe borders and formation of sulfur islands on the oxidized stripes.

In the first part of the chapter, we will discuss various aspects that need to be considered, when performing STM measurements during exposure to a reactive gas. We will then shortly present results of the kinetic AES measurements and continue with the STM study of the reaction mechanisms. The reaction mechanisms of sulfidation of a nanostructure with narrow oxidized stripes ($\omega_{CuO} \approx 3$–10 nm) has previously been debated in Ref. 89 and are therefore not discussed in detail here. We will present the mechanisms only for comparison with the reaction mechanisms for wide oxidized stripes. The second part of the chapter deals with the formation of S-c(2×2) islands. We will present the influence of the exposure conditions (pressure) on the reaction mechanisms and also discuss the observed modifications of the structure of steps caused by the sulfidation.

4.1 STM during sulfidation

When studying dynamic processes on the surface by STM, two strategies can be chosen, a so-called "quench and look" approach or "on-site on-time" approach, which we have chosen in this thesis. The former strategy involves freezing a dynamic system by lowering the temperature and investigating it. The later approach provides a possibility to follow a dynamic system quasi-simultaneously, by recording consecutive STM images during the process. Pitfalls of this approach, such as thermal drift and interaction of the surface with the STM tip are discussed in Ref. 166. In this section, we will describe in detail the experimental design we have chosen for our STM study and the challenges that had to be overcome or considered.

Our approach to study the reaction mechanisms of sulfidation of the nanostructured O/Cu(110) surface, was to scan by STM during exposure to sulfur and thereby "film" the reaction on the surface. First of all, the opening of a gas leak valve could lead to vibrations to which STM is very sensitive. This could cause noise in images and in the worst case crashing of the tip. Next, we have to note that our UHV system consists of two chambers connected by a passage with limited conductance. The H_2S leak valve and the pressure gauge are situated in the preparation chamber, while the experiments are carried out in the STM chamber. Consequently, we cannot precisely determine the pressure we are exposing the sample to during an STM measurement. For example, when exposing a sample in the preparation chamber, exposure to 0.45 L H_2S is enough to see adsorbed sulfur in c(2×2) configuration on the CuO stripes. In contrast, when the sample is in the STM chamber, the exposure has to be sometimes more than ten times higher in order to see any sulfur on the surface. It has been estimated that during exposure, the difference between the local pressure at the sample position and the position where the pressure is measured, is around two orders of magnitude. All exposures given in this chapter have been calculated using the pressure in the preparation chamber, while the sample has been in the STM chamber during the exposure.

We have found that the position of the STM tip above the sample and the shape of the tip apex significantly influence the real exposure to the surface. When exposing to relatively low H_2S pressures (typically 1×10^{-8}–5×10^{-8} mbar), the tip can block the molecules in their path towards the surface, what we call a "shadow effect". Since the area of the surface being scanned is typically between 5 to 800 nanometers and a sharp STM tip will have an apex radius of few tens of nanometers, the microscopic structure of the tip apex will have an important influence. The Fig. 4.1 schematically explains, how the shape of the tip influences the exposure of the scanned surface.

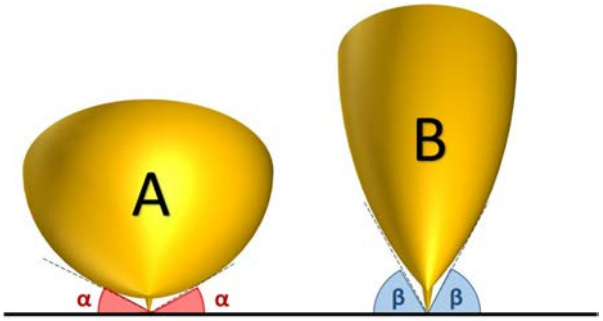

Fig. 4.1: Schematic representation of the "shadow effect" of the STM tip apex. Tip A casts a greater "shadow" than tip B.

The tip A has a larger radius and therefore the angle, α, from which the molecules can access the surface, is smaller than for the tip B. We have often witnessed the "shadow effect", when imaging by STM during the sulfidation. The area of the surface that has not been scanned by STM during the exposure would have a higher coverage, than the surface that has been under the shadow of the tip. This is why when working with a new tip for the first time, the experiment has to be carried out beginning with low pressure until we have a sense of the real exposure rate.

To quantify the possible discrepancies caused by the "shadow effect", the table 4.1, which summarizes examples of the sulfur coverage observed in STM images after different exposures, has been created. The sulfur coverage is given as a percentage of the oxidized stripe area. It is important to keep in mind that during the sulfidation the edges of the oxidized stripes are attacked and therefore the higher the sulfur coverage is, the more difficult it is to estimate the area that has been covered by the oxidized stripe before the sulfidation began. Fig. 4.2 shows the corresponding STM images to the data in table 4.1. During STM measurements with the tip A, the coverage rate has been calculated to be $1.6 \pm 0.3 \times 10^{-4}$ L^{-1} and for the tip B, this rate is two orders of magnitude higher, namely $2 \pm 0.6 \times 10^{-2}$ L^{-1}. We conclude that it is difficult to compare exposures of measurements with different STM tips.

4.2 Reaction kinetics: sulfidation of the clean and oxidized Cu(110)

We have followed the kinetics of the sulfidation reaction on clean and oxidized (saturated and nanostructured) Cu(110) surfaces, by AES. We evaluate the sulfur and oxygen amounts on the surface using the ratio of the sulfur and oxygen peak

Table 4.1: Summary of sulfur coverage determined from STM images after different exposures and during measurements using 2 different STM tips (A and B). The periodicity and width of the oxidized stripes before exposure are given. The exposure is calculated using the pressure measured in the preparation chamber. Only the sulfur adsorbed on Cu adatoms of the (2×1)O-phase is considered, since only this sulfur is visible in STM images.

Tip ID	Exposure (L)	% of CuO stripe covered by S	P (nm)	ω_{CuO} (nm)	θ_O	STM image
A	86 ±1.5	1.4 ±0.5	63.5	28.5	0.22	Fig. 4.2a)
A	325 ± 1.5	5 ±1	63.5	28.5	0.22	Fig. 4.2b)
B	6.8 ± 1.5	8 ±1	61.5	25	0.2	Fig. 4.2c)
B	9 ± 1.5	21 ±2	61.5	25	0.2	Fig. 4.2d)

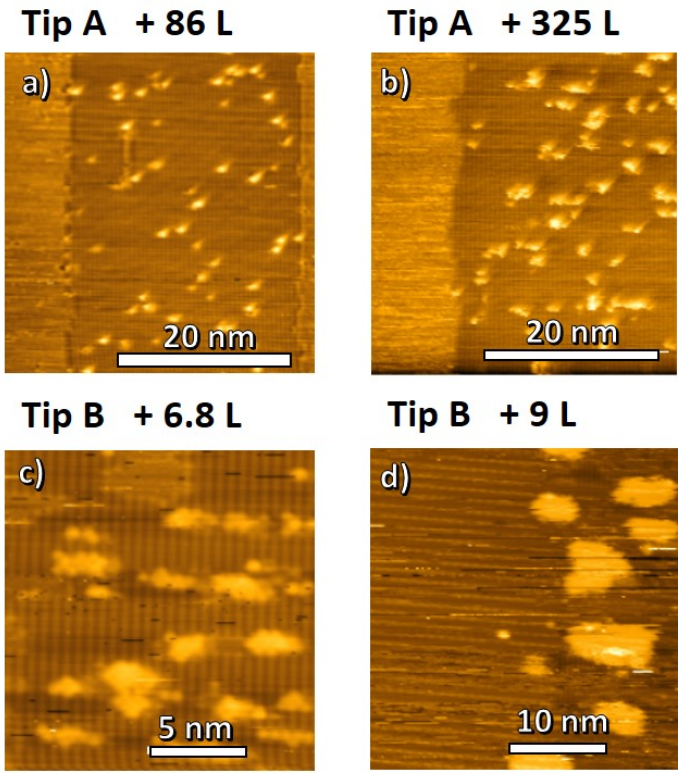

Fig. 4.2: STM images of sulfur adsorbed on CuO stripes. The nanostructures have been exposed to H_2S during the STM measurement with two different tips, A and B. Tunneling conditions for a)–b) $I = 0.2$ nA, $V = -1.5$ V and for c)–d) $I = 0.2$ nA, $V = -1.0$ V. W-tip in all images.

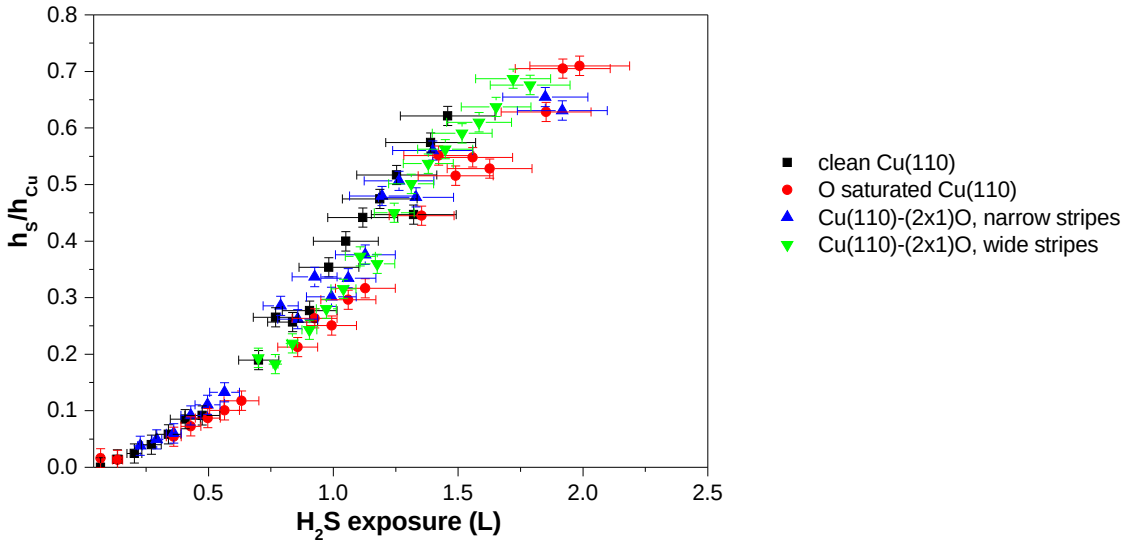

Fig. 4.3: Increase of the sulfur signal in AES during sulfidation of 4 different surfaces: clean Cu(110) (black squares), oxygen-saturated Cu(110) (red circles), nanostructured Cu(110)-(2×1)O with $P = 7$ nm, $\theta_O \approx 0.25$ (blue triangles) and nanostructured Cu(110)-(2×1)O with $P = 45$ nm, $\theta_O \approx 0.25$ (green triangles). As a consequence of the different initial sulfur amounts, the raw data curves are not superposed and therefore the data have been shifted in the x-direction in order to better compare the shape of the curves.

respectively to the copper peak in the AES derivative spectra. We use the oxygen peak at 503 eV, sulfur at 152 eV and copper at 920 eV. The precise experimental conditions are described in section 2.6. In Fig. 4.3 and 4.4 we can see the evolution of the sulfur and oxygen signals, respectively, as a function of the exposure. We demonstrate experimentally that during the exposure to H_2S the sulfur amount on the surface increases. In the case of the previously oxidized surfaces, the oxygen signal decreases, thus confirming the supposed total reaction:

$$H_2S + O_{ad} \longrightarrow S_{ad} + H_2O \uparrow$$

We have compared the kinetics for the oxygen-saturated and clean Cu(110) and two nanostructured surfaces, one with wide ($\omega_{CuO} \approx 20$ nm) and one with narrow ($\omega_{CuO} \approx 3.5$ nm) oxidized stripes. We have not observed a significant change in the reaction kinetics, however, as later presented, these reactions follow different reaction

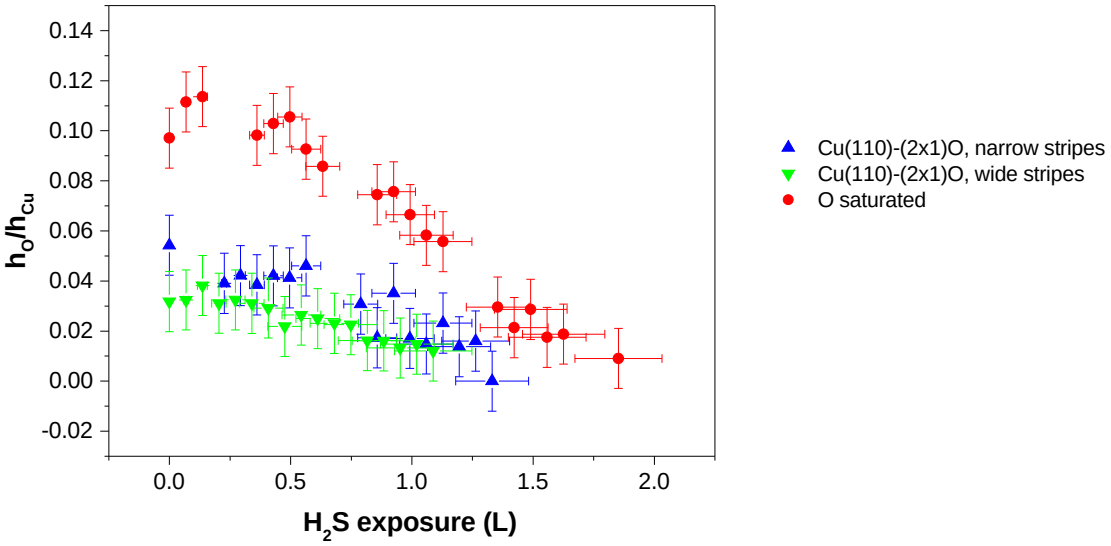

Fig. 4.4: Decrease of the oxygen signal in AES during sulfidation of 3 different surfaces: oxygen-saturated Cu(110) (red circles), nanostructured Cu(110)-(2×1)O with $P = 7$ nm, $\theta_O \approx 0.25$ (blue triangles) and nanostructured Cu(110)-(2×1)O with $P = 45$ nm, $\theta_O \approx 0.25$ (green triangles).

mechanisms and therefore a change in the kinetics is to be expected. Apparently, the difference in the kinetics is within the error bars.

4.3 Sulfidation of narrow oxidized stripes

In the beginning, we recall the reaction mechanisms for the sulfidation of clean and oxygen-saturated Cu(110) surfaces, known from the literature and discussed in the section 1.4. The adsorption of H_2S on the clean and oxidized surface will lead in both cases to the same outcome at saturation, the surface will be covered with sulfur in the c(2×2) configuration. On the clean surface, sulfur cannot be observed by STM until saturation coverage is reached, because of its high mobility on copper even at room temperature. H_2S adsorption on an oxygen-saturated surface has been studied by Carley *et al.* [99]. They have observed S-c(2×2) structures appearing on the (2×1)O overlayer even before saturation. In this case, the sulfur is adsorbed on the oxidized copper and is directly immobilized by the surrounding oxygen. Due to the hindered diffusion, the adsorbed sulfur can be imaged by STM already from low concentrations and one can follow growing sulfur islands on the surface. The reaction is initiated at step edges and defects.

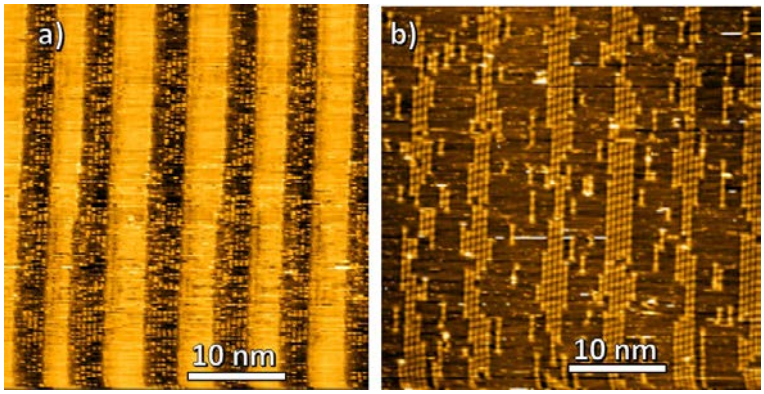

Fig. 4.5: STM images of the sulfidation of narrow CuO stripes. Tunneling parameters: $I = 0.2$ nA, $V = -0.7$ V a) Nanostructure before sulfidation with $P = 7.2 \pm 0.7$ nm and $\theta_O = 0.24 \pm 0.01$. The CuO stripes appear darker (W-tip). b) Same surface after exposure to $\approx$ 100 L H_2S. Short Cu–O chains are cut-off from the edges of the stripes and move freely on the clean copper. Inversed contrast for Cu–O chains in respect to a) caused by ending of the tip by an oxygen atom.

The sulfidation of the partially oxidized nanostructured Cu(110)-(2×1)O surface has been found to follow a different mechanism, depending on the width of the oxidized stripes. We will further discuss the case of the narrow oxidized stripes in this section. If the surface is nanostructured with narrow oxidized stripes (3–10 nm), the reaction has been found to be initiated at the borders of the stripes [89]. Our observations confirm this mechanism. We have observed short Cu–O chains being cut-off from the edges and then move freely on the clean copper stripes. In Fig. 4.5 we can see an example of sulfidation of narrow oxidized stripes. The nanostructure has been prepared by the classical method with approximately half oxygen coverage and periodicity of 7 nanometers. The average width of the oxidized stripes was 3.4 nanometers. STM images of the surface before sulfidation and after the exposure to 100 L H_2S are shown. As previously mentioned, sulfur is highly mobile on clean copper and cannot be imaged by STM until saturation is reached. However, in the presence of oxygen, the diffusion is hindered. In Ref. 89, occasionally small c(2×2) sulfur structures in the proximity of oxidized stripes have been identified. The surface at saturation is covered by the c(2×2) phase of sulfur and with increasing sulfur amount, the higher concentration phase, p(5×2), starts appearing.

4.4 Sulfidation of wide oxidized stripes

Using the new fabrication method for the Cu(110)-(2×1)O nanostructure, we are able to prepare surfaces with significantly wider oxidized stripes, than has been possible by the classical preparation. In the previous work done in our laboratory [89], a new mechanism has been observed during the sulfidation of a nanostructure with wider oxidized stripes. In Fig. 4.6, we can see STM images recorded during sulfidation of a Cu(110)-(2×1)O surface with the periodicity of 70 ± 7 nm. The mechanism is clearly different, than the one seen in Fig. 4.5 for narrow oxidized stripes. Fig. 4.6a) and b) show the surface before and after exposure to 9 L H_2S (measured in the preparation chamber), respectively. The sulfidation leads to a transformation of the oxidized stripes into bright islands. In Fig. 4.6c), we can see a zoomed image of the oxidized stripe after exposure of 6.8 L and in Fig. 4.6d) after 9 L. We can see that the sulfidation proceeds via adsorption of sulfur on the oxidized stripes in c(2×2) configuration, as well as detachment of Cu–O chains from the stripe edges. In this section, we will present the results of the detailed study of this reaction mechanism.

According to our findings, the sulfidation of nanostructures with ω_{CuO} wider than ≈ 10 nanometers (stripes of more than 20 Cu–O chains), will proceed via a combination of the two reaction mechanisms known for the sulfidation of narrow CuO stripes and the oxygen-saturated Cu(110) surface: the Cu–O chain abstraction and S island formation on oxidized copper. For structures with $\omega_{CuO} < 10$ nm, the sulfidation proceeds exclusively via the Cu–O chain abstraction. For structures with $\omega_{CuO} \approx 10$ nm, the chain abstraction is still the main mechanism of the sulfidation, but a few small sulfur islands start appearing on the oxidized stripes. As ω_{CuO} gets larger, the S island formation becomes more important and more favored over the chain abstraction. Structures with $\omega_{CuO} \approx 17$ nm are already large enough, for the S island formation to almost completely take over. In order to confidently conclude that there is no more difference between the S island formation on structures with oxidized stripes larger than ≈ 17 nm, we would need to compare the S island formation for the exactly same exposures, which as has been discussed in section 4.1 is not straightforward in our experiments. We can however compare the role of Cu–O chain abstraction. In all of our experiments for $\omega_{CuO} > 17$ nm, we see the same kind of attack on the borders of the CuO stripes. Even after a significant part of the CuO stripes is covered by S islands, we can still see the original CuO stripe edges, with only some parts of chains missing. In all the cases studied in the present study the main reaction mechanism has been the S island formation and only negligible amount of sulfur has been adsorbed on the CuO stripe edges. Therefore, for our

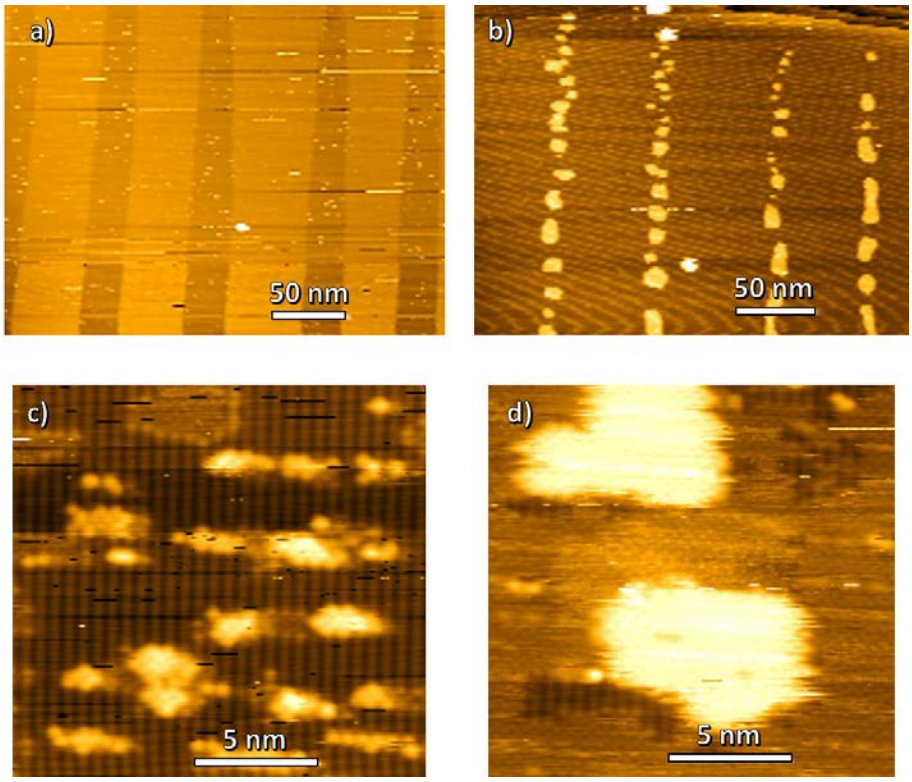

Fig. 4.6: STM images of the sulfidation of wide CuO stripes. Tunneling parameters: a) $I = 0.2$ nA, $V = -0.7$ V; b)–d) $I = 0.2$ nA, $V = -1.0$ V. W-tip. a) Nanostructure before sulfidation with $P = 70 \pm 7$ nm and $\theta_O = 0.20 \pm 0.01$. b) Same surface after exposure to ≈ 9 L H_2S. CuO stripes have been transformed into bright islands. c) CuO stripe during sulfidation (6.8 L). Sulfur forms c(2×2) structures on the CuO stripes. d) CuO stripe during further sulfidation (9 L). S structures grow to form sulfur islands, which are surrounded by rests of the Cu–O chains.

further evaluation, we have considered the S island formation mechanism to be the same for all studied surfaces.

For the present study of the sulfidation mechanism of wide oxidized stripes, we have prepared several Cu(110)-(2×1)O nanostructures with ω_{CuO} in the range between 17 and 32 nm and approximately half oxygen coverage. We have chosen to systematically study surfaces with the same θ_O, in order to be able to compare the results and study exclusively the influence of the width of the stripes without the influence of the changing oxygen coverage. The study has been done by exposing the nanostructure to H_2S during STM measurement in order to follow the reaction mechanism in real time and at the atomic level. The results of the detailed study of the S island formation mechanism, from the initial stages to saturation, are presented next.

4.4.1 Initial stages of the sulfidation

On STM images with atomic resolution recorded during the sulfidation of wide CuO stripes, as shown for example in Fig. 4.7, we can see that sulfur is adsorbing in the c(2×2) configuration on the CuO stripes. The c(2×2) phase is known for sulfur adsorption on Cu(110) (see section 1.4). As we know, the Cu chains in the CuO stripes are reconstructed into (2×1). After the oxygen is removed during the reaction, the Cu adatoms have to rearrange to form the original (1×1) configuration, otherwise sulfur would not be able to adsorb in c(2×2). Fig. 4.7 shows STM images with atomic resolution, where we can distinguish S-c(2×2) structures built on the Cu adatoms of the previously reconstructed surface, and also c(2×2) structures which are in-plane, built on clean copper after the Cu adatoms have been removed. In the images, the "in-plane" structures are highlighted by an ellipse and the "on-top" by a rectangle. In Fig. 4.7a), we see that the c(2×2) structures appear in STM images with a different contrast as a function of their height. The height difference of one monoatomic copper layer between the two structures is better visible in the 3D view image (Fig. 4.7b)).

In Fig. 4.8, the arrangement of atoms of the three phases present on wide CuO stripes during sulfidation are shown. Firstly, there is the (2×1)O-phase of the oxidized copper stripes. During the reaction, the oxygen desorbs in form of H_2O molecules and the Cu adatoms form the Cu(1×1) adlayer, where sulfur adsorbs in c(2×2), forming the "on-top" S phase. Finally, an area of the original CuO stripes is freed from the oxygen and Cu adatoms, leaving the third phase, Cu(1×1), where sulfur adsorbs also in c(2×2). This sulfur phase is therefore one copper monolayer

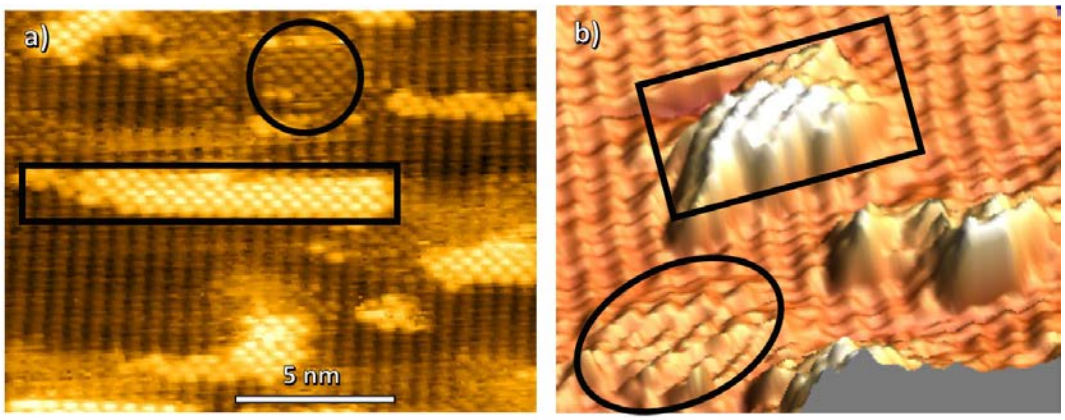

Fig. 4.7: STM images of "in-plane" and "on-top" S-c(2×2) on wide oxidized copper stripes. a) Top view STM image. b) 3D view STM image. In both images the sulfur island on top of Cu adatoms is marked by a rectangle and the "in-plane" island by an ellipse. Tunneling parameters: a) $I = 0.5$ nA, $V = 0.5$ V and b) $I = 0.5$ nA, $V = -0.5$ V.

lower than the sulfur adsorbed on the Cu adlayer. The phase is imaged in-plane with the clean Cu phase in STM images and has consequently lower contrast than the sulfur on Cu adatoms.

Fig. 4.9 shows STM images and corresponding profiles of "in-plane" and "on-top" c(2×2) structures. From the profiles we extract a height difference of 123 ± 10 pm between the "in-plane" and "on-top" sulfur island. This corresponds to the theoretical height of a monoatomic copper step, which is 128 pm. In the following part, we will discuss only the S-c(2×2) islands built on top of the Cu adatoms, which are the easiest to study by STM, because of their good contrast.

At the beginning of the sulfidation we see small structures of a few atoms in c(2×2) configuration appearing on the CuO stripes. At this stage of the reaction we can already observe some attack on the borders of the stripes. With increasing exposure the structures grow in size, while there is less and less oxygen surrounding them. To present the development of the size of the sulfur islands, we give their area as a function of the sulfur coverage. We cannot give the size of the islands as a function of the exposure, because of the discrepancies explained in section 4.1 of the present chapter and therefore the reaction advancement is described in terms of sulfur coverage. We will give the sulfur coverage as a percentage of the original oxidized stripe area which is covered by the "on-top" sulfur islands.

The increase of the island's sizes with respect to the sulfur coverage is summarized in the table 4.2 and the corresponding STM images and histograms of the island's

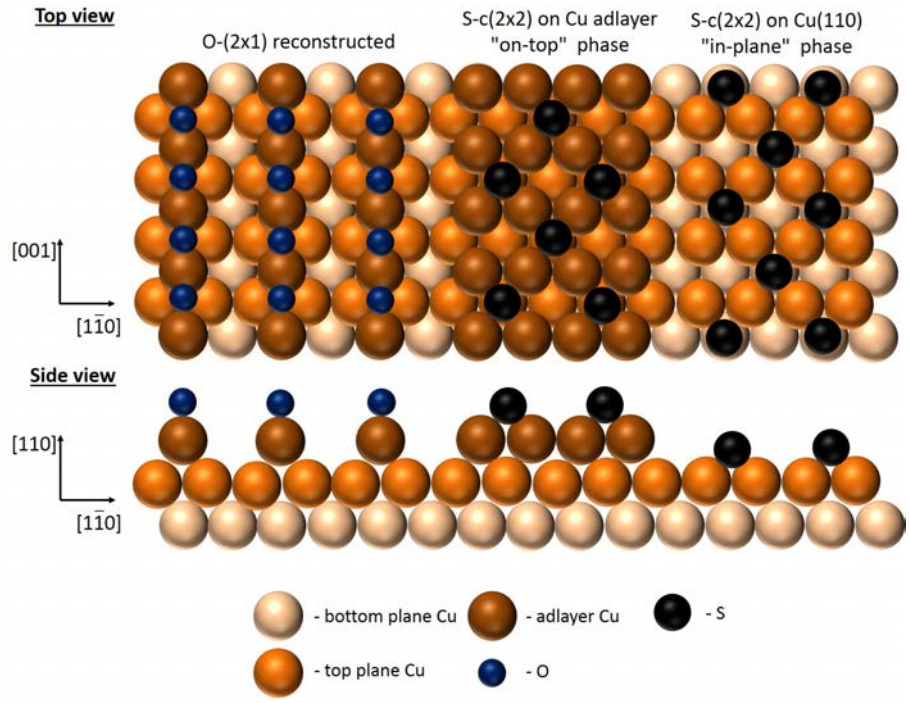

Fig. 4.8: Atomic ball model for (2×1)O and S on Cu(1×1) "on-top" and "in-plane".

sizes are shown in Fig. 4.10 and 4.11. Additionally to the S island size, we have also analyzed their density. Structures composed of sulfur atoms in a c(2×2) formation with the size of 1 to 3.5 nm^2 start appearing on the oxidized stripes when sulfur covers approximately 9% of the CuO stripe. We observe an increase of the density of these structures with further sulfidation from 0.04 to 0.13 islands per nm^2, until the sulfur coverage of around 14%, with their size staying approximately the same. With higher exposure the S islands grow larger and the merging of small sulfur structures into larger islands is characterized by the decrease in the density of the islands. In Fig. 4.10e) islands of up to 45 nm^2 can be found and the S coverage has been determined to be around 27 %. The density of the sulfur islands is significantly lower, namely 0.01 island per nm^2. At this coverage we still observe rests of (2×1)O structures surrounding the sulfur islands, but the borders of the original oxidized stripes are no more visible. In the final stage of the sulfidation, when all the oxygen has been removed by the reaction, the measured island sizes are between 14 and 260 nm^2. The sulfur coverage at this stage has been estimated to be ≈ 45–50 %. This is in agreement with the fact that the density of the Cu adatoms in the (2×1) reconstruction is half of the density of clean copper Cu(1×1), which is, as we have seen in the model in Fig. 4.8, also the density of Cu adatoms in the sulfur islands.

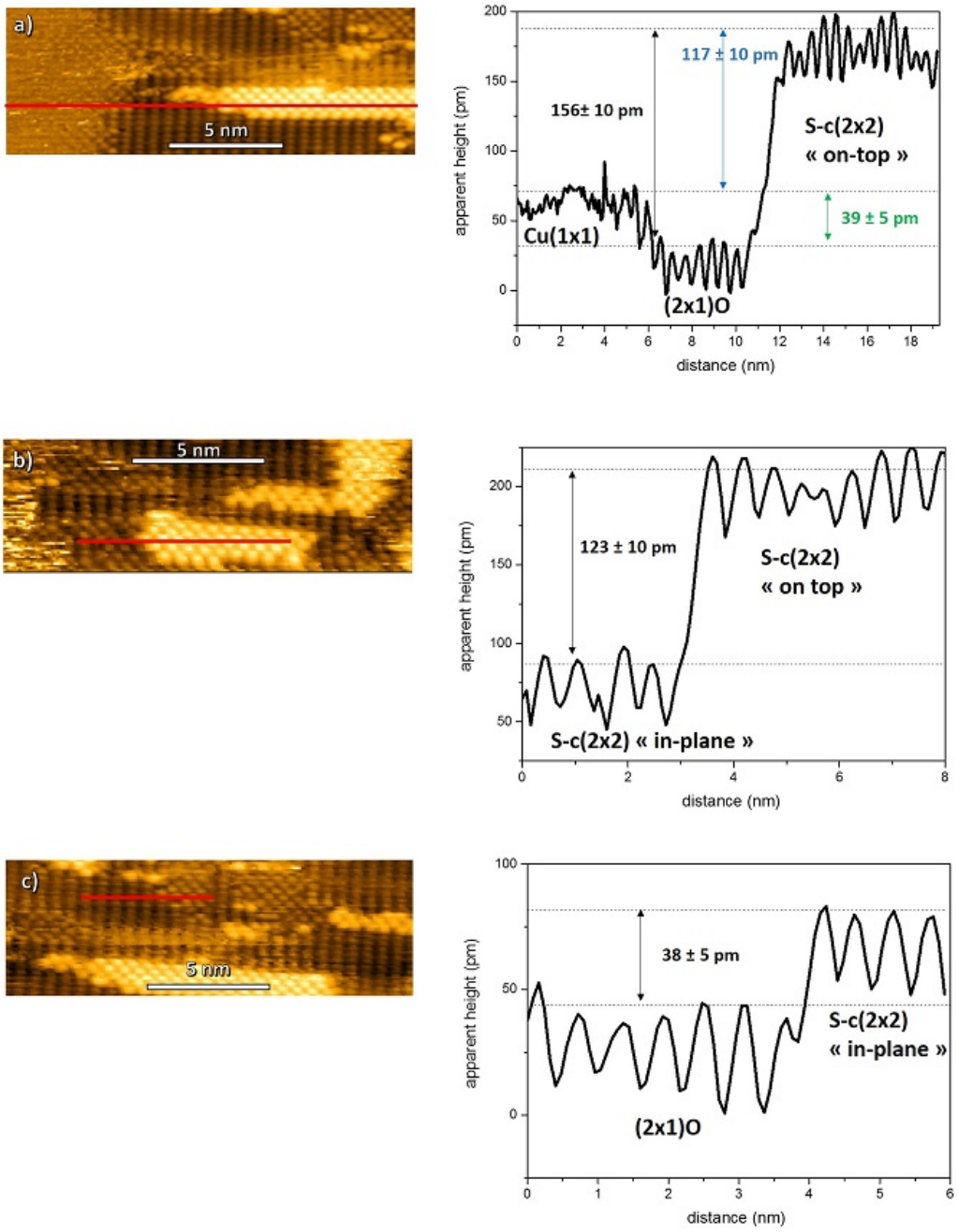

Fig. 4.9: STM images and corresponding height profiles of the 4 different phases present during sulfidation of Cu(110)-(2×1)O with wide stripes. The red lines in the images indicate where the profile has been measured. Tunneling parameters for all images: $I = 0.5$ nA, $V = 0.5$ V. a) Height difference between Cu(1×1) substrate, the reconstructed CuO phase and the "on-top" S island; b) height difference between the S islands "on-top" and "in-plane"; c) Height difference between CuO and "in-plane" S island.

Table 4.2: Size and density of sulfur structures as a function of θ_S

S on CuO stripe %	S island size (nm^2)			S island density (island×nm^{-2})	Fig. 4.10
	min	max	median		
9 ± 1	0.8	3.4	2.1	0.04	a)
14±2	0.6	2.6	1.7	0.13	b)
15±2	1.8	20.9	6.7	0.02	c)
17±2	1.7	12.1	5.1	0.06	d)
27±5	6.9	45.0	18.7	0.01	e)
45±5	14.1	258.6	49.3	0.008	f)

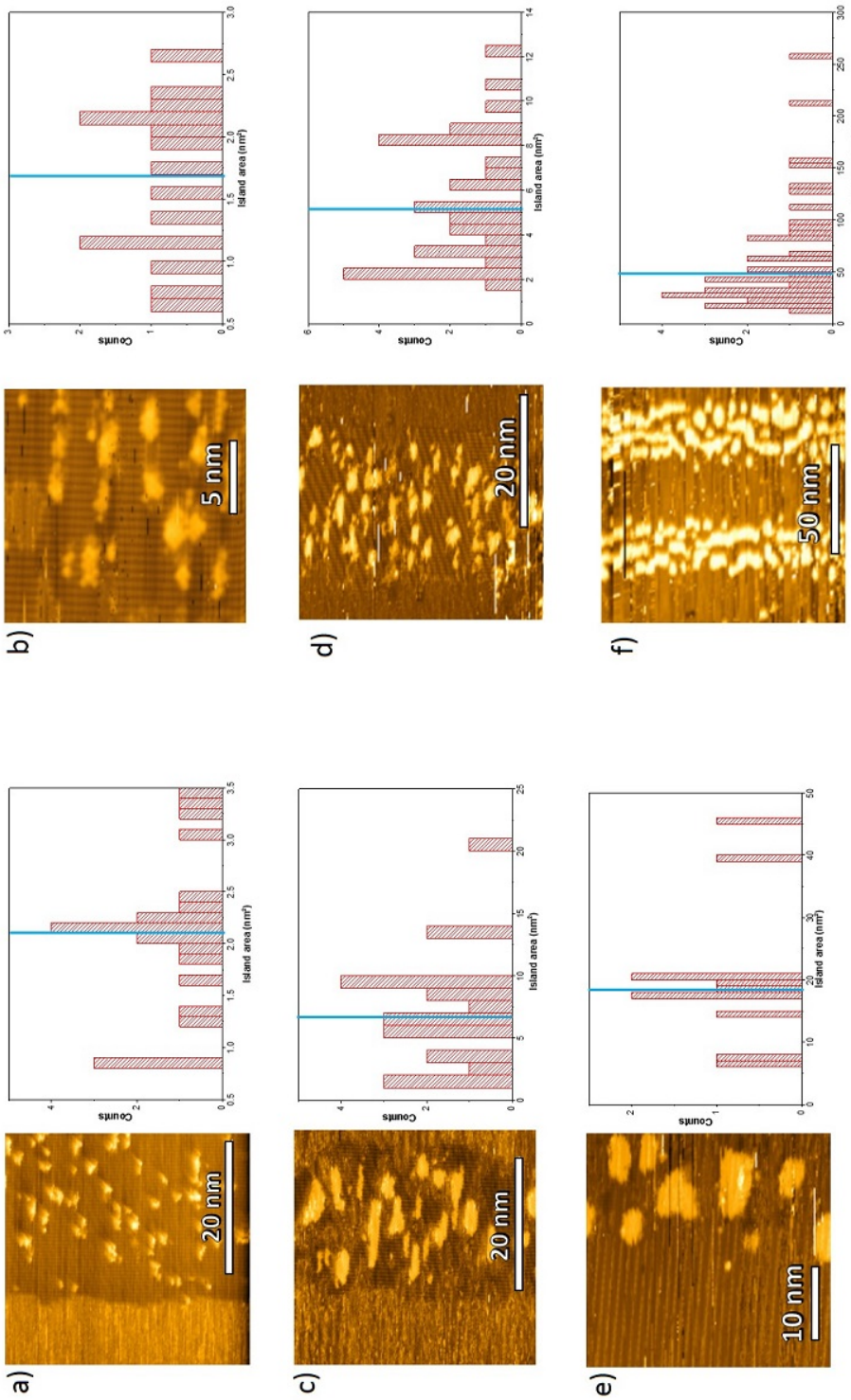

Fig. 4.10: S islands size distributions and corresponding STM images. Sulfur coverage given as percentage of the CuO stripe covered by S: a) $\approx 9\%$; b) $\approx 14\%$; c) $\approx 15\%$; d) $\approx 17\%$; e) $\approx 27\%$; f) $\approx 45\%$. The blue line indicates the median size of the S islands. Tunneling parameters: a) and d) $I = 0.2$ nA, $V = -1.5$ V; b) and e) $I = 0.2$ nA, $V = -1.0$ V; c) $I = 0.5$ nA, $V = 0.5$ V; f) $I = 0.2$ nA, $V = 1.0$ V.

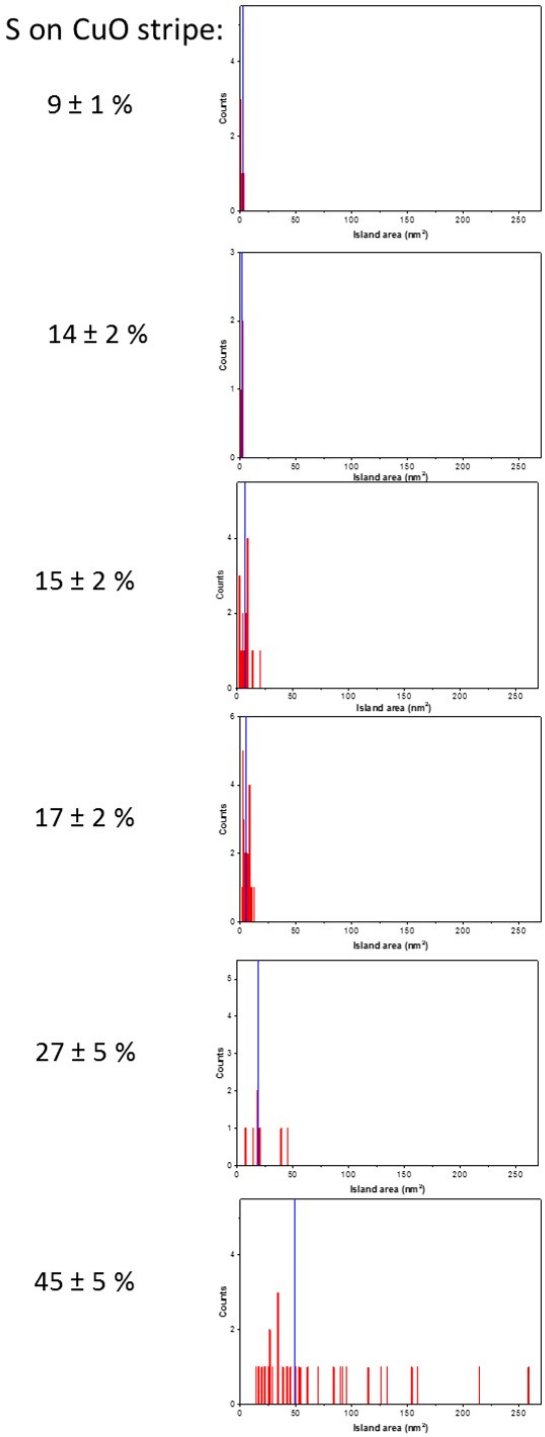

Fig. 4.11: S islands size distributions for different sulfur coverages. The histograms from Fig. 4.10 are shown with the same scale for direct comparison. The blue line indicates the median size of the S islands.

In Fig. 4.12 an STM image is shown, in which we can see a surface after all of the oxygen has been removed by the sulfidation. The surface is covered by the S-c(2×2)

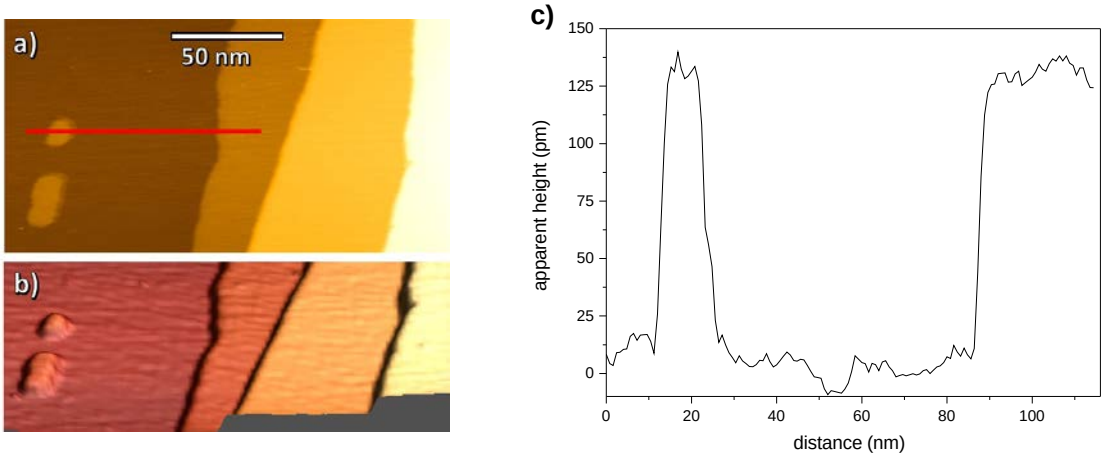

Fig. 4.12: Height comparison between S-c(2×2) island and a monoatomic step. a) STM image of the sulfur islands next to a monoatomic copper step. Tunneling parameters: $I = 0.2$ nA, $V = -1.0$ V. b) The same STM image in 3D view. c) STM height profile measurement. The profile corresponds to the red line in the image. The height of the S-island and the monoatomic step is determined to be 130 ± 10 pm after calibration.

islands. We have compared the height of the S "on-top" island and of a monoatomic copper step. The height profile measurement shows that their height is about the same, which is in agreement with the previously discussed model, where the sulfur islands are one copper monolayer higher than the surrounding surface.

4.4.2 Influence of the exposure conditions on the mechanism

In this section we present the observations made on the reaction mechanism for exposures at different pressures. As discussed in the previous sections, the reaction mechanism for wide oxidized stripes is a combination of Cu–O chain detachment and S-c(2×2) island formation on the CuO stripes. The following results indicate that exposure at high pressures leads to exclusively the sulfur island formation and a low pressure exposure favors the Cu–O chain detachment.

4.4.2.1 Exposure at high pressures

Under the term "exposure at high pressure" we mean an exposure to high enough H_2S pressure to almost saturate a previously nanostructured Cu(110)-(2×1)O surface with sulfur in only a few minutes. The result of a sulfidation experiment with "high pressure exposure" is shown in Fig. 4.13. We have prepared a nanostructure with wide oxidized stripes ($\omega_{CuO} = 32 \pm 3$ nm) using the S co-adsorption method

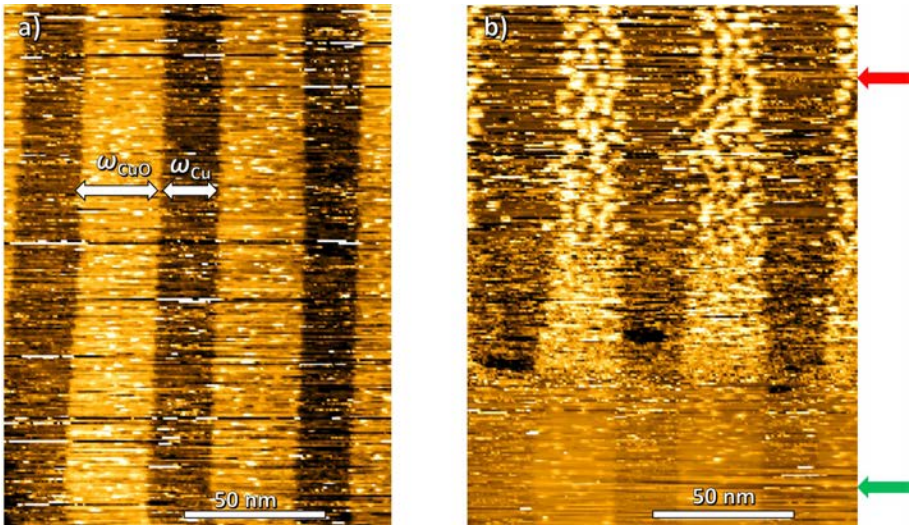

Fig. 4.13: Reaction mechanism during exposure at high pressure. a) STM image of the nanostructure with parameters $P = 55 \pm 5$ nm, $\omega_{CuO} = 32 \pm 3$ nm and $\theta_O = 0.29 \pm 0.01$, before sulfidation. CuO stripes appear brighter, because of O-tip. b) STM image during the sulfidation (same area as in a)). The start and end of the exposure is illustrated by the green and red arrows respectively. The transformation of the oxidized stripes into sulfur islands is shown within one STM image. Tunneling parameters: $I = 0.2$ nA, $V = 1.0$ V.

and exposed it to $\approx 1 \times 10^{-7}$ mbar (measured in the preparation chamber) H_2S during an STM measurement. In the STM image in Fig. 4.13b) we can see, how the oxidized stripes transform into S-c(2×2) islands within a single STM image, which corresponds to less than 3 minutes. The beginning of the reaction can easily be identified, since the opening of the leak valve has caused vibrations in the STM image and is indicated in the STM image by the green arrow. We observe a very fast formation of sulfur islands on the area of the previously oxidized stripes. We cannot observe detached Cu–O chains in this image, since as a consequence of the fast reaction progress, the main reaction mechanism here was the island formation. We deliberately use the term fast reaction progress and not fast reaction, because the pressure doesn't influence the reaction kinetics, but the reaction simply proceeds faster because more H_2S is being deposited. In other words, when exposing to high pressures, the sulfidation until all oxygen is removed, proceeds in a short time. The edges of the stripes, which are more reactive, can get saturated by sulfur and since there is no time for the Cu–O chains to diffuse away from the step edges, the further sulfidation has to proceed by a different mechanism. Therefore in this case, the observed reaction mechanism is almost exclusively the S island formation on the Cu adatoms of the oxidized stripes. To support the statement that during a reaction

Fig. 4.14: Reaction mechanism during exposure at high pressure. STM image of a nanostructure with parameters $P = 100 \pm 27$ nm and $\theta_O = 0.26 \pm 0.01$ during sulfidation. Rests of Cu–O chains are visible as dark patches. No Cu–O chains are diffusing on the clean copper stripe. Tunneling parameters: $I = 0.5$ nA, $V = -0.5$ V.

with a fast progress, the chain detachment mechanism is not present, a less noisy STM image is shown in Fig. 4.14. It shows a nanostructure with wide oxidized stripes ($\omega_{CuO} = 53 \pm 13$ nm) during a sulfidation at high pressure. At this stage of the reaction, the oxidized stripe is covered by bright S islands and only few dark patches of CuO are visible. There are clearly no Cu–O chains on the clean copper stripe.

4.4.2.2 Exposure at low pressures

In this part, we have chosen a different approach and exposed the Cu(110)-(2×1)O nanostructured surface with wide CuO stripes to low H_2S pressure (1×10^{-8} mbar at the maximum). The exposure has been done stepwise with long pauses (≈ 1 hour) between individual steps. During the interruption of exposure, the chamber has been pumped and the surface has been studied under UHV conditions. The surface has been exposed to H_2S 8 times in total. Under these conditions, we have observed only small changes due to sulfidation from image to image and the transformation from an oxidized nanostructured surface to a sulfur-saturated surface took several hours. In Fig. 4.15a) we can see an STM image of the prepared nanostructured surface before the sulfidation. The nanostructure prepared by the S co-adsorption method had the parameters $P = 35.5 \pm 4$ nm and $\theta_O = 0.23 \pm 0.01$. After 1 min of exposure at 1×10^{-8} mbar and 7.5 min at 5×10^{-9} mbar H_2S (pressure measured in the preparation chamber), we start to observe small sulfur structures on the CuO stripes (see Fig. 4.15b)). In the STM images in Fig. 4.15c) and d), we can see closely the Cu stripes at this stage of the reaction. The borders of the oxidized stripes are attacked and we can see short Cu–O chains moving freely on the clean copper stripe. These images were recorded about 1 hour and 30 minutes after exposure. This shows

that when exposing to low pressures, the reaction proceeds slowly, favoring thus the Cu–O chain detachment mechanism.

We have continued to expose the nanostructure and after additional stepwise exposure to a total of 9 min at 1×10^{-8} mbar and 40 min at 5×10^{-9} mbar H_2S, we have observed the formation of bright islands on the clean copper stripes, as shown in Fig. 4.16a). At the moment when these islands start appearing, oxygen is still present on the surface. In Fig. 4.16b) an STM image of the oxidized stripe existing next to the new islands on clean copper is shown. At this point, only about half of the oxygen of the oxidized stripes has been removed by sulfur. We can see a significant attack on the borders of the CuO stripe.

In Fig. 4.17a) and b) STM images of the final stage of the sulfidation are shown. Additional exposure to H_2S for 2 min at 1×10^{-8} mbar leads to the removal of all of the remaining oxygen from the oxidized stripes and their transformation into S-c(2×2) islands. To identify the nature of the islands built on the clean Cu stripes, we compare their height with the height of the S-c(2×2) "on-top" islands created from the CuO stripes in the STM profile in Fig. 4.17c). We can see that both islands have the same height, which corresponds to the height of a monoatomic step of copper, namely 120 ± 10 pm. We therefore conclude that the large bright islands, built on clean copper stripes during exposure at low rates, are also S-c(2×2) islands on a Cu adlayer.

We will now briefly discuss the new mechanism. The source of the adatoms for these new S islands could be the CuO stripes or step edges. The border of the oxidized stripe is attacked by the reaction with sulfur and we can see Cu–O chains missing from the stripes. These short Cu–O chains are mobile on clean copper [67], as we can see in Fig. 4.15b) and c), and they are surrounded by adsorbed sulfur. During sulfidation, the chains progressively disappear from the STM images, as oxygen is removed by the reaction. The Cu–O chains are the probable source of the Cu adlayer, since we observe neither an attack of the step edges, nor a formation of monoatomic holes on the terraces. The mechanism of the formation of S-c(2×2) islands on clean copper stripes, from the sulfur from H_2S and the Cu adatoms coming from the oxidized stripes, requires time for diffusion of atoms on the surface. If the sulfidation until almost saturation S coverage proceeds in only a few minutes, there is no time for this process and therefore no islands are built on clean copper stripes.

Additionally, we can discuss the amount of sulfur adsorbed on the clean Cu stripes. In Fig. 4.16 the sulfur structures formed on the CuO stripes are composed of around 50–100 atoms (largest area measured 14 nm^2). Meanwhile the S-c(2×2)

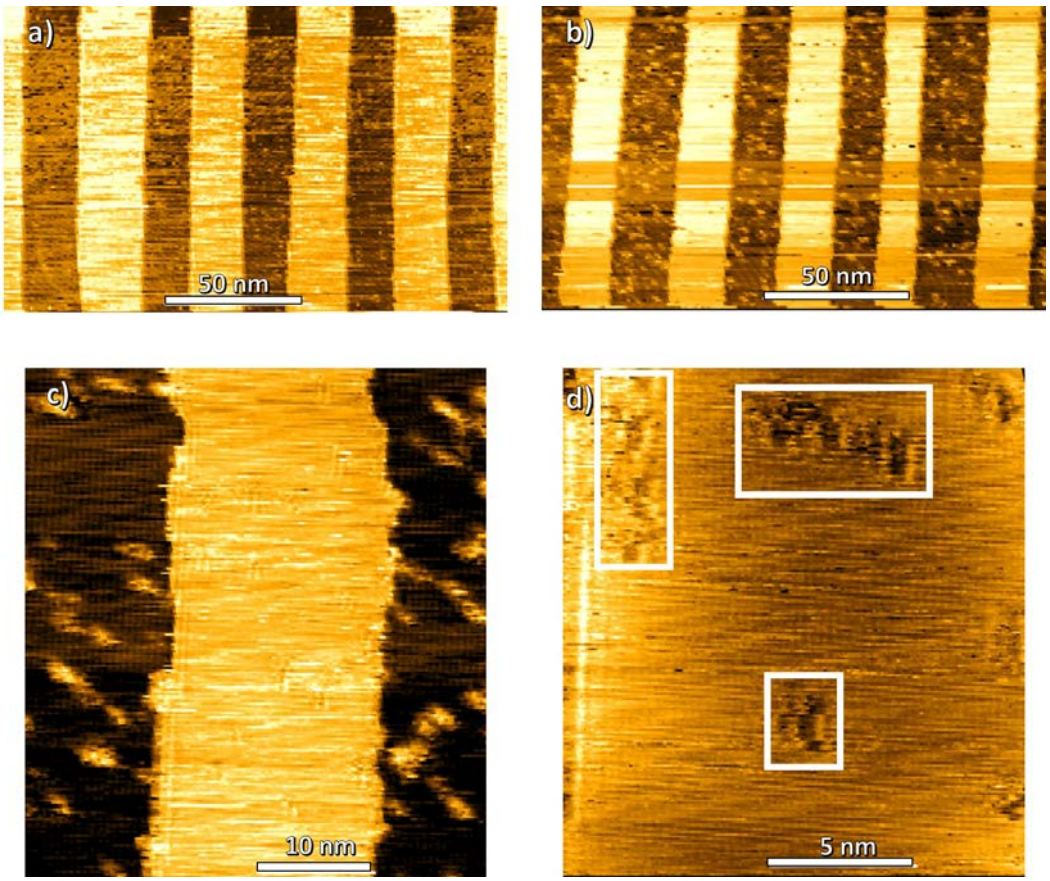

Fig. 4.15: Low pressure exposure: beginning of reaction. a) STM image of the nanostructure before the sulfidation. $P = 35.5 \pm 4$ nm, $\omega_{\mathrm{CuO}} = 16.5 \pm 2$ nm, $\theta_{\mathrm{O}} = 0.23 \pm 0.01$. b) STM image of the same surface at the beginning of sulfidation. Small sulfur structures begin to appear on the CuO stripes. c) and d) STM images showing the attack of the CuO stripe borders and short detached Cu–O chains (highlighted by a white rectangle) moving on the clean copper stripe. W-tip in all images. CuO stripes appear darker. Tunneling parameters: a) $I = 0.2$ nA, $V = -1.5$ V; b) $I = 0.5$ nA, $V = -0.5$ V; c) $I = 0.2$ nA, $V = -0.7$ V; d) $I = 0.5$ nA, $V = -0.7$ V.

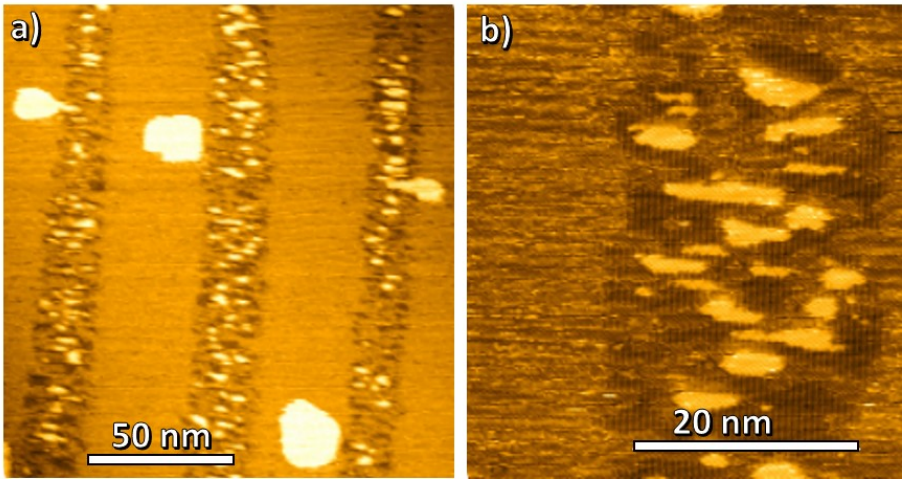

Fig. 4.16: Low pressure exposure: S islands on Cu stripes. a) STM image of S-c(2×2) islands on clean copper stripes. Tunneling parameters: $I = 0.2$ nA, $V = -1.5$ V. b) STM image showing the oxidized copper stripe at the moment, when S islands start to appear on copper stripes. W-tip, CuO stripes appear darker. Tunneling parameters: $I = 0.5$ nA, $V = 0.5$ V.

islands on clean copper stripes have in average the area of 300 nm^2. Islands of this size were found after a high pressure exposure to H_2S only after a phase of coalescing of small islands. The diffusion of islands at this stage of the sulfidation is possibly easier on the clean copper stripes, because they are not hindered by surrounding Cu–O chains, like the sulfur structures built on the CuO stripes. We can draw the conclusion that the average size of the sulfur islands found on copper stripes is larger than the ones on oxidized stripes, but if we compare the surface density of these islands, we realize that the islands on copper stripes cover smaller percentage of the surface and therefore globally more sulfur is adsorbed on the CuO stripes than on the clean copper stripes (when comparing only the "on-top" sulfur). On the oxidized stripe in Fig. 4.16b) approximately 12% of the area originally covered by CuO is now covered by the S-c(2×2) islands. This corresponds to ≈ 6% of the whole surface in the image. The islands on copper stripes in Fig. 4.16a) cover 4.5% of the Cu stripes and 3% of all the surface imaged.

Apart from the sulfur islands being formed on the clean copper stripes, we have observed mass transport of copper atoms towards the step edges. The steps that are almost parallel to the $[1\bar{1}0]$ direction, which are straight before the reaction, become wavy during the slow sulfidation. The Cu adatoms, which diffuse to the step edges are incorporated at the end of the terrace. When the neighboring terrace is still covered by the oxidized stripes, the Cu will be incorporated only at the end of

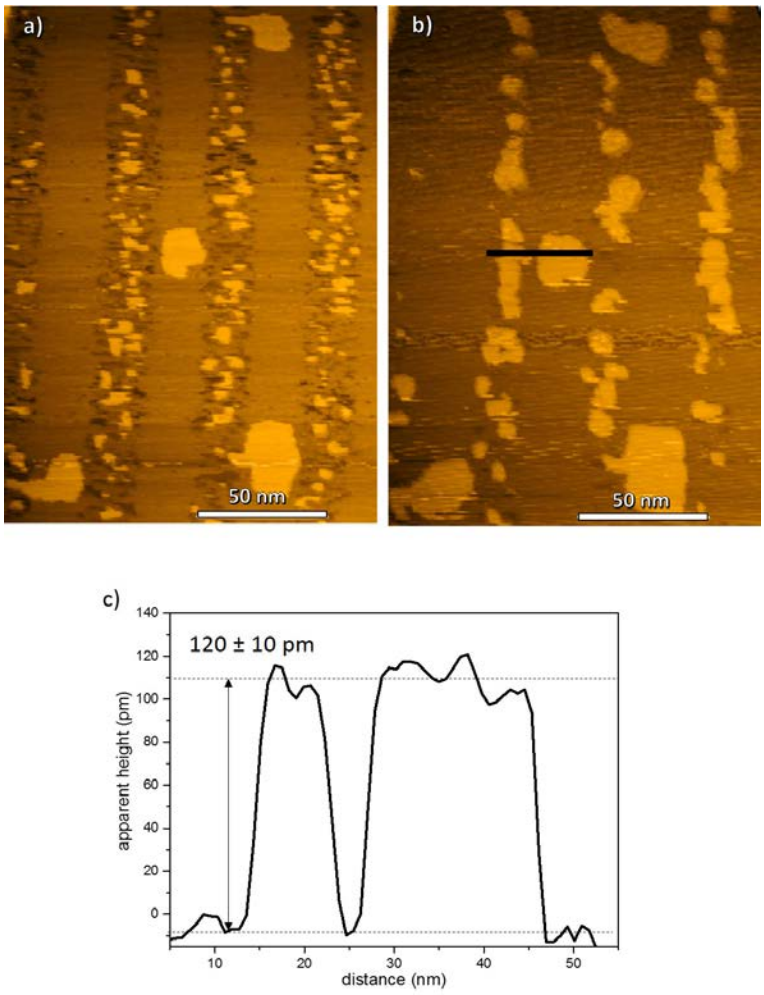

Fig. 4.17: Low pressure exposure: final reaction stage. a) STM image of the nanostructured surface during sulfidation with slow progress. CuO stripes are covered with sulfur structures and their borders are attacked (visible Cu–O chain detachment). Large sulfur islands appear on clean copper stripes. b) STM image of the same surface after additional exposure to 1×10^{-8} mbar H_2S for 2 minutes and 22 minutes of scanning after the exposure. The remaining oxygen is removed by the sulfidation and now only sulfur islands can be found on the surface. c) STM height profile corresponding to the black line in b). The height of sulfur islands built on Cu and on CuO stripes is compared with the conclusion that their height is the same, 120 ± 10 pm. Tunneling parameters: a) $I = 0.2$ nA, $V = -1.5$ V; b) $I = 0.2$ nA, $V = -0.7$ V.

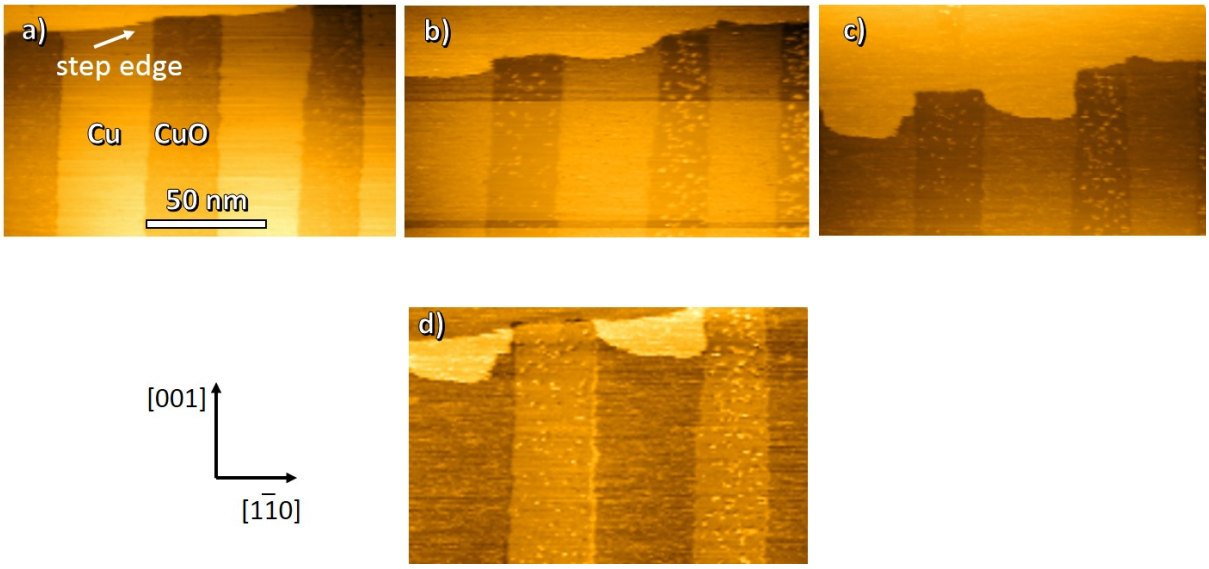

Fig. 4.18: Modifications at step edges during sulfidation. a)-c) STM images showing a growing step edge during sulfidation. d) Subtraction of the STM images c) – a). Before the subtraction the images have been shifted so that the same area on the surface is exactly superposed in both images. Tunneling parameters: a)-b) $I = 0.2$ nA, $V = -1.5$ V; c) $I = 0.5$ nA, $V = -0.5$ V. W-tip in all images.

the clean copper stripes and not the oxidized stripes, since these sites are already occupied by oxygen. The source of the Cu atoms could be the reconstructed (2×1)O phase, where Cu adatoms are present. As we know, during the sulfidation, oxygen is removed from the oxidized stripes, leaving behind Cu adatoms. Additionally, short Cu–O chains are being removed from the borders of the CuO stripes and these then freely move on the clean copper stripe. Further sulfidation will lead to removal of the oxygen from these Cu–O chains, setting thus Cu adatoms free.

Fig. 4.18 shows an example of such a growth of a step edge. In the present case about 60 minutes passed between each image during which the nanostructure has been under constant pressure of $\approx 5 \times 10^{-8}$ mbar H_2S (measured in the preparation chamber). The time necessary for the modification of step edges indicates that the diffusion process to the step edges is relatively slow. To better analyze and visualize the area by which the terrace grows in two hours, we have subtracted the first image from the last one, as shown in Fig. 4.18d). After the subtraction the part of the terrace that has not been in the first image appears brighter. This area is around 400–600 nm^2 per copper stripe, whose area is at least 6500 nm^2. (The exact area of the copper stripe cannot be measured, since the end of the terrace lies outside of the image. If we consider that typically a terrace is not wider than $\approx$ 450 nm in the

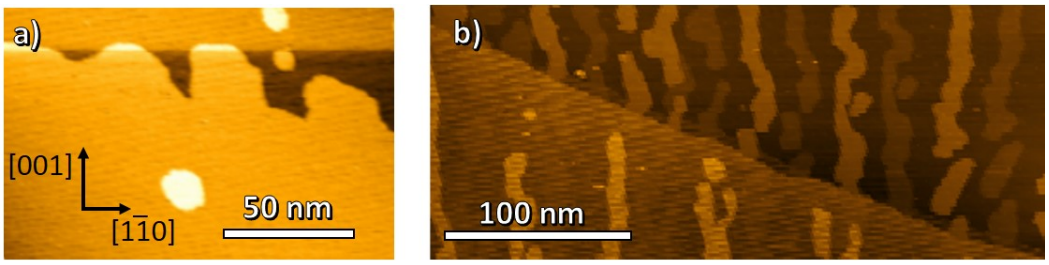

Fig. 4.19: Comparison of the modification to step edges for exposures at low and high pressures. a) STM image showing a modified step edge after a sulfidation until saturation with a slow progress. b) STM image of a step edge after sulfidation until saturation with a fast progress. S islands are imaged twice on the bottom terrace because of the effect of a double STM tip. Tunneling parameters: a) $I = 0.2$ nA, $V = -1.5$ V; b) $I = 0.2$ nA, $V = 1.0$ V

[001] direction, the maximum area of the CuO stripe would be ≈ 12600 nm^2.) In Fig. 4.18 we can see that the modification to step edges by sulfidation is already visible, while the oxidized stripes of the nanostructure still stay more or less intact and only a few small sulfur islands can be seen on the stripes (S on CuO stripes ≈ 9 %).

In Fig. 4.19 two step edges after sulfidation are shown (both almost parallel to the [1$\bar{1}$0] direction). Both surfaces are covered with sulfur and all the oxygen has been removed. In Fig. 4.19a) the sulfidation has been done stepwise, with long pauses between individual exposures and at low pressure, while in Fig. 4.19b) the sulfidation until almost saturation took only about 3 minutes. In both cases two terraces are divided by a single monoatomic step and both terraces have been covered by the CuO stripes before the sulfidation. We can clearly see that when the sulfidation progress is fast, the modification to the step edge is not as pronounced, as for the case of an exposure at low pressures (slow reaction progress). This is because the oxygen is removed before the Cu adatoms have time to diffuse to the step edges. Additionally, we have identified the detached Cu–O chains as the source of the Cu atoms which modify the step edge. During sulfidation at high pressure, the S island formation mechanism is favored over the chain detachment, as discussed in section 4.4.2, and therefore there is less Cu atoms which diffuse to the step edges and more which are incorporated into the S "on-top" islands.

Steps which are parallel to the [001] direction are also parallel to the CuO stripes and therefore we will not observe the same kind of wavy structures due to blocking of sites by oxygen like we have in Fig. 4.18. The Cu adatoms which are incorporated into these steps will be distributed uniformly along the whole length of the step.

4.5 Summary and discussion

In this chapter, we have presented results regarding the reactivity of the Cu(110)-(2×1)O surface towards sulfur. We have exposed nanostructures with wide and narrow CuO stripes and approximately the same oxygen coverage ($\theta_O \approx 0.25$) to H_2S during STM measurement. Our results demonstrate that the mechanism of the sulfidation is significantly different depending on the width of the CuO stripes. For nanostructures with $\omega_{CuO} < 10$ nm, the sulfidation proceeds exclusively via Cu–O chain detachment. The stripes are attacked during the reaction preferentially from the borders. The short Cu–O chains, which have been cut-off from the borders, diffuse freely on the clean copper stripe surface. For nanostructures with wider stripes, we have observed a new mechanism. The Cu–O chain detachment is still present, but we additionally observe the formation of sulfur islands on the CuO stripes. This mechanism is known for the sulfidation of an oxygen-saturated Cu(110) surface. The reason why we do not observe such island formation on narrow CuO stripes probably lies in the different strain of this surface, in comparison to a nanostructure with wide oxidized stripes. The elastic strain of the surface results in the periodic structure formation. Apparently, the strain in the surface which leads to the formation of wide stripes also enables the formation of S islands on the oxidized stripes and makes the stripes less stable against attack by sulfur.

Furthermore, we have studied the formation of the sulfur islands on CuO stripes in detail. The mechanism of the reaction is as follows. Adsorption of sulfur causes the removal of the oxygen atoms from the (2×1)O phase. The released Cu adatoms from this phase move together to form a Cu(1×1) adlayer onto which simultaneously sulfur adsorbs in c(2×2). The sulfur will at the same time adsorb on the clean copper. Sulfur atoms on the clean copper stripes are however highly mobile and therefore not visible by STM. The sulfur which adsorbs in c(2×2) on the copper, which has been released from the (2×1)O phase is immobilized by the surrounding oxygen and therefore recognizable in STM images. These “in-plane” sulfur islands are one copper monolayer lower, than the islands built on the Cu(1×1) adlayer of the (2×1)O phase and appear therefore with a lower contrast in STM images.

Our experimental results further indicate that the mechanism of the sulfidation is influenced by the exposure conditions. We have observed that an exposure at high pressures leads to a sulfidation exclusively via the S island formation. When exposing to high pressures, the reaction progress is fast and therefore the detached Cu–O fragments do not have time to diffuse away from the stripe edges. The reaction thus

has to continue by the second mechanism, the S island formation on the oxidized stripes.

In contrary, at low pressures, the Cu–O chain detachment mechanism is favored. During a sulfidation with a slow progress, we have observed a formation of large sulfur islands on a Cu(1×1) adlayer not only on the oxidized stripes, but also on the clean copper stripes. The source of the adatoms is the Cu–O chains, detached from the oxidized stripes and diffusing on the clean copper stripe. Additionally, we have observed Cu atoms being incorporated into step edges during the low pressure sulfidation. When a step edge parallel to the $[1\bar{1}0]$ direction (perpendicular to the CuO stripes) is next to a terrace covered by the CuO stripes, the Cu adatoms can only be incorporated into the free sites, and not the sites occupied by oxygen. This leads to a non-uniform growing of the terrace and forming of a wave-shaped step edge.

In summary, we can say that fast reaction progress causes the adsorption to be determined by kinetics, while during slowly progressing reactions, the adsorbed species have time to diffuse and reach a minimum energy configuration. While the S island formation mechanism may require more energy, it is favored by the high pressure, simply because there is no time for the diffusion of the Cu–O chains.

Chapter 5

Dynamics of the S-c(2×2) islands

In this chapter, we report on the stability of the islands, formed by sulfidation of a nanostructure with wide oxidized stripes, under UHV conditions. In the first part of this chapter, we shortly discuss certain experimental and theoretical studies of cluster diffusion on surfaces, in order to subsequently explain our results. We further present our experimental observations of the surface diffusion for two cases: sub-saturation and saturation sulfur coverages.

Since the techniques that allow us to follow atomic mobility on surfaces (e.g. field ion microscopy (FIM), electron microscopy, STM) have been developed, many studies were dedicated to the atomic diffusion on metal surfaces [167, 168]. Different mechanisms, such as hopping, jumping, atomic exchange or tunneling have been identified. Large clusters of 20 or more atoms were believed to be immobile, until Fink in 1984 using the FIM technique showed the mobility of large clusters of Pd atoms on W(110) [169]. The investigation of the mobility of large clusters on metal surfaces is important, because their diffusivity influences the stability of nanostructures, as well as kinetics and morphology of thin film growth.

We will first remind some terms and phenomena, known from the literature, that we will need in the discussion about surface diffusion of 2D islands. During epitaxial thin film growth, islands are formed, which are often not in equilibrium and therefore they undergo coarsening [170], i.e. an increase in the length-scale of the growth features, in order to minimize their total free energy. This can proceed either via Ostwald ripening, where large islands grow at the expense of small ones [126, 127, 131], or via coalescence of diffusing adatom islands, called Smoluchowski ripening [171–173]. The type of ripening depends less on the material, but more on the face and type of the island. For example, Smoluchowski ripening has been observed for adatom

islands on Ag(100) [172] and vacancy islands on Ag(111) [173]. In contrast, adatom islands on Ag(111) [174], adatom and vacancy islands on Ag(110) [175, 176], and vacancy islands on Ag(100) [172] coarsen primarily via Ostwald ripening.

The motion of large clusters, required for coalescence, can proceed by single atom jumps or concerted atom displacement. The main mechanisms in the single atom jumps category are peripheral displacements, correlated evaporation and condensation, and the true evaporation and condensation (EC) mechanism. During the correlated EC mechanism, cluster atoms are detached, diffuse on the surface and then come back to reattach to the same cluster. The EC mechanism is essentially the same, except a different atom attaches to the cluster after the evaporation. For this mechanism the presence of adatoms on the surface is necessary. Both EC mechanisms are unlikely at low temperatures because of the high energy required for detachment.

Various studies have been dedicated to the diffusion of large clusters on fcc (100) [135, 172, 177–180] and (111) [136, 166, 181–183] surfaces. In general, they found the mobility of large clusters to be due to edge running, and they found the evaporation and condensation mechanism to be unlikely, but possible in special cases. Gliding of stable clusters was observed on fcc (111) surfaces, but not on (100) surfaces. On the other hand, information about diffusion of large clusters on anisotropic surfaces, such as fcc(110), is not exhaustive. Experimental studies have been performed on Ag(110) [175, 176, 184], Au(110) [185] and Pt(110)-(1×2) [186]. Morgenstern *et al.* have studied the diffusion of a vacancy island on the channeled Ag(110) island and found the diffusion to be a Brownian motion in the in-channel direction. In the cross-channel direction the diffusion has been found to be very limited and linearly dependent on the ratio of the hopping/exchange probabilities. According to our knowledge, the only experimental study of diffusion of larger structures on Cu(110) has been done by Schunack *et al.*, who studied the diffusion of large organic molecules [187]. They have found their diffusion to be along the $[1\bar{1}0]$ direction.

5.1 Behavior of S islands at sub-saturation sulfur coverages

The sulfidation of the nanostructured Cu(110)-(2×1)O surface leads to creation of islands composed of Cu adatoms on which sulfur is adsorbed in a c(2×2) configuration, on the (110) face of copper. Once the nucleation phase is finished, and all the oxygen is removed from the surface, the dynamic island evolution (coarsening and decay) has been studied by STM. Since we are using the "on-site on-time" approach, we can follow

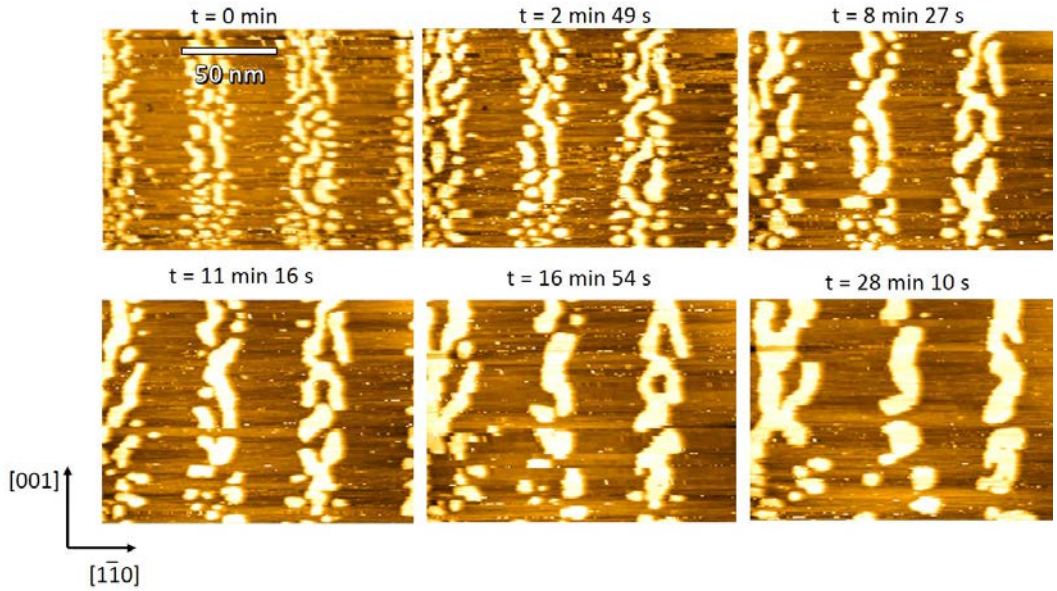

Fig. 5.1: Coarsening of S-c(2×2) islands: STM images of the surface after exposure to H_2S until sub-saturation S coverage. The time at the top of each image is the moment when the image started. The STM image is scanned from bottom to top and it takes 2 min 49 s to scan the image area. Time t = 0 is the end of exposure to H_2S. We observe coalescence of neighboring islands as well as Ostwald ripening, leading to dissolution of small islands and growth of larger ones. Tunneling parameters: I = 0.2 nA, V = 1.0 V.

continuously the dynamic surface diffusion of the islands. In this section, we will present experimental observations of the behavior of these islands at sub-saturation sulfur coverages and we will discuss the observed coarsening mechanisms.

The experiment has been carried out as follows. We have prepared a nanostructure with the parameters $P = 55 \pm 5$ nm and $\theta_O = 0.29 \pm 0.01$ by the S co-adsorption method. We have exposed the nanostructure to H_2S and stopped the reaction when all of the oxygen has been removed from the surface and the surface was about 90% saturated by sulfur, as determined by AES. At this point, we can see bright islands of sulfur on Cu adatoms, whose surface area corresponds to approximately half of the surface area of the initial oxidized stripes. Since, according to AES analysis, the surface is nearly saturated by sulfur, we know that the bright islands in STM images are in fact surrounded by sulfur and not clean copper. Sulfur is highly mobile on copper and cannot be imaged by STM when its coverage is lower than saturation. At saturation coverage, the sulfur mobility is hindered and we can image the c(2×2) structure on the surface.

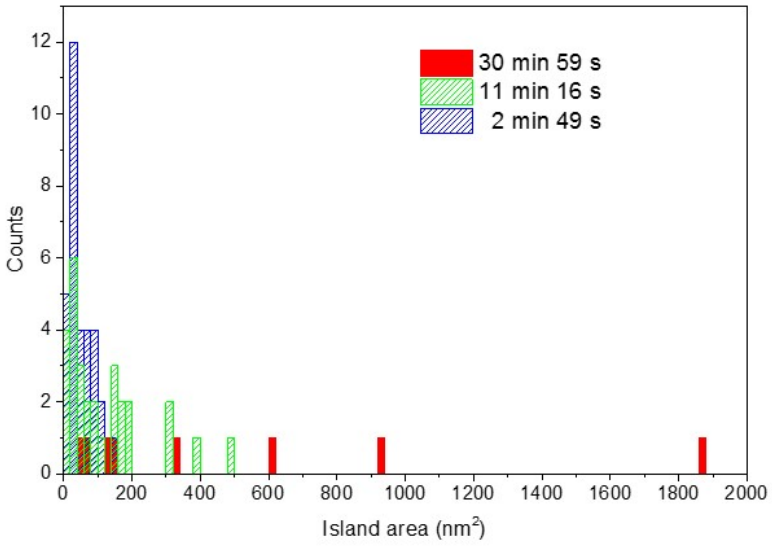

Fig. 5.2: Histogram for S island size at different times after exposure

In Fig. 5.1 we can see the evolution of the sulfur islands during the first half hour after the exposure. Even at room temperature, the islands are mobile on the surface. As discussed earlier, the coarsening on a channeled surface, such as fcc(110), has been found to proceed via Ostwald ripening, as shown on the example of Ag(110) [175, 176]. However, we observe an important coalescence of the small islands into large ones. We also occasionally observe very small islands shrinking until finally disappearing completely, which would indicate the Ostwald ripening mechanism. At the moment when all the islands are formed and all the oxygen is removed, the average island size is between 30 and 80 square nanometers. After 45 minutes, islands with sizes up to 1850 nm^2 have been observed. The distribution of the island sizes at different times after exposure is portrayed as histograms in Fig. 5.2. The density of the islands goes from 6×10^{-3} island per nm^2 (directly after exposure) to 7×10^{-4} island per nm^2 (28 min 10 s after exposure).

In Fig. 5.3 an STM image is shown, where we can see the effect of the scanning on island distribution of the surface. The area of the image in the white square has been scanned by STM for half an hour. The interactions between the STM tip and the sample causes a displacement of the adatoms in the scanning direction. We can see that islands in the scanned zone have diffused in the direction parallel to the original stripes, but also in the direction of the scanning, while on the rest of the surface the islands diffuse significantly less along the $[1\bar{1}0]$ axis. The islands seem to

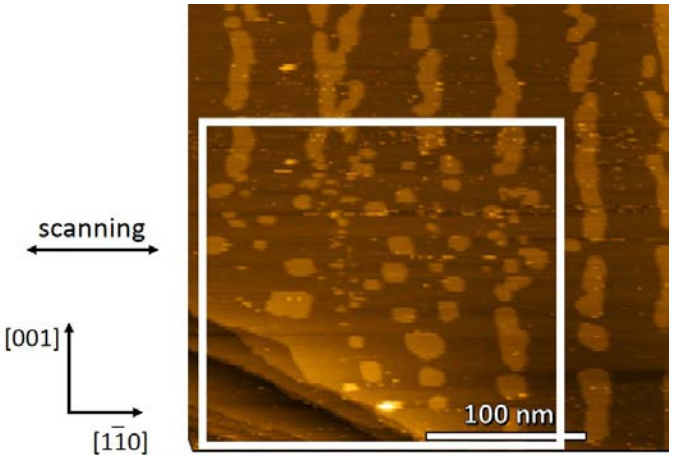

Fig. 5.3: Influence of STM scanning on the movement of sulfur islands. The area of the surface which has been scanned for half an hour is highlighted by the white square. Tunneling parameters: $I = 0.2$ nA, $V = 1.0$ V.

move only to approach the closest islands and coalesce, forming a long island along the [001] direction. An influence of the scanning on the island diffusion has not been observed each time. The extent of the interaction depends on the tip and tunneling conditions.

Now we can discuss the diffusion of the S islands, which are not affected by the scanning. As observed in Fig. 5.3, the island diffusion on the surface does not proceed by a random walk in all directions, but the islands move preferentially towards their nearest neighbor, in order to coalesce. This is due to the fact that forming one large island instead of many small ones, minimizes the total free energy. The individual atoms probably move in all directions, however the center of the mass of the islands moves preferentially along [001], leading to formation of large elongated islands. This is the direction parallel to the stripes of a nanostructured surface, however it is not the direction with the lowest diffusion barrier for single adatoms. The (110) face of copper has a channeled structure and the barrier for diffusion is known to be the lowest along the [1$\bar{1}$0] direction, in-channel with the copper rows [99, 103]. Mechanisms leading to diffusion across the channel are either the cross-channel hopping or the far more favorable exchange mechanism. Islands of adatoms, vacancy pits, as well as heterogeneous clusters formed during epitaxial thin film growth have an equilibrium shape, which is determined by the variation of the step free energy with angle. The step free energy is the energy required to create a crystal step and it is proportional to the chemical potential of the step. Equilibrium shapes of adatom and vacancy islands on (111) and (100) faces of Cu, Ag, and Au

are hexagons and squares, respectively [188]. On the anisotropic Ag(110) surface, the equilibrium shape is elongated along the in-channel direction [175, 176, 184, 188, 189]. The ratio between the width and length is known to depend on the ratio of attempt frequencies for hopping diffusion and exchange diffusion. Ag(110) should be a good model for the Cu(110) surface, since both are stable in their unreconstructed form. Yet, we observe the exact opposite orientation of the elongated islands, which could suggest a high probability of the exchange mechanism in our case. Few experimental, but many theoretical studies determined the energy needed for the in-channel and the cross-channel self-diffusion on Cu(110) [190–204]. The cross-channel hopping mechanism has been found, as expected, to be very unfavorable. Its energy barrier is around 1.07 eV [203]. During the atomic exchange mechanism, an adatom takes the place of a lattice atom at the side of the channel and it is the displaced lattice atom that continues the diffusion [205]. The energetic barriers of this process, in comparison with the in-channel hopping, are given in table 5.1. An experimental observation of a cross-channel diffusion has been reported for the first time for Pt and Ir adatoms on Pt(110) [206] and has since been observed also for other fcc metals. Evidently, the diffusion of clusters and islands composed of hundreds of adatoms of different chemical species is guided by different processes than simple self-diffusion of a single adatom, for which the diffusion is expected only in one direction on an anisotropic surface. A diffusion of adatom islands on a channeled surface across the channels has already been observed by Linderoth *et al.* [186]. They have studied the diffusion of Pt islands on the missing-row reconstructed Pt(110)-(1×2) surface. At low coverages the Pt adatoms move only along one direction, however at higher coverages, the island motion becomes 2D. The authors propose two kinds of mechanisms for mass transport across the missing-row troughs, which both result from the interaction between neighboring islands. Therefore we infer that the here observed coalescence along the cross-channel direction is also guided by the attraction between neighboring islands. But essentially, what allows the creation of elongated islands parallel to the [001] direction in our case, is the fact they the islands have been formed on the oxidized stripes, which act as a template for the sulfur islands. Sulfidation of an oxygen-saturated surface also leads to formation of S-c(2×2) "on-top" islands. In contrary to our case, they will probably be distributed homogeneously over the surface and their coalescence will not lead to formation of long islands along the [001] axis.

In section 1.5 a model for the diffusion of 2D islands, known from the literature, is described. The diffusion coefficient is known to depend on the island side length

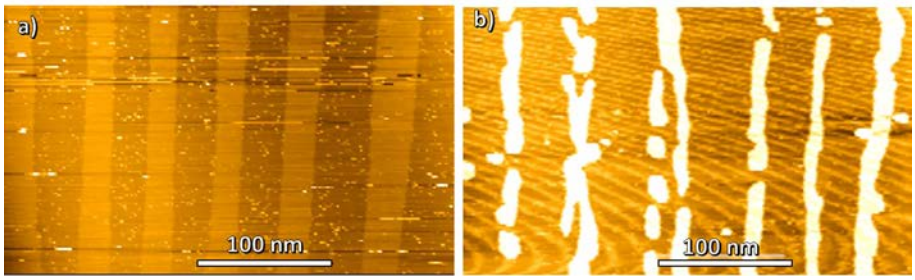

Fig. 5.4: a) STM image of the Cu(110)-(2×1)O with the periodicity $P = 55 \pm 5$ nm. b) STM image of the same surface after sulfidation. (The surface is now covered with S-c(2×2) islands). Tunneling parameters: a) $I = 0.2$ nA, $V = -1.0$ V (W-tip) and b) $I = 0.2$ nA, $V = 1.0$ V.

according to a power law, $D \propto L^{-n}$. To determine the diffusion coefficient, or the exponent, n, which describes the underlying mechanism in our case, we would need to be able to observe an island which is isolated on a terrace. The constant coalescing and shape changing of the islands in our case does not permit an analysis of the movement of the island center. Also, to explain how the islands diffuse along the [001] direction, we would need to perform a simulation. We propose that the reason is linked to the interaction between sulfur and Cu adatoms, which could be stronger in this direction, or to the attraction between the islands. From our study of the surface diffusion of the S islands, we can also note that we have never observed an island crossing over a step edge.

In Fig. 5.4 a comparison of the surface before and after the sulfidation is shown. Before the reaction, the surface has been covered with the Cu(110)-(2×1)O nanostructure with the periodicity of 55 ± 5 nanometers. As a consequence of the S island diffusion along the direction parallel to the stripes, this periodicity has more or less been transferred onto the sulfur islands. Certainly, the stripes in the later case do not have well-defined borders, therefore the periodicity is only approximate. Nevertheless, on the image in Fig.5.4b), the periodicity has been estimated to be 58 ± 11 nanometers. Now we will discuss the question of the stability of such nanostructured S/Cu(110) surfaces.

After all the islands in respective proximity merged together, we have observed pronounced gradual shrinking of the islands, which continued until all the bright islands completely disappeared from the surface. Example of this behavior is shown in the STM images in Fig. 5.5. For evaluation of the island size as a function of time, we have chosen $t = 0$ to be the time when the first image of the sequence has been

Table 5.1: Review of the barrier heights for diffusion of Cu on Cu(110) from the literature. Values for the in-channel hopping mechanism along the [1$\bar{1}$0] direction and the cross-channel exchange mechanism along the [001] direction are given.

	Energetic barrier		
	in-channel hopping (eV)	cross-channel exchange (eV)	Ref.
experimental		0.84	[207]
theoretical	0.059		[190]
	0.23 (AFW) 0.28(VC)	0.30 (AFW) 0.31 (VC)	[192]
	0.18	0.27	[193]
	0.260 (113 atoms) 0.294 (13 atoms)	0.485 (133 atoms) 0.489 (13 atoms)	[194]
	0.292	0.419	[195]
	0.24	0.30	[196]
	0.25	0.30	[197]
	0.23	0.29	[198, 199]
	0.251	0.284	[200]
	0.23	0.30	[201]
	0.23	0.27	[203]

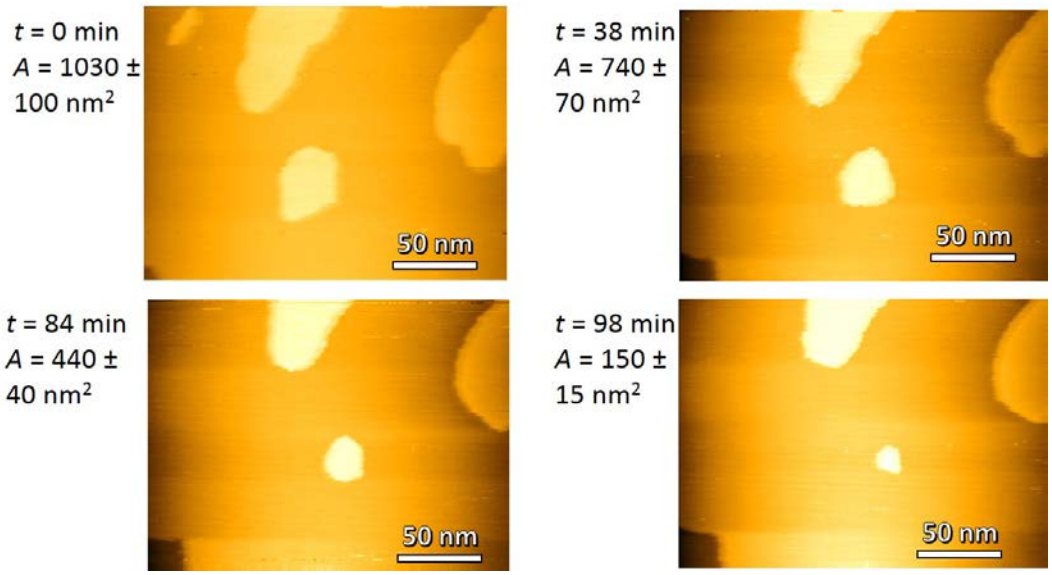

Fig. 5.5: STM images: S island decay. The time t, which has passed since the recording of the first image is given, as well as the area A of the sulfur island in the middle of the image. The first image has been recorded 4 h 40 min after the exposure to H_2S. Tunneling parameters: $I = 0.2$ nA, $V = 0.7$ V.

recorded. This image has been recorded 4 hours and 40 minutes after the exposure to H_2S.

During this decay of the islands, the sulfur signal in the AES spectra stays the same. Evidently, there is no desorption of sulfur, but the shrinking of the islands is due to superficial diffusion of the sulfur atoms, as well as the Cu adatoms away from the islands. A different mechanism than for the coalescence of small islands takes place. During the coalescence, the adatoms "float" on the surface and move to join other islands. But what becomes evident once the islands become larger, is that additionally to the "floating" displacement, adatoms from the periphery of the islands become incorporated into the surrounding overlayer and therefore we lose the contrast caused by the height difference between the sulfur on adatoms and on clean copper. The mechanism involved could be a kind of vacancy diffusion, when the Cu adatoms and the S atoms hop into vacancy sites in the overlayer, which is a nearly sulfur-saturated copper surface. Possibly the same mechanism as during Ostwald ripening is present here, except that this time the evaporated atoms from the smaller islands do not condensate at the borders of larger islands, but instead, they are incorporated into the surrounding surface.

We have noticed that smaller islands were shrinking faster than larger ones. The atoms have to be extracted from the periphery of the island. Such detachment should

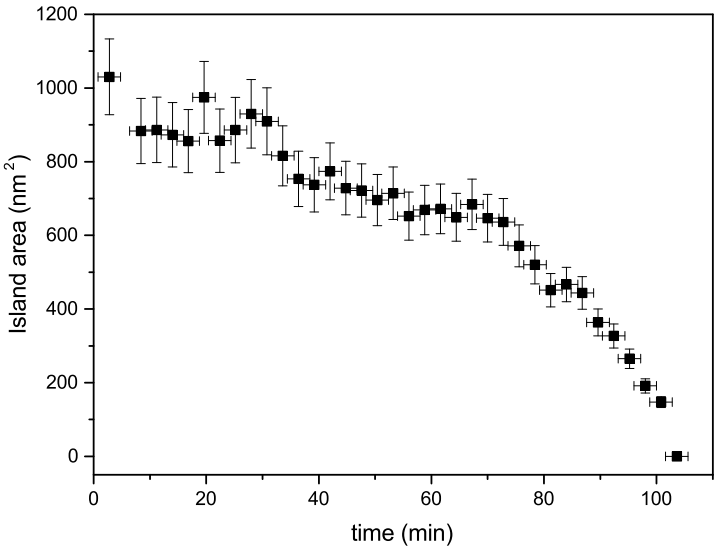

Fig. 5.6: Graph of S island area as a function of time. Time $t = 0$ has been chosen as the time when the first STM image of the sequence has been recorded.

be easier for atoms at the periphery of islands with smaller radius and therefore higher curvature, because these atoms are less coordinated. This explains why smaller islands with circular shape shrink faster. To quantify the decay dynamics, we have analyzed the area of the island in each STM image as a function of time, which is shown in Fig. 5.6. It is apparent that the change in the island area with time, $-\mathrm{d}A/\mathrm{d}t$ is not linear. We see that as the islands get smaller, they shrink faster. For the following calculations, we suppose a circular shape of the islands with a radius r. Because of the apparent dependency of the decay rate on the island radius, we postulate the following power law model:

$$-\frac{\mathrm{d}A}{\mathrm{d}t} = \alpha r^{-\beta} \tag{5.1}$$

We will now try to evaluate the values for the coefficients α and β. The area of the island A is equal to πr^2 for a circular island. After derivation this gives:

$$\mathrm{d}A = 2\pi r \mathrm{d}r \tag{5.2}$$

Therefore we can rewrite equation 5.1 as:

$$-\frac{2\pi r \mathrm{d}r}{\mathrm{d}t} = \alpha r^{-\beta} \tag{5.3}$$

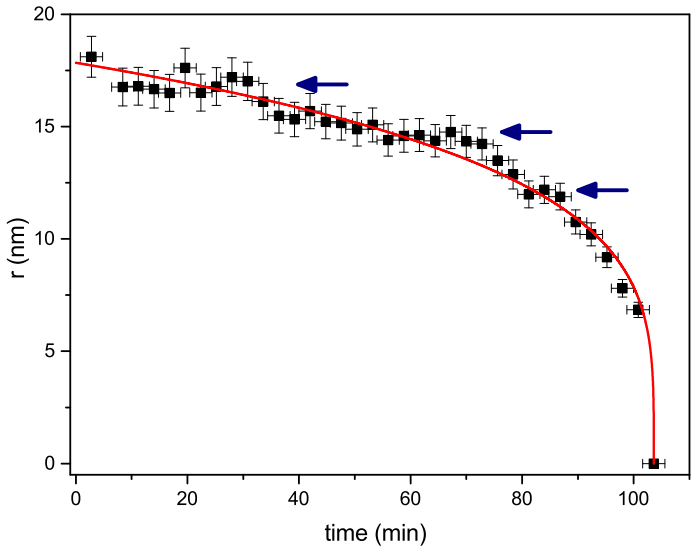

Fig. 5.7: Graph of S island's radius as a function of time. The red line is the fitted model described in the text. The blue arrows indicate the possible saddle points.

After integration over r with limits r and 0 and over t with limits t and t_f , we will obtain for r:

$$r = \left[\frac{\alpha}{2\pi}(t_\mathrm{f} - t)\right]^{\frac{1}{\beta+2}} \tag{5.4}$$

The final time t_f is the experimentally determined time, for which the radius reached zero.

In the graph in Fig. 5.7 we have plotted the radius of the island calculated from the area $\left(r = \sqrt{\frac{A}{\pi}}\right)$ as a function of time. We have fitted the model for the radius on the experimental data and obtained the parameters $\alpha = 8\ 000 \pm 3000$ and $\beta = 2.1 \pm 0.2$, by calculating with time in minutes and radius in nanometers.

Thus we have found a power law for r, $r \propto (t_\mathrm{f} - t)^{0.24}$, with an exponent of $\frac{1}{\beta+2} = 0.24$. In section 1.5, a classical model for the island decay based on the Gibbs-Thomson equation and leading to the same power law, is described. The model predicts an exponent of 1/3 for the diffusion limited decay and 1/2 for interface limited decay. The value we have found is slightly lower than 1/3 and we conclude that our data gives an evidence of the diffusion limited decay. For the interface limitation, an additional barrier for the detachment of atoms from the island needs to be present. Therefore the diffusion limitation is in fact expected for our case. The

determined value of 0.24 is in good agreement with experimental observations on other systems. For example, Morgenstern *et al.* have found an exponent of 0.27 for decay of 2D Ag islands on Ag(111) [208]. The same exponent has been found for the decay of Cu adatom islands on Cu(111) [209]. The decay of vacancy islands has also been studied on the channeled surface of Ag(110) [175]. The authors have found 1D decay mode, contrary to the Ostwald model predictions, to be present at temperatures between 175 and 220 K. This means that the length of the island is decreasing, while the width stays the same. However, at temperatures higher than 220 K, both width and length of the islands decreased with the decay parameter $\approx 1/3$, in agreement with the model for the diffusion limited decay.

When evaluating the agreement of the model with the experimental data in Fig. 5.7, we notice oscillations in the decay, which are not described by the model. The here presented island decay shows signs of stabilization, where the decrease in island area slows down and forms a plateau in the $r(t)$- curve. We can see such saddle points at values of $\approx$ 17, 14 and 12 nm (indicated by the blue arrows). The discrepancies arise because the model considers a constant value for β. The deviations of the decay parameter from the model could be caused by the influence of the location of neighboring islands on the decay rate. For example, a small island surrounded by larger islands that are smaller than average, will decay more slowly than expected by the theory. This influence of the local environment will also cause the size distribution of islands to be broader than simulated, because islands of the same size will not necessarily decay with the same kinetics. Certain island sizes may also be stabilized by strain effects. In the literature, the stabilization of certain island sizes during island decay is known to arise for example due to quantum size effects [210, 211]. Quantum size effects occur when a size of a structure is in the dimensions of de Broglie wavelength of electrons confined within it. On the decaying island, surface states electrons are confined in the lateral direction, which is responsible for the enhancement of the detachment barrier for adatoms from the island edge. This occurs for specific island sizes and shapes, which exhibit an absence of quantum well states near the Fermi level. This experimental observation could demonstrate that the electron confinement influences the surface kinetics and therefore the value for β is not constant, but oscillates as a function of the island's size. A deviation of the model is also certainly due to the circular shape approximation. In Fig. 5.8 we show an example of the island shape, which evolves during the decay. While at some moments, the shape is practically circular, we also often observe the formation of sharp edges. This could indicate that the detachment of adatoms from the periphery

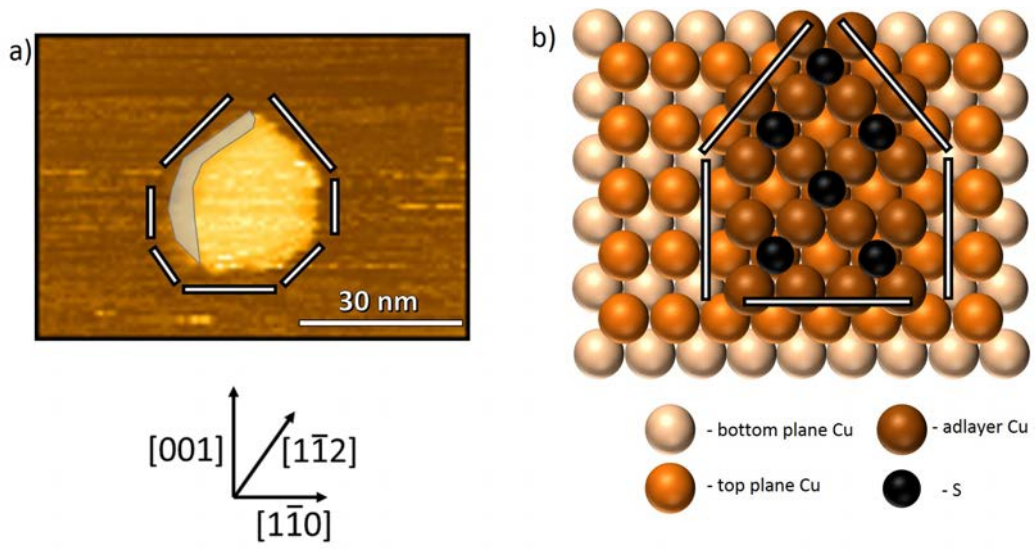

Fig. 5.8: a) STM image of a specific island shape formed during decay. The effect of the double tip is visible at island edges. The phantom side of the island is highlighted by gray shadowing. This effect, increasing the uncertainty of the island area determination, has been taken into account. b) Atomic ball model representing a S-c(2×2) "on-top" island on Cu(110). The atomic model serves only to point out directions and is not an actual size model of the island in the STM image. In the example shown here, the borders of the island have edges with specific orientations. In the atomic ball model, we can see that these orientations correspond to the direction formed by S atoms in the c(2×2) configuration, namely the $\langle 1\bar{1}2\rangle$, $\langle 1\bar{1}0\rangle$ and $\langle 001\rangle$.

is not isotropic, but specific orientations are preferred. The orientations of the island sides in the STM image shown in Fig. 5.8, correspond to orientations in which sulfur positions, in the c(2×2) configuration, are dense. They are the $\langle 1\bar{1}2\rangle$, $\langle 1\bar{1}0\rangle$ and $\langle 001\rangle$ directions. We can assume that a dense coordination of atoms on the island is more advantageous, because the high coordination of atoms increases stability of the island. This would again lead to a deviation from the model, which supposes an isotropic decay of a circular island.

After 24 hours following the end of exposure to H_2S, all of the islands have disappeared. However, we could very occasionally find islands, which seem to have stopped diffusing and their size stays constant even after more than 24 hours. In Fig. 5.9 two STM images of such islands are shown. We assume that the specific elongated form of these islands indicates the presence of strongly bound surface contaminations (or defects) at the sharp corners, which hinder the diffusion of the atoms from the periphery of the islands. The island stays in a shape with high radius

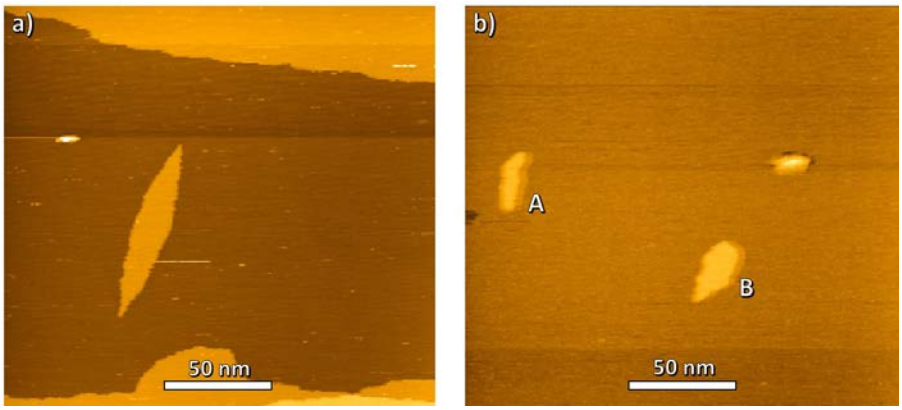

Fig. 5.9: STM images of S islands pinned by contaminations. Islands of a specific form stay on the surface even after 24 hours. In image b) two sulfur islands are shown and marked A and B. The third bright feature is identified as a large contamination, because it is significantly higher than the other two islands. Tunneling parameters: a) $I = 0.2$ nA, $V = 1.5$ V, b) $I = 0.2$ nA, $V = 1.0$ V.

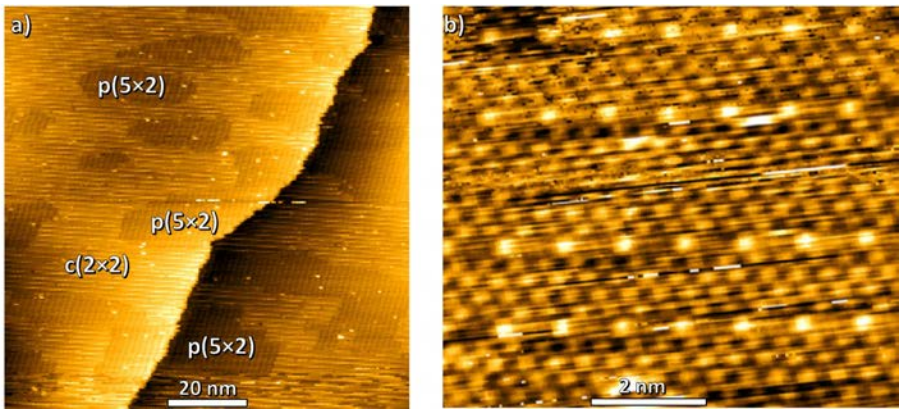

Fig. 5.10: a) STM image showing the co-existence of S phases c(2×2) and p(5×2). b) STM image of the S-c(2×2) phase with atomic resolution. Unusual bright features separated from each other by ≈ 10 Å, corresponding to the features reported by Ref. 99 for sulfidation of an oxidized Cu(110). Tunneling parameters: a) and b) $I = 0.2$ nA, $V = 1.0$ V.

of curvature and therefore the diffusion from its periphery will be extremely slow. It comes to a kind of "pinning down" of these sulfur islands.

Finally, after the bright S-c(2×2) islands disappeared, we have exposed the surface to additional H_2S. Already after short exposure at 8×10^{-8} mbar ($\approx$ 30 L), we could observe the surface being covered by both the c(2×2) and the p(5×2) phase, as shown in Fig. 5.10. The co-existence of these phases is known for $0.41 < \theta_S < 0.62$.

5.2 Behavior of S islands on a sulfur-saturated surface

We have seen that after sulfidation of the nanostructured Cu(110)-(2×1)O surface until all oxygen is removed, the surface will be covered with S islands, which eventually decay. The S on Cu adatoms incorporate into the vacancies of the surrounding sulfur overlayer. In order to answer the question of how such S islands behave if the surrounding copper is already saturated with sulfur, we have performed the following experiment. A nanostructure with $P = 100 \pm 27$ nm, $\omega_{CuO} = 53 \pm 13$ nm and $\theta_O \approx 0.26$ was prepared and subsequently exposed to H_2S until we were sure that the saturation coverage had been reached. We have not been able to obtain atomic resolution on the surface and therefore could not verify the presence of the saturated c(2×2) structure or the second phase, p(5×2). However, we have exposed to 180 ± 10 L H_2S, while after already 50 L all the oxygen had been removed from the surface. Furthermore the sulfur amount was determined by AES after the exposure and it was found to be 30 % higher than for a fully covered c(2×2) phase. This means that both the c(2×2) and p(5×2) phases were present on the surface. After exposure to H_2S, we have evacuated the chamber and scanned the surface for several hours under UHV conditions. We could conclude that the islands are still mobile and undergo coarsening. We observed both dynamic coalescence and Ostwald ripening mechanisms. However, the islands do not disappear from the STM images even after long diffusion times. In fact, even after 22.5 hours, the surface is still covered by large S islands, as seen in Fig. 5.11. This is because the sulfur cannot incorporate into the already saturated sulfur overlayer. The formation of higher concentration sulfur phases, such as p(5×2) or p(3×2), would require more energy for the necessary compression.

In Fig. 5.12 we can see the evolution of the S islands during 5 hours following the exposure to saturation. S islands surrounded by the saturated sulfur overlayer are still mobile and move together to form larger islands. In table 5.2 a summary of the S

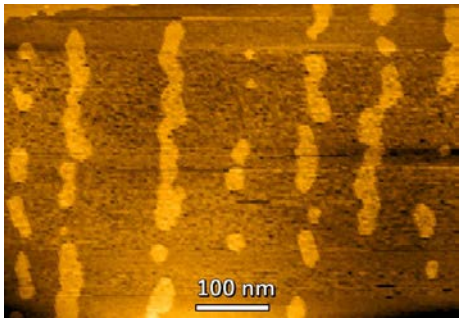

Fig. 5.11: STM image of the surface 22.5 hours after exposure to saturation. The surface is still covered with large S islands, which do not disappear. Tunneling parameters: $I = 0.2$ nA, $V = -1.5$ V.

island parameters at different times after exposure is given. The coverage and density is here given with respect to the whole surface and not the area of CuO stripes, and therefore are not to be compared with the values in table 4.2. The coalescence is confirmed by the increase of the median size of the S islands and decrease in density. Even after 5 hours the S island cover the same percentage of the surface, within the uncertainty, as in the beginning. This confirms that the Cu adatoms and S atoms in the islands are "frozen" on the surface and do not incorporate into the layer around them. This finding also indicates that the diffusion of the atoms from the periphery of the sulfur islands is dependent on the sulfur coverage of the surrounding surface. So the constant β in the model 5.4 is dependent on θ_S.

In Fig. 5.13, we show some examples of island coarsening that we have observed during the experiment. The image sequences in Fig. 5.13a) and b) show two islands colliding together and forming a larger one. This process is the already mentioned dynamic coalescence, also called Smoluchowski ripening. It requires a mobility of the merging islands. We can observe how the islands first approach, then connect by a small "neck", which eventually becomes thicker, as the island rearranges to an energetically more favorable shape. According to literature [188], during a coalescence event the neck is formed and widens within seconds, and the remaining bumps on both sides of the neck retreat within minutes. Our scanning is not fast enough to quantify the time of individual steps during the coalescence process.

In Fig. 5.13c) we can also see two islands colliding and their shape becoming rounder, but we can also see an example of the Ostwald ripening mechanism. The small island on the bottom of the image does not collide with the larger one, but it dissolves, while the larger one grows. This mechanism is explained by the fact that small islands have a larger vapor pressure, a consequence of the Gibbs-Thomson

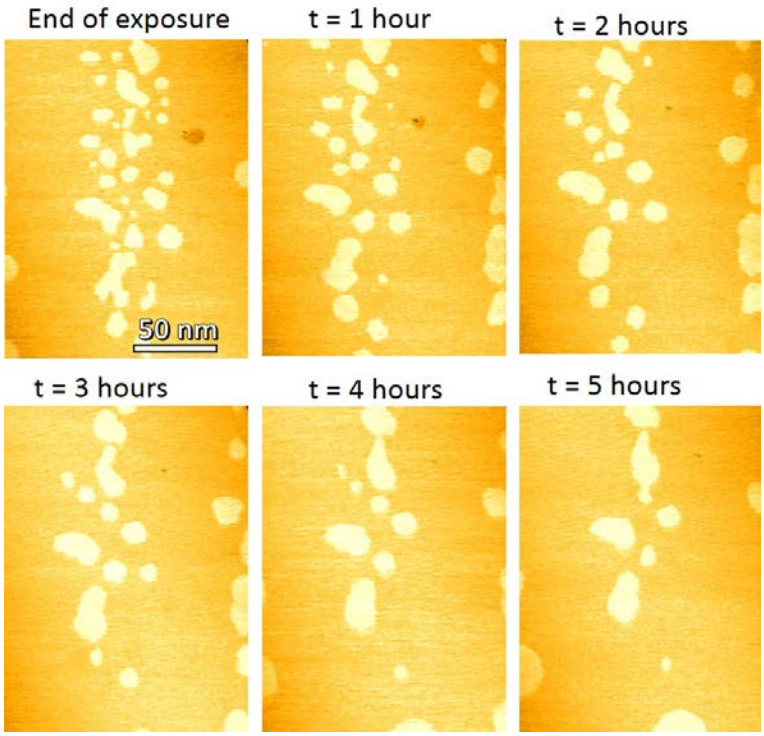

Fig. 5.12: STM images of S islands after exposure to saturation. The same area of the surface has been scanned for over 5 hours. Tunneling parameters: $I = 0.5$ nA, $V = -0.5$ V.

Table 5.2: S island size evolution after exposure to saturation

Time since exposure (hours)	S island size (nm^2)			S island density (island$\times nm^{-2}$)	S island area (%)
	min	max	median		
0	19	413	123	1.0×10^{-3}	17 ± 3
1	37	447	124	9.8×10^{-4}	16 ± 3
2	24	451	138	9.0×10^{-4}	15±3
3	39	493	181	7.5×10^{-4}	15±3
4	25	495	249	5.8×10^{-4}	16±3
5	54	1181	246	4.5×10^{-4}	16±3

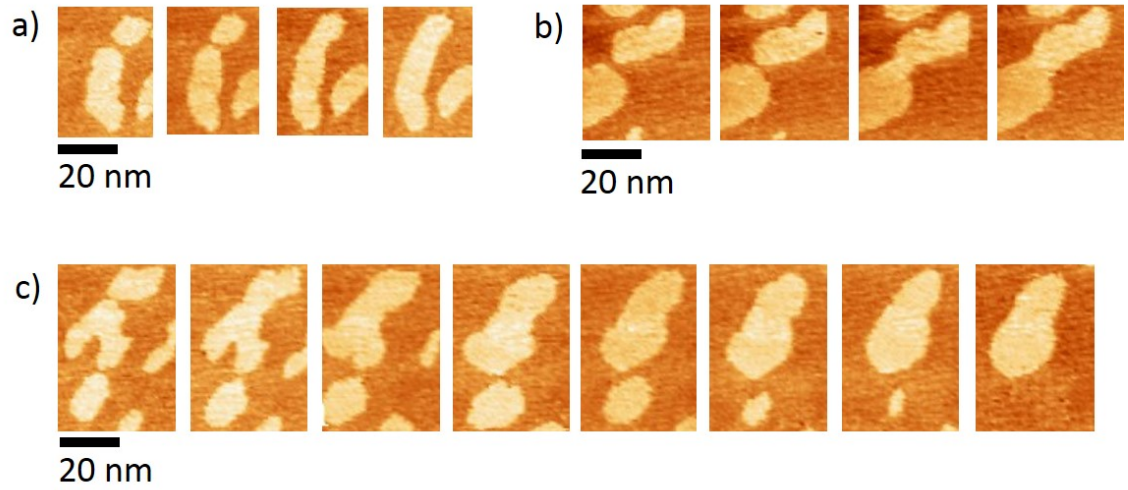

Fig. 5.13: The Ostwald and Smoluchowski ripening of S islands: Zoomed parts of STM images. a) and b) show the coalescence of two islands via Smoluchowski ripening. c) shows the growing of a large island at the expense of a small one, which eventually dissolves completely: the Ostwald ripening. Sequences a) and b) cover 20 min of scanning time and sequence c) 3 h 23 min.

effect, and hence there is mass flow from the small islands towards the larger ones. A critical minimum size of an island is the decisive factor for an island to dissolve or coalesce with another island.

5.3 Summary and discussion

We have followed the dynamics of the S-c(2×2) "on-top" islands under UHV conditions and at room temperature and identified two different mechanisms of surface diffusion, depending on the sulfur coverage of the surface. These two types of surface diffusion mechanisms are island ripening and island decay. The observed dynamic ripening, called Smoluchowski ripening, is characterized by the islands moving on the surface and coalescing together, forming large elongated islands along the [001] direction. The spacing between two islands and their orientation is transfered from the original Cu(110)-(2×1)O striped surface, which acts as a template. We have also observed small islands being dissolved while the larger ones grow (Ostwald ripening). Both ripening mechanisms are present at the surface even at saturation. According to our observations, the ripening continues until all S islands formed on one CuO stripe have merged together. Thereafter the coalescence is stopped, because the distance between two stripes is too large. This means that the energy cost for the

diffusion over such distance is larger than the energy won by forming a single large island on the surface.

The second type of mechanism, island decay, has been found to be present only at sub-saturation sulfur coverages. Atoms are detached from the periphery of the islands and incorporated into the surrounding overlayer, after which their contrast in STM, due to the height difference, is lost. This causes the islands to appear as if shrinking in STM images. The decay of the S islands has been found to depend on their size and shape. This is due to the fact that it is easier to extract atoms from the periphery of islands with small radius and high curvature. All islands are losing mass from their periphery at the same time, however, this happens very slowly for large islands. Therefore in the beginning, the shrinking of large islands is overcompensated by the mass transport towards them, due to Ostwald and Smoluchowski ripening and we observe the larger islands first growing and then shrinking. In the case of saturation, the islands do not disappear from the surface, because the atoms from the S-c(2×2) islands cannot be incorporated into an already saturated overlayer. A creation of a higher concentration phase would require more energy. The results demonstrate that the diffusion of the atoms from the periphery of the islands depends on the sulfur coverage of the surrounding surface. Finally, we have shown a way to prepare a new nanostructured surface, by transforming the CuO stripes of the Cu(110)-(2×1)O surface into S-c(2×2) “on-top” islands.

Conclusions and perspectives

The first objective of the present thesis was to study the tuning of the Cu(110)-(2×1)O system by the co-adsorption of sulfur. For this purpose, numerous nanostructures have been prepared and studied by STM. We have successfully demonstrated that the presence of surface adsorbates influences the self-organization. While the classical preparation allows to create nanostructures with periodicities in the limited range between 6.5 and 11 nanometers (for $0.1 < \theta_O < 0.4$), we have been able to prepare nanostructures with periodicities reaching up to ≈ 200 nm. Additionally, using the new preparation method, we can create nanostructures with the desired parameters P and θ_O, as they are now, in contrast to the classical preparation, independent of each other. The novel preparation consists in co-adsorbing oxygen and sulfur on the surface and then annealing at $T > 640$ K. We have found the final nanostructure to be independent of exposure sequence, as well as of the surface pre-nanostructuring.

Throughout the study, we have analyzed a great number of STM images of the Cu(110)-(2×1)O nanostructure. We have confirmed that the contrast of the oxidized and clean copper stripe depends on the chemical identity of the tip. A clean W-tip will give a different contrast for CuO than a tip ended by an oxygen atom. In our experiments, the highest contrast (largest height difference in the STM profile), has been obtained with a clean W-tip and tunneling conditions $I = 0.1$ nA and $V = 1.0$ V.

We have identified a second factor, which influences the periodicity of the O/Cu(110) nanostructured system, which is step bunching. The rearrangement of the surface into large terraces alternating by step bunches consisting of several monoatomic steps induces extra strain into the surface and thus changes the self-organization. Step bunching can be induced by annealing at higher temperatures

in the presence of oxygen. We have found that annealing at $T \geq 870$ K already creates a strained surface by step bunching and leads to increase in the periodicity. While the presence of sulfur seems to influence mainly nanostructures with high oxygen coverages, the step bunching increases periodicities of nanostructures with low oxygen coverages. One can therefore combine both effects to reach a desired structure. However, the introduction of step bunching into the surface is much less controllable and less effective than the S co-adsorption method.

We have found that the self-organization is very sensitive to the sulfur amount on the surface and therefore it is essential to ensure the same sulfur amount on the surface, if we want precise measurements from which we can extract a model. We have succeeded to do so, by doing consecutive oxidations of a surface with well-defined sulfur amounts. Finally, we have shown on three series of measurements, with $\theta_S = 0$, $\theta_S = 0.05$ and $\theta_S = 0.11$, that the points on the $P(\theta_O)$-graph describe clear curves. The experimental points for $\theta_S = 0$ are in very good agreement with the elastic model of Marchenko and Vanderbilt. To describe the influence of sulfur, we have introduced an added term, A, to this model, which describes the change in the surface creation energy. We have found A to be equal to 69.5 $\theta_S\theta_O$, which indicates an association with the interaction between oxygen and sulfur. We have also observed a saturation for the term A for high sulfur and oxygen coverages, which is probably associated with the saturation of the total surface coverage, $\theta_S + \theta_O$.

We do not observe sulfur on nanostructures prepared by S co-adsorption, once the surface has been annealed and cooled down to room temperature. This is because sulfur is mobile on copper, unless its diffusion is hindered by e.g. contaminations, defects or in the case of saturation. To understand the role of sulfur in the increase of the periodicity, it is essential to identify its position. We can assume that the sulfur is found on the clean copper stripes after the annealing, because if it would be on the oxidized stripes, we would have observed the c(2×2) structures, in which sulfur is known to adsorb on oxidized copper. However, there are other possibilities and sulfur could be incorporated into lower layers during the annealing. We hope that the planned XPS study will help to identify the exact position of sulfur, as the way sulfur is bound to the substrate will influence its peak position in the XPS spectrum. Furthermore we can use VT-STM (variable temperature) to follow the formation of the nanostructure during annealing and cooling down and reveal the role of sulfur in the nanostructure formation.

We have demonstrated that the presence of surface adsorbates can modify the structure of a self-organized system, by changing its elastic and/or electrostatic

properties. We believe that this method can be expanded to other self-organized systems and other adsorbates. Our study therefore opens new perspectives for the bottom-up approach in nanotechnology.

Being able to prepare a nanostructure with desired parameters is not only important for the direct application of the surfaces as templates for guided adsorption, but also opens perspectives for fundamental studies of the structure and reactivity interplay. The second objective of the present thesis has therefore been to study the sulfidation of the tunable Cu(110)-(2×1)O nanostructure. We have studied the kinetics of this reaction by AES, but have not observed any significant difference in the kinetics for different clean and oxidized Cu(110) surfaces. We believe that we will be able to identify the reaction kinetics more precisely by XPS in the near future. We have however obtained interesting results from the STM study of the reaction mechanisms. We have chosen a rather unique approach and studied the mechanisms of the reaction by STM directly in quasi real time during the exposure to H_2S. Our results demonstrate that the reaction mechanisms depend on the width of the oxidized stripes. Sulfidation of nanostructures with narrow oxidized stripes ($\omega_{CuO} \approx$ 3–10 nm) proceeds exclusively via Cu–O chain detachment. A new mechanism has been found during sulfidation of nanostructures with wider oxidized stripes ($\omega_{CuO} >$ 10 nm), which is a combination of the chain detachment and formation of sulfur islands (c(2×2) phase) on the oxidized stripes. The larger the width of the oxidized stripes, the less stable they are against attack by sulfur.

The new mechanism on wide oxidized stripes is as follows. During the adsorption of sulfur on the CuO stripes, the oxygen is removed and desorbs from the surface. The reconstructed copper added chains, from the (2×1) oxygen induced reconstruction, move together to form a Cu(1×1) adlayer, on which the sulfur adsorbs in c(2×2). The sulfur also adsorbs on the clean copper, which becomes free of adsorbed oxygen and copper adlayer, but this phase is in-plane with the rest of the surface and therefore only visible if atomic resolution is obtained. We can easily study the "on-top" S-(2×2) islands (sulfur adsorbed on the Cu adlayer), because of their good contrast in STM, due to the fact that the islands are one copper monolayer higher than the surrounding surface.

We have found that beside the width of the oxidized stripes, the H_2S exposure conditions influence the reaction mechanism as well. Namely, during a high pressure exposure, the S-c(2×2) island formation on the oxidized stripes will be favored. During a low pressure exposure of a nanostructure with wide oxidized stripes, the Cu–O detachment will be present next to the island formation and consequently

lead to formation of S-c(2×2) "on-top" islands on the originally clean copper stripes. During exposures at low pressures, the detached Cu–O chains have time to diffuse on the clean copper stripe and the copper adatoms from these chains act as a source of Cu adatoms for further S island formation. Besides, during low pressure exposures, we have noticed mass transport of Cu atoms towards the copper steps. Cu adatoms detached from the CuO stripes diffuse to the step edges and since the reaction progress is slow, the ends of terraces are still covered by CuO stripes. This causes the Cu adatoms to incorporate exclusively on the free sites and not the ones occupied by oxygen. After all the oxygen is removed, the step edges stay wavy, due to the uneven growth. This effect can only be observed on step edges perpendicular to the oxidized stripes.

In conclusion, we have demonstrated that we can change a reaction mechanism by changing the morphology of the support. The ability to guide and control a reaction on a surface is essential for the fields of heterogeneous catalysis and corrosion protection. As a perspective, it would be interesting to study other reactions of the tunable Cu(110)-(2×1)O nanostructure, to see how the structure will influence their behavior. Furthermore, one could study the influence of other factors, such as temperature, on the reaction mechanism.

The study of the dynamics of the sulfur "on-top" islands in UHV and at room temperature revealed two different kinds of surface diffusion mechanisms: island ripening and island decay. We have observed ripening of the islands by coalescence of smaller islands together. Additionally, large islands grew to some extent at the expense of smaller ones, which characterizes the Ostwald ripening. In the case of sub-saturation sulfur coverages, the islands disappear from the STM images due to the superficial diffusion of the sulfur atoms and copper adatoms from the periphery of the islands over the surface. The speed at which the island decays depends on its shape and size. We have found islands with a smaller radius to shrink faster, because the extraction of atoms from the periphery is easier for islands with higher curvature. This is due to lower coordination of atoms at their periphery and therefore their easier detachment. We have shown that the decay can be described by a classical power law model, as well as possible reasons for the deviations from the model. Additionally, an experiment in which we exposed the nanostructured surface to sulfur until saturation coverage revealed that if the S-c(2×2) "on-top" islands are surrounded by a saturated overlayer of sulfur, they are still mobile on the surface, but do not decay. This is probably because the sulfur atoms cannot be incorporated into the saturated overlayer. A higher concentration phase of sulfur, such as p(5×2)

or p(3×2), could be formed, however this would probably cost more energy because of the necessary compression of the copper lattice underlying the sulfur phase to create these phases. When exposing the nanostructured Cu(110)-(2×1)O surface to sulfur until saturation, the surface acts as a template for creating a S/Cu(110) nanostructured surface. This surface consists of an alternation of the S-c(2×2) "on-top" and "in-plane" stripes. Thus the surface is covered by the same chemical species and the nanostructuration is purely topographical. Due to time constraints, the observations of decaying S islands in the present thesis have been limited and could be extended. More data on the surface diffusion of the islands could help to conclude on the mechanisms involved and to obtain sufficient statistics. It would be of interest to follow the decay of an ensemble of islands, in order to determine the size distribution of the islands and thus possibly identify stabilized island shapes and sizes.

List of Figures

List of Tables

References

[1] Moore, G. *Electronics* **38**, 114–117 (1965).

[2] http://www.itrs.net/papers.html.

[3] http://www.scaruffi.com/monument/silicon/cmseq.html.

[4] https://comm350.wordpress.com/2012/03/04/worlds-smallest-computer/.

[5] Feynman, R. P. *Eng. Sci.* **23**, 22–36 (1960).

[6] http://www.research.ibm.com/articles/madewithatoms.shtml.

[7] Kern, K., Niehus, H., Schatz, A., Zeppenfeld, P., Goerge, J., and Comsa, G. *Phys. Rev. Lett.* **67**, 855–858 (1991).

[8] Koller, G., Winter, B., Oehzelt, M., Ivanco, J., Netzer, F., and Ramsey, M. *Org. Electron.* **8**, 63–68 (2007).

[9] Hu, Y., Maschek, K., Sun, L., Hohage, M., and Zeppenfeld, P. *Surf. Sci.* **600**, 762–769 (2006).

[10] Sun, L., Weidlinger, G., Denk, M., Denk, R., Hohage, M., and Zeppenfeld, P. *Phys. Chem. Chem. Phys.* **12**, 14706–14709 (2010).

[11] Koini, M., Haber, T., Werzer, O., Berkebile, S., Koller, G., Oehzelt, M., Ramsey, M., and Resel, R. *Thin Solid Films* **517**, 483–487 (2008).

[12] Oehzelt, M., Berkebile, S., Koller, G., Ivanco, J., Surnev, S., and Ramsey, M. *Surf. Sci.* **603**, 412–418 (2009).

[13] Otero, R., Naitoh, Y., Rosei, F., Jiang, P., Thostrup, P., Gourdon, A., Laegsgaard, E., Stensgaard, I., Joachim, C., and Besenbacher, F. *Angew. Chem. Int. Ed.* **43**, 2092–2095 (2004).

[14] Feitzinger, J. *IAU Symp.* , 559–560 (1985).

[15] Eaglesham, D. J. and Cerullo, M. *Phys. Rev. Lett.* **64**, 1943–1946 (1990).

[16] Nishimori, H. and Ouchi, N. *Phys. Rev. Lett.* **71**, 197–200 (1993).

[17] Moison, J., Houzay, F., Barthe, F., Leprince, L., Andre, E., and Vatel, O. *Appl. Phys. Lett.* **64**, 196–198 (1994).

[18] Tersoff, J., Teichert, C., and Lagally, M. *Phys. Rev. Lett.* **76**, 1675–1678 (1996).

[19] BenJacob, E. *Contemp. Phys.* **38**, 205–241 (1997).

[20] Facsko, S., Dekorsy, T., Koerdt, C., Trappe, C., Kurz, H., Vogt, A., and Hartnagel, H. *Science* **285**, 1551–1553 (1999).

[21] Whitesides, G. and Grzybowski, B. *Science* **295**, 2418–2421 (2002).

[22] Cen, R. *Astrophys. J. Lett.* **785**, L21 (2014).

[23] Rousset, S., Pourmir, F., Berroir, J., Klein, J., Lecoeur, J., Hecquet, P., and Salanon, B. *Surf. Sci.* **422**, 33–41 (1999).

[24] Swamy, K., Bertel, E., and Vilfan, I. *Surf. Sci.* **425**, L369–L375 (1999).

[25] Bachmann, A., Speller, S., Mugarza, A., and Ortega, J. *Surf. Sci.* **526**, L143–L150 (2003).

[26] Leibsle, F., Dhesi, S., Barrett, S., and Robinson, A. *Surf. Sci.* **317**, 309–320 (1994).

[27] Sotto, M. and Croset, B. *Surf. Sci.* **461**, 78–86 (2000).

[28] Rousset, S., Repain, V., Baudot, G., Ellmer, H., Garreau, Y., Etgens, V., Berroir, J., Croset, B., Sotto, M., Zeppenfeld, P., Ferre, J., Jamet, J., Chappert, C., and Lecoeur, J. *Mater. Sci. Eng.* **96**, 169–177 (2002).

[29] Hibino, H., Sumitomo, K., Fukuda, T., Homma, Y., and Ogino, T. *Phys. Rev. B* **58**, 12587–12589 (1998).

[30] Men, F. K., Liu, F., Wang, P. J., Chen, C. H., Cheng, D. L., Lin, J. L., and Himpsel, F. J. *Phys. Rev. Lett.* **88**, 096105 (2002).

[31] Fishlock, T., Pethica, J., and Egdell, R. *Surf. Sci.* **445**, L47–L52 (2000).

[32] Plass, R., Last, J., Bartelt, N., and Kellogg, G. *Nature* **412**, 875–876 (2001).

[33] Teichert, C., Lagally, M. G., Peticolas, L. J., Bean, J. C., and Tersoff, J. *Phys. Rev. B* **53**, 16334–16337 (1996).

[34] Barth, J. V., Costantini, G., and Kern, K. *Nature* **437**, 671–679 (2005).

[35] Ellmer, H., Repain, V., Sotto, M., and Rousset, S. *Surf. Sci.* **511**, 183 – 189 (2002).

[36] Denk, M., Denk, R., Hohage, M., Sun, L. D., and Zeppenfeld, P. *Phys. Rev. B* **85**, 014423 (2012).

[37] Brandstetter, T., Wagner, T., Fritz, D. R., and Zeppenfeld, P. *J. Phys. Chem. Lett.* **1**, 1026–1029 (2010).

[38] Somorjai, G. A. *Chem. Rev.* **96**, 1223–1236 (1996).

[39] Ertl, G. *Angew. Chem. Int. Ed.* **47**, 3524–3535 (2008).

[40] Taylor, H. *Proc. R. Soc.* **108**, 105–111 (1925).

[41] Sinfelt, J. volume 23 of *Advances in Catalysis*, 91 – 119. Academic Press (1973).

[42] Clarke, J. and Rooney, J. volume 25 of *Advances in Catalysis*, 125 – 183. Academic Press (1976).

[43] Bennett, C. and Che, M. *J. Catal.* **120**, 293–302 (1989).

[44] Jacobs, P., Ribeiro, F., Somorjai, G., and Wind, S. *Catal. Lett.* **37**, 131–136 (1996).

[45] Komarneni, M., Shan, J., Chakradhar, A., Kadossov, E., Cabrini, S., and Burghaus, U. *J. Phys. Chem. C* **116**, 5792–5801 (2012).

[46] Kadossov, E., Cabrini, S., and Burghaus, U. *J. Mol. Catal. A: Chem.* **321**, 101–109 (2010).

[47] Chakradhar, A., Shan, J., Komarneni, M. R., Lu, M., and Burghaus, U. *Chem. Phys. Lett.* **544**, 70–72 (2012).

[48] Eppler, A., Zhu, J., Anderson, E., and Somorjai, G. *Top. Catal.* **13**, 33–41 (2000).

[49] Wong, K., Johansson, S., and Kasemo, B. *Faraday Discuss.* **105**, 237–246 (1996).

[50] Bobrov, K. and Guillemot, L. *Surf. Sci.* **611**, 32–39 (2013).

[51] Guillemot, L. and Bobrov, K. *J. Phys.Chem. C* **115**, 22387–22392 (2011).

[52] Ertl, G. *Surf. Sci.* **6**, 208–232 (1967).

[53] Wit, A. D., Bronckers, R., and Fluit, J. *Surf. Sci.* **82**, 177–194 (1979).

[54] Stroscio, J., Persson, M., and Ho, W. *Phys. Rev. B* **33**, 6758–6770 (1986).

[55] Mundenar, J., Baddorf, A., Plummer, E., Sneddon, L., Didio, R., and Zehner, D. *Surf. Sci.* **188**, 15–31 (1987).

[56] Lapujoulade, J., Le Cruër, Y., Lefort, M., Lejay, Y., and Maurel, E. *Phys. Rev. B* **22**, 5740–5743 (1980).

[57] Lapujoulade, J., Le Cruër, Y., Lefort, M., Lejay, Y., and Maurel, E. *Surf. Sci.* **118**, 103–120 (1982).

[58] Niehus, H. and Comsa, G. *Surf. Sci.* **140**, 18–30 (1984).

[59] Bader, M., Puschmann, A., Ocal, C., and Haase, J. *Phys. Rev. Lett.* **57**, 3273–3276 (1986).

[60] Parkin, S. R., Zeng, H. C., Zhou, M. Y., and Mitchell, K. A. R. *Phys. Rev. B* **41**, 5432–5435 (1990).

[61] Feidenhans'l, R., Grey, F., Nielsen, M., Besenbacher, F., Jensen, F., Laegsgaard, E., Stensgaard, I., Jacobsen, K. W., Nørskov, J. K., and Johnson, R. L. *Phys. Rev. Lett.* **65**, 2027–2030 (1990).

[62] Feidenhans'l, R. and Stensgaard, I. *Surf. Sci.* **133**, 453–468 (1983).

[63] DiDio, R. A., Zehner, D. M., and Plummer, E. W. *J. Vac. Sci. Technol. A* **2**, 852–855 (1984).

[64] Liang, K., Fuoss, P., Hughes, G., and Eisenberger, P. *The Structure of Surfaces*. Springer-Verlag, Berlin, (1985).

[65] Chua, F. M., Kuk, Y., and Silverman, P. J. *Phys. Rev. Lett.* **63**, 386–389 (1989).

[66] Tjeng, L., Meinders, M., and Sawatzky, G. *Surf. Sci.* **233**, 163–183 (1990).

[67] Coulman, D. J., Wintterlin, J., Behm, R. J., and Ertl, G. *Phys. Rev. Lett.* **64**, 1761–1764 (1990).

[68] Jensen, F., Besenbacher, F., Laegsgaard, E., and Stensgaard, I. *Phys. Rev. B* **41**, 10233 (1990).

[69] Kuk, Y., Chua, F. M., Silverman, P. J., and Meyer, J. A. *Phys. Rev. B* **41**, 12393 (1990).

[70] Besenbacher, F. and Nørskov, J. K. *Prog. Surf. Sci.* **44**, 5–66 (1993).

[71] Wintterlin, J., Schuster, R., Coulman, D. J., Ertl, G., and Behm, R. J. *J. Vac. Sci. Technol. B* **9**, 902–908 (1991).

[72] Li, L., Cai, N., Saidi, W. A., and Zhou, G. *Chemical Physics Letters* **613**, 64–69 (2014).

[73] Besenbacher, F., Jensen, F., Laegsgaard, E., Mortensen, K., and Stensgaard, I. *J. Vac. Sci. Technol. B* **9**, 874–878 (1991).

[74] Bobrov, K. and Guillemot, L. *Surf. Sci.* **604**, 1894–1898 (2010).

[75] Guillemot, L. and Bobrov, K. *Phys. Rev. B* **83**, 075409 (2011).

[76] Poulain, C., Wiame, F., Maurice, V., and Marcus, P. *Surf. Sci.* **606**, L26–L30 (2012).

[77] Mocuta, D., Ahner, J., Lee, J.-G., Denev, S., and Jr., J. T. Y. *Surf. Sci.* **436**, 72–82 (1999).

[78] Hartmann, N. and Madix, R. *Surf. Sci.* **488**, 107–122 (2001).

[79] Prévot, G., Croset, B., Girard, Y., Coati, A., Garreau, Y., Hohage, M., Sun, L. D., and Zeppenfeld, P. *Surf. Sci.* **549**, 52–66 (2004).

[80] Bombis, C., Moiseeva, M., and Ibach, H. *Phys. Rev. B* **72**, 245408 (2005).

[81] Bobrov, K. and Guillemot, L. *Phys. Rev. B* **78**, 121408 (2008).

[82] Ruan, L., Besenbacher, F., Stensgaard, I., and Laegsgaard, E. *Phys. Rev. Lett.* **70**, 4079–4082 (1993).

[83] Sun, L. D., Hohage, M., Denk, R., and Zeppenfeld, P. *Phys. Rev. B* **76**, 245412 (2007).

[84] Marchenko, V. *JETP Lett.* **55**, 73–76 (1992).

[85] Vanderbilt, D. *Surf. Sci.* **268**, L300–L304 (1992).

[86] Zeppenfeld, P., Krzyzowski, M., Romainczyk, C., Comsa, G., and Lagally, M. G. *Phys. Rev. Lett.* **72**, 2737–2740 (1994).

[87] Marchenko, V. *JETP Lett.* **33**, 381–383 (1981).

[88] Alerhand, O. L., Vanderbilt, D., Meade, R. D., and Joannopoulos, J. D. *Phys. Rev. Lett.* **61**, 1973–1976 (1988).

[89] Poulain, C. *Nanostructuration de la surface O/Cu(110) et rôle sur la réactivité.* PhD thesis, Université Pierre et Marie Curie, (2013).

[90] Rostrup-Nielsen, J. *J. Catal.* **85**, 31–43 (1984).

[91] Newsome, D. *Cat. Rev. - Sci. Eng.* **21**, 275–318 (1980).

[92] Campbell, C. T. and Koel, B. E. *Surf. Sci.* **183**, 100–112 (1987).

[93] Marcus, P., Barbouth, N., and Oudar, J. *C. R. Acad. Sci. Paris* **280**, 1183–1186 (1975).

[94] Oudar, J. and Marcus, P. *Appl. Surf. Sci.* **3**, 48–67 (1979).

[95] Domange, J. and Oudar, J. *Surf. Sci.* **11**, 124–142 (1968).

[96] Petrino, P., Moya, F., and Cabané-Brouty, F. *J. Solid State Chem.* **2**, 439–444 (1970).

[97] Werlen-Ruze, B. and Oudar, J. *J. Cryst. Growth* **9**, 47–59 (1971).

[98] Kostelitz, M. and Oudar, J. *Surf. Sci.* **27**, 176–190 (1971).

[99] Carley, A. F., Davies, P. R., Jones, R. V., Harikumar, K. R., Kulkarni, G. U., and Roberts, M. W. *Surf. Sci.* **447**, 39–50 (2000).

[100] Stensgaard, I., Ruan, L., Besenbacher, F., Jensen, F., and Laegsgaard, E. *Surf. Sci.* **269-270**, 81–88 (1992).

[101] Maurice, V., Oudar, J., and Huber, M. *Surf. Sci.* **187**, 312–326 (1987).

[102] Parker, T., Condon, N., Lindsay, R., Thornton, G., and Leibsle, F. *Surf. Rev. Lett.* **01**, 705–708 (1994).

[103] Atrei, A., Johnson, A., and King, D. *Surf. Sci.* **254**, 65–72 (1991).

[104] Bonzel, H. *Surf. Sci.* **27**, 387–410 (1971).

[105] Moroney, L., Rassias, S., and Roberts, M. *Surf. Sci.* **105**, L249–254 (1981).

[106] Uy, P. S., Bardolle, J., and Bujor, M. *Surf. Sci.* **134**, 713–721 (1983).

[107] Prabhakaran, K., Sen, P., and Rao, C. *Surf. Sci.* **169**, L301–306 (1986).

[108] Colaianni, M. L., Syhler, P., and Chorkendorff, I. *Phys. Rev. B* **52**, 2076–2082 (1995).

[109] Alemozafar, A. R., Guo, X.-C., and Madix, R. J. *J. Chem. Phys.* **116**, 4698–4706 (2002).

[110] Wiame, F., Maurice, V., and Marcus, P. *Surf. Sci.* **600**, 3540–3543 (2006).

[111] Afsin, B., Davies, P., Pashusky, A., Roberts, M., and Vincent, D. *Surf. Sci.* **284**, 109–120 (1993).

[112] Carley, A. F., Davies, P. R., Roberts, M. W., and Vincent, D. *Top. Catal.* **1**, 35–42 (1994).

[113] Carley, A. F., R. Davies, P., and Wyn Roberts, M. *Chem. Commun.* , 1793–1794 (1998).

[114] Guo, X.-C. and Madix, R. J. *Surf. Sci.* **367**, L95–L101 (1996).

[115] Guo, X.-C. and Madix, R. J. *Surf. Sci.* **387**, 1–10 (1997).

[116] Kishi, K., R. M. *J. Chem. Soc. Faraday Trans.* **71**, 1721–1726 (1975).

[117] Joyner, R., McKee, C., and Roberts, M. *Surf. Sci.* **27**, 279–285 (1971).

[118] Roberts, M. W. *Surf. Sci.* **299/300**, 769–784 (1994).

[119] Au, C. and Roberts, M. *Chem. Phys. Lett.* **74**, 472–474 (1980).

[120] Zhou, Y. and White, J. *Surf. Sci.* **183**, 363–376 (1987).

[121] Mitchell, G., Schulz, M., and White, J. *Surf. Sci.* **197**, 379–390 (1988).

[122] Ruan, L., Besenbacher, F., Stensgaard, I., and Laegsgaard, E. *Phys. Rev. Lett.* **69**, 3523–3526 (1992).

[123] Besenbacher, F., Stensgaard, I., Ruan, L., Nørskov, J., and Jacobsen, K. *Surf. Sci.* **272**, 334–341 (1992).

[124] Perdereau, M. and Oudar, J. *Surf. Sci.* **20**, 80–98 (1970).

[125] Ostwald, W. *Z. Phys. Chem.* **34**, 495–503 (1900).

[126] Lifshitz, I. and Slyozov, V. *J. Phys. Chem. Solids* **19**, 35–50 (1961).

[127] Wagner, C. *Z. Elektrochem.* **65**, 581–591 (1961).

[128] Chakraverty, B. *J. Phys. Chem. Solids* **28**, 2401 – 2412 (1967).

[129] Wynblatt, P. and Gjostein, N. *Supported Metal Crystallites*, volume 9 of *Progress in Solid State Chemistry*. Pergamon, Oxford, (1975).

[130] Mullins, W. W. *J. Appl. Phys.* **28**, 333–339 (1957).

[131] McLean, J. G., Krishnamachari, B., Peale, D. R., Chason, E., Sethna, J. P., and Cooper, B. H. *Phys. Rev. B* **55**, 1811–1823 (1997).

[132] Smoluchowski, M. *Z. Phys.* **17**, 557–585 (1916).

[133] Khare, S., Bartelt, N., and Einstein, T. *Phys. Rev. Lett.* **75**, 2148–2151 (1995).

[134] Van Siclen, C. D. *Phys. Rev. Lett.* **75**, 1574–1577 (1995).

[135] Wen, J., Chang, S., Burnett, J., Evans, J., and Thiel, P. *Phys. Rev. Lett.* **73**, 2591–2594 (1994).

[136] Morgenstern, K., Rosenfeld, G., Poelsema, B., and Comsa, G. *Phys. Rev. Lett.* **74**, 2058–2061 (1995).

[137] Soler, J. M. *Phys. Rev. B* **53**, R10540–R10543 (1996).

[138] Binning, G., Rohrer, H., Gerber, C., and Weibel, E. *App. Phys. Lett.* **40**, 178–180 (1982).

[139] Binnig, G., Rohrer, H., Gerber, C., and Weibel, E. *Phys. Rev. Lett.* **49**, 57–61 (1982).

[140] van de Leemput, L. E. C., Rongen, P. H. H., Timmerman, B. H., and van Kempen, H. *Rev. Sci. Instrum.* **62**, 989–992 (1991).

[141] Jorgensen, J., Madsen, L., Garnaes, J., Carneiro, K., and Schaumburg, K. *J. Vac. Sci. Technol., B* **12**, 1698–1701 (1994).

[142] Chikkamaranahalli, S. B., Vallance, R. R., Damazo, B. N., and Silver, R. M. In *American Society for Precision Engineering 2006 Spring Topical Meeting: Challenges at the Intersection of Precision Engineering and Vacuum Technology*, (2006).

[143] Davies, P. In *Encyclopedia of Materials: Science and Technology (Second Edition),* Buschow, K. J., Cahn, R. W., Flemings, M. C., Ilschner, B., Kramer, E. J., Mahajan, S., and Veyssiére, P., editors, 6624 – 6630. Elsevier, Oxfordsecond edition edition (2001).

[144] Bardeen, J. *Phys. Rev. Lett.* **6**, 57–59 (1961).

[145] Tersoff, J. and Hamann, D. *Phys. Rev. B* **31**, 805–813 (1985).

[146] Chen, C. J. *Phys. Rev. B* **42**, 8841–8857 (1990).

[147] Meitner, L. *Z. Phys.* **9**, 131–144 (1922).

[148] Auger, P. *Cr. Hebd. Acad. Sci.* **177**, 169–171 (1923).

[149] Auger, P. *J. Phys. Radium* **6**, 205–208 (1925).

[150] Harris, L. A. *J. Appl. Phys.* **39**, 1419–1427 (1968).

[151] Weber, R. E. and Peria, W. T. *J. Appl. Phys.* **38**, 4355–4358 (1967).

[152] Palmberg, P. W., Bohn, G. K., and Tracy, J. C. *App. Phys. Lett.* **15**, 254–255 (1969).

[153] Gallon, T. and Matthew, J. *Review of Physics in Technology* **3**, 31–64 (1972).

[154] Seah, M. and Dench, W. *Surf. Interface Anal.* **1**, 2–11 (1979).

[155] http://www.spl.eu/.

[156] Ibe, J. P., Bey, P. P., Brandow, S. L., Brizzolara, R. A., Burnham, N. A., DiLella, D. P., Lee, K. P., Marrian, C. R. K., and Colton, R. J. *J. Vac. Sci. Technol. A* **8**, 3570–3575 (1990).

[157] Necas, D. and Klapetek, P. *Cent. Eur. J. Phys.* **10**, 181–188 (2012).

[158] Horcas, I., Fernandez, R., Gomez-Rodriguez, J. M., Colchero, J., Gomez-Herrero, J., and Baro, A. M. *Rev. Sci. Instrum.* **78**, 013705 (2007).

[159] Buisset, J., Rust, H.-P., Schweizer, E., Cramer, L., and Bradshaw, A. *Surf. Sci.* **349**, L147–L152 (1996).

[160] Uehara, Y., Matsumoto, T., and Ushioda, S. *Phys. Rev. B* **66**, 075413 (2002).

[161] Wiame, F., Poulain, C., Budinska, Z., Maurice, V., and Marcus, P. *Surf. Sci.* **636**, L1–L4 (2015).

[162] Reinecke, N., Reiter, S., Vetter, S., and Taglauer, E. *Appl. Phys. A Mater. Sci. Process.* **75**, 1–10 (2002).

[163] Brandstetter, T., Draxler, M., Hohage, M., and Zeppenfeld, P. *Phys. Rev. B* **76**, 245420 (2007).

[164] Brandstetter, T., Draxler, M., Hohage, M., and Zeppenfeld, P. *Phys. Rev. B* **78**, 075402 (2008).

[165] Guillemot, L. and Bobrov, K. *Phys. Rev. B* **79**, 201406 (2009).

[166] Morgenstern, K., Rosenfeld, G., Poelsema, B., and Comsa, G. *Surf. Sci.* **352-354**, 956–959 (1996).

[167] Kellogg, G. *Surf. Sci. Rep.* **21**, 1–88 (1994).

[168] Besenbacher, F. *Rep. Prog. Phys.* **59**, 1737–1802 (1996).

[169] Fink, H.-W. *Diffusion at Interfaces – Microscopic Concepts.* Springer-Verlag, Berlin, (1988).

[170] Zinke-Allmang, M., Feldman, L. C., and Grabow, M. H. *Surf. Sci. Rep.* **16**, 377–463 (1992).

[171] Family, F. and Meakin, P. *Phys. Rev. Lett.* **61**, 428–431 (1988).

[172] Wen, J.-M., Evans, J. W., Bartelt, M. C., Burnett, J. W., and Thiel, P. A. *Phys. Rev. Lett.* **76**, 652–655 (1996).

[173] Rosenfeld, G., Morgenstern, K., Esser, M., and Comsa, G. *Appl. Phys. A* **69**, 489–496 (1999).

[174] Morgenstern, K., Rosenfeld, G., and Comsa, G. *Surf. Sci.* **441**, 289 – 300 (1999).

[175] Morgenstern, K., Lægsgaard, E., Stensgaard, I., and Besenbacher, F. *Phys. Rev. Lett.* **83**, 1613–1616 (1999).

[176] Morgenstern, K., Lægsgaard, E., and Besenbacher, F. *Phys. Rev. B* **66**, 115408 (2002).

[177] Binder, K. and Kalos, M. *J. Stat. Phys.* **22**, 363–396 (1980).

[178] Voter, A. F. *Phys. Rev. B* **34**, 6819–6829 (1986).

[179] Pai, W. W., Swan, A. K., Zhang, Z., and Wendelken, J. F. *Phys. Rev. Lett.* **79**, 3210–3213 (1997).

[180] Stoldt, C. R., Jenks, C. J., Thiel, P. A., Cadilhe, A. M., and Evans, J. W. *J. Chem. Phys.* **111**, 5157–5166 (1999).

[181] Trevor, D. and Chidsey, C. *J. Vac. Sci. Technol. B* **9**, 964–968 (1991).

[182] de la Figuera, J., Prieto, J., Ocal, C., and Miranda, R. *Solid State Comm.* **89**, 815–818 (1994).

[183] Hamilton, J. C., Daw, M. S., and Foiles, S. M. *Phys. Rev. Lett.* **74**, 2760–2763 (1995).

[184] Morgenstern, K., Lægsgaard, E., and Besenbacher, F. *Phys. Rev. Lett.* **86**, 5739–5742 (2001).

[185] Rost, M. J., van Albada, S. B., and Frenken, J. W. M. *Phys. Rev. Lett.* **86**, 5938–5941 (2001).

[186] Linderoth, T. R., Horch, S., Petersen, L., Laegsgaard, E., Stensgaard, I., and Besenbacher, F. *New J. Phys.* **7**, 13–25 (2005).

[187] Schunack, M., Linderoth, T. R., Rosei, F., Lægsgaard, E., Stensgaard, I., and Besenbacher, F. *Phys. Rev. Lett.* **88**, 156102 (2002).

[188] Morgenstern, K. *Phys. Stat. Sol. B* **242**, 773–796 (2005).

[189] Rusponi, S., Boragno, C., Ferrando, R., Hontinfinde, F., and Valbusa, U. *Surf. Sci.* **440**, 451 – 459 (1999).

[190] Wynblatt, P. and Gjostein, N. *Surf. Sci.* **12**, 109–127 (1968).

[191] Cousty, J., Peix, R., and Perraillon, B. *Surf. Sci.* **107**, 586–604 (1981).

[192] Liu, C., Cohen, J., Adams, J., and Voter, A. *Surf. Sci.* **253**, 334–344 (1991).

[193] Hansen, L., Stoltze, P., Jacobsen, K. W., and Nørskov, J. K. *Phys. Rev. B* **44**, 6523–6526 (1991).

[194] Perkins, L. S. and DePristo, A. E. *Surf. Sci.* **317**, L1152–L1156 (1994).

[195] Stoltze, P. *J. Phys. Condens. Matter* **6**, 9495–9517 (1994).

[196] Karimi, M., Tomkowski, T., Vidali, G., and Biham, O. *Phys. Rev. B* **52**, 5364–5374 (1995).

[197] Evangelakis, G., Papageorgiou, D., Kallinteris, G., Lekka, C., and Papanicolaou, N. *Vacuum* **50**, 165–169 (1998).

[198] Mottet, C., Ferrando, R., Hontinfinde, F., and Levi, A. *Surf. Sci.* **417**, 220–237 (1998).

[199] Montalenti, F. and Ferrando, R. *Phys. Rev. B* **59**, 5881–5891 (1999).

[200] Prévot, G., Cohen, C., Schmaus, D., and Pontikis, V. *Surf. Sci.* **459**, 57–68 (2000).

[201] Wang, Z., Li, Y., and Adams, J. *Surf. Sci.* **450**, 51–63 (2000).

[202] Kürpick, U. *Phys. Rev. B* **64**, 075418 (2001).

[203] Ndongmouo, U. and Hontinfinde, F. *Surf. Sci.* **571**, 89–101 (2004).

[204] Kong, L. and Lewis, L. J. *Phys. Rev. B* **77**, 165422 (2008).

[205] Wrigley, J. D. and Ehrlich, G. *Phys. Rev. Lett.* **44**, 661–663 (1980).

[206] Bassett, D. and Webber, P. *Surf. Sci.* **70**, 520–531 (1978).

[207] Robinson, I., Whiteaker, K., and Walko, D. *Physica B* **221**, 70–76 (1996).

[208] Morgenstern, K., Rosenfeld, G., and Comsa, G. *Phys. Rev. Lett.* **76**, 2113–2116 (1996).

[209] Icking-Konert, G. S., Giesen, M., and Ibach, H. *Surf. Sci.* **398**, 37 – 48 (1998).

[210] Otero, R., Vázquez de Parga, A. L., and Miranda, R. *Phys. Rev. B* **66**, 115401 (2002).

[211] Morgenstern, K., Lægsgaard, E., and Besenbacher, F. *Phys. Rev. Lett.* **94**, 166104 (2005).

Self-organization, reactivity, and stability of nanostructured copper surfaces

Self-organized nanostructures are essential for the field of nanotechnology, since they provide a relatively simple way to create periodic structures with nanodimensions. In the present work, we have developed a new preparation method for the Cu(110)-(2×1)O nanostructure, which allows tuning of its morphology. For oxygen coverages between 0.1 and 0.4 (saturation coverage 0.5), the periodicity of this nanostructure varies from 6.5 to 11 nanometers. We have been able to expand the possibilities of the system and reach periodicities up to 100 nanometers for half oxygen coverage. The preparation method consists in co-adsorption of low amounts of sulfur. We have shown that the presence of sulfur influences the elastic and/or electrostatic properties of the surface and thus changes its self-organization. We present a detailed scanning tunneling microscopy (STM) study of this new preparation method and a mathematical model describing our experimental data.

A tunable self-organized surface provides an ideal playground for testing the reactivity and structure interplay. We introduce an Auger electron spectroscopy (AES) and STM study of the sulfidation of the nanostructured Cu(110)-(2×1)O surface. The reaction mechanism has been found to depend on the width of the oxidized stripes. Sulfidation of narrow CuO stripes proceeds via Cu–O chain abstraction and in the case of wide CuO stripes, the reaction mechanism is a combination of the chain detachment and S-c(2×2) island formation on the CuO stripes. We present a thorough STM study of the S island formation, as well as of their stability under UHV conditions, following the exposure to H_2S. The S islands have been found to be mobile at room temperature and undergo ripening. Both Ostwald and Smoluchowski mechanisms have been observed. If the surface is saturated by sulfur, the islands eventually reach an equilibrium. In the case of a sub-saturated surface, a radius-dependent island decay has been observed.

Keywords: Scanning tunneling microscopy, Sulfidation, Copper(110), Reaction mechanism

Auto-organisation, réactivité et stabilité de surfaces nanostructurées de cuivre

Les nanostructures auto-organisées sont essentielles dans le domaine des nanotechnologies, car elles fournissent un moyen relativement simple de créer des structures périodiques avec des dimensions nanométriques. Dans ce travail, nous avons étudié la surface Cu(110)-(2×1)O, dans le but d'élargir les possibilités de ce système. Nous introduisons une nouvelle méthode de préparation de cette surface auto-organisée, qui permet un contrôle de sa morphologie. La périodicité varie de 6.5 à 11 nm pour recouvrement en oxygène entre 0.1 et 0.4 (saturation est 0.5). On a réussi à obtenir des périodicités allant jusqu'au 100 nm. La préparation est basée sur la pré-adsorption de faibles quantités de soufre. Nous avons montré que la présence de soufre change les propriétés élastiques et/ou électrostatiques de la surface et modifie ainsi son auto-organisation. Nous avons effectué une étude détaillée au moyen de la microscopie à effet tunnel (STM) de cette nouvelle méthode de préparation et développé un modèle mathématique décrivant nos données expérimentales.

Une surface auto-organisée accordable fournit un système idéal pour étudier l'interaction entre la réactivité et la structure. Dans ce travail, nous avons étudié la sulfuration au moyen de la spectroscopie d'électrons Auger (AES) et STM sur la surface nanostructurée, Cu(110)-(2 ×1)O. Le mécanisme réactionnel est modifié et dépend de la largeur des bandes oxydées. La sulfuration d'une nanostructure à bandes oxydées étroites conduit au détachement de chaînes reconstruites Cu–O et dans le cas de bandes larges, le mécanisme réactionnel est une combinaison du détachement de chaînes et de la formation d'îlots de la phase S-c(2×2) sur les bandes CuO. Nous présentons une étude STM approfondie de la formation de ces îlots, ainsi que leur évolution après l'exposition à H_2S. Les îlots sont mobiles sur la surface même à température ambiante et subissent une maturation. Les deux mécanismes, Ostwald et Smoluchowski, ont été observé. Si la surface est saturée en soufre, les îlots finissent par atteindre un équilibre. Dans le cas d'une surface non complètement saturé, les îlots disparaissent progressivement à des vitesses qui dépendent de leur taille.

Mots clés : Microscopie à éffet tunnel, Sulfuration, Cuivre(110), Mécanismes réactionnels